

ABSTRACT

Title of Dissertation: FUNCTIONALIZED NANOPARTICLES FOR THE CONTROLLED MODULATION OF CELLULAR BEHAVIOR

Katherine E. Pendragon, Doctor of Philosophy, 2023

Dissertation directed by: Dr. James B. Delehanty
US Naval Research Laboratory

Professor John P. Fisher
Fischell Department of Bioengineering

The ability to control cellular behavior at the single-cell level is of great importance for gaining a nuanced understanding of cellular machinery. This dissertation focuses on the development of novel hard nanoparticle (NP) bioconjugate materials, specifically gold nanoparticles (AuNPs) and quantum dots (QDs), for the controlled modulation of cellular behavior. These hard NPs offer advantages such as small size on the order of 1 – 100 nm, high stability, unique optical properties, and the ability to load cargo on a large surface area to volume ratio, making them ideal tools for understanding and controlling cell behavior. In Aim 1, we demonstrate the use of AuNPs to manipulate cellular biological functions, specifically the modulation of membrane potential. We present the conception of anisotropic-shaped AuNPs, known as gold nanoflowers (AuNFs), which exhibit broad absorption extending into the near-infrared region of the spectrum. We demonstrate the effectiveness of utilizing the plasmonic properties AuNFs for inducing plasma membrane depolarization in rat adrenal medulla pheochromocytoma (PC-12) neuron-like cells. Importantly, this is achieved with temporal control and without negatively impacting cellular viability. Aim 2 explores the use of QDs as an optical, trackable scaffold for the multivalent display of growth

factors, specifically erythropoietin (EPO), for the enhanced induction of protein expression of aquaporin-4 (AQP4) within human astrocytes. This results in enhanced cellular water transport within human astrocytes, a critical function in the brain's glymphatic system. We show that EPO-QD-induced augmented AQP4 expression does not negatively impact astrocyte viability and augments the rate of water efflux from astrocytes by approximately two-fold compared to cells treated with monomeric EPO, demonstrating the potential of EPO-NP conjugates as research tools and prospective therapeutics for modulating glymphatic system function. Overall, the body of work presented in this dissertation develops new NP tools, namely solid anisotropic AuNFs and growth factor-delivering QDs, for the understanding and control of cell function. These new functional nanomaterials pave the way for the continued development of novel NP-based tools for the precise modulation of cellular physiology.

FUNCTIONALIZED NANOPARTICLES FOR THE CONTROLLED MODULATION OF CELLULAR BEHAVIOR

by

Katherine E. Pendragon

Dissertation submitted to the Faculty of the Graduate School of the
University of Maryland, College Park in partial fulfillment
of the requirements for the degree of
Doctorate of Philosophy
2023

Advisory Committee:

Dr. James Delehanty, Co-chair

Professor John Fisher, Co-chair

Professor Ian White

Professor Srinivasa Raghavan

Associate Professor Paul Paukstelis, Dean's Representative

DEDICATION

This work is dedicated to:

My late father Dr. William H. Rogers III,
who always encouraged my love of science
and in whose venerable footsteps I follow
as I endeavor to attain my Ph.D.

Table of Contents

| | |
|---|------------|
| Dedication | ii |
| Table of Contents | iii |
| Table of Figures..... | v |
| Table of Tables | v |
| List of Abbreviations | vi |
| Chapter 1: Introduction | 1 |
| The Cell: A Machine that Spans a Range of Size Scales | 1 |
| The Evolution of the Controlled Modulation of Cellular Function | 2 |
| Functional Nanomaterials for the Modulation of Cellular Behavior..... | 4 |
| Specific Aims | 8 |
| Specific Aim 1: Photothermal-Enhanced Modulation of Cellular Membrane Potential Using Long-Wavelength-Activated Gold Nanoflowers. | 8 |
| Specific Aim 2: Multivalent Display of Erythropoietin on Quantum Dots Enhances Aquaporin-4 Expression and Water Transport in Human Astrocytes In Vitro. | 9 |
| Chapter 2: Gold Nanoparticles and Quantum Dots: A Topical Review on their Use for Modulation of Cellular Function..... | 11 |
| Gold Nanoparticles (AuNPs)..... | 11 |
| Quantum Dots (QDs) | 18 |
| Chapter 3: Photothermal-enhanced Modulation of Cellular Membrane Potential using Long Wavelength-activated Gold Nanoflowers | 24 |
| Introduction..... | 24 |
| Materials and Methods..... | 26 |
| Synthesis of spherical AuNP (AuNS) in aqueous phase | 26 |
| Ligand exchange of AuNPs with TA-PEG-COOH/TA-PEG-Methoxy | 28 |
| UV-Vis Spectroscopy | 28 |
| Transmission electron microscopy (TEM) and scanning electron microscopy (SEM). | 28 |
| Dynamic light scattering..... | 29 |
| Conjugation of AuNPs to NH ₂ -PEG2000-Chol and NH ₂ -PEG2000-FITC. | 29 |
| Cell culture..... | 30 |
| Demonstration of AuNP-PEG-Chol/FITC localization to the plasma membrane..... | 30 |
| Characterization of AuNP-PEG-Chol-mediated membrane potential depolarization | 31 |
| Cellular cytotoxicity of AuNPs in PC-12 cells..... | 31 |
| Microscopy and Image Analysis..... | 32 |
| Statistical Analysis..... | 32 |
| Results and Discussion..... | 33 |
| Synthesis and characterization of AuNF-PEG-Chol and AuNS-PEG-Chol..... | 33 |

| | |
|---|-----------|
| Tethering of AuNF-PEG-Chol and AuNS-PEG-Chol to the plasma membrane..... | 37 |
| Depolarization of membrane potential via photoexcitation of AuNS-PEG-Chol and AuNF-PEG-Chol conjugates. | 39 |
| Effect of AuNP-PEG-Chol-mediated membrane depolarization on cellular viability. | 44 |
| Conclusion | 46 |
| | |
| Chapter 4: Multivalent Display of Erythropoietin on Quantum Dots Enhances Aquaporin-4 Expression and Water Transport in Human Astrocytes <i>In Vitro</i> | 49 |
| Introduction | 49 |
| Materials and Methods | 51 |
| Chemicals..... | 52 |
| CdSe core synthesis. | 52 |
| Overcoating of CdSe core QDs with CdS/ZnS shell. | 53 |
| Ligand exchange of CdSe/CdS/ZnS QDs..... | 53 |
| EPO-his assembly to QDs..... | 53 |
| Gel electrophoresis..... | 54 |
| Zeta potential and DLS. | 54 |
| Cell culture..... | 54 |
| Characterization of EPO-QD cellular labeling. | 55 |
| Induction of AQP4 expression using monomeric EPO or multivalent EPO-QDs. | 55 |
| Immunohistochemistry (IHC)..... | 55 |
| EPO and EPO-QD mediated activation of JAK/STAT signaling pathway. | 56 |
| Characterization of AQP4 water transport activity. | 56 |
| Cellular cytotoxicity of EPO-QDs..... | 57 |
| Microscopy and Image Analysis..... | 57 |
| Statistical Analysis..... | 58 |
| Results and Discussion | 58 |
| Characterization of EPO-QD bioconjugates. | 60 |
| Characterization of EPO-QD binding to EPOR on HA..... | 62 |
| Induction of AQP4 expression by EPO and EPO-QD bioconjugates. | 66 |
| Quantification of water transport in EPO and EPO-QD-treated HA..... | 68 |
| Cytotoxicity of EPO-QD bioconjugates. | 71 |
| Conclusion | 72 |
| | |
| Chapter 5: Conclusions and Future Outlook | 75 |
| | |
| Appendix | 81 |
| Contribution to Science | 81 |
| Publications..... | 81 |
| Presentations | 82 |
| Permissions | 83 |
| | |
| References | 88 |

Table of Figures

| | |
|---|----|
| Figure 1: Uses of AuNPs for the control of cellular function seen within recent scientific literature..... | 16 |
| Figure 2: Uses of QDs for the control of cellular function seen within recent scientific literature..... | 21 |
| Figure 3: Characterization of AuNF and AuNF-PEG-Chol conjugates..... | 33 |
| Figure 4: Capping ligands and AuNP conjugation..... | 34 |
| Figure 5: Localization of AuNS-Chol and AuNF-Chol conjugates to the plasma membranes... | 37 |
| Figure 6: Timelapse images of AuNF-Chol and AuNS-Chol mediated membrane depolarization..... | 40 |
| Figure 7: Membrane depolarization of PC-12 cells labeled with 1 nM AuNPs and excited using a 561 nm or a 640 nm laser at various power densities..... | 41 |
| Figure 8: Membrane depolarization of PC-12 cells labeled with AuNPs adjusted to the same optical density (OD = 0.52) at 561 nm..... | 43 |
| Figure 9: PC-12 cellular viability under AuNP-mediated membrane depolarization..... | 44 |
| Figure 10: EPO-QD bioconjugate system..... | 58 |
| Figure 11: Transmission electron microscopy (TEM) of QDs used in this study..... | 58 |
| Figure 12: Absorption and emission spectra of QDs..... | 59 |
| Figure 13: Physical characterization of EPO-QD bioconjugates..... | 60 |
| Figure 14: Immunohistochemistry (IHC) for visualization of EPOR expression in HA.. | 61 |
| Figure 15: Quantification of the binding of EPO-QD to EPOR on HA..... | 63 |
| Figure 16: Time-resolved labeling of HA with EPO-QD conjugates..... | 64 |
| Figure 17: Colocalization of EPO-QD with transferrin endocytosis marker..... | 64 |
| Figure 18: Competitive EPO-QD binding assay in HA..... | 65 |
| Figure 19: Quantification of JAK2 phosphorylation in HA..... | 66 |
| Figure 20: Induction of AQP4 expression by free EPO and EPO-QD..... | 67 |
| Figure 21: Quantification of water transport in EPO treated HA using calcein AM assay..... | 69 |
| Figure 22: Quantification of relative water transport rates in EPO-treated HA..... | 70 |
| Figure 23: Cytotoxicity of EPO and EPO-QD bioconjugates..... | 71 |
| Figure 24: Schematic of a combinatorial approach using techniques explored in Aim 1 and Aim 2..... | 78 |

Table of Tables

| | |
|---|----|
| Table 1: Characterization of AuNPs..... | 35 |
|---|----|

List of Abbreviations

| | |
|-------------------|---|
| 2D | Two-dimensional |
| 3D | Three-dimensional |
| β NGF | β subunit-neural growth factor |
| Ag | Silver |
| ANOVA | Univariate analysis of variance |
| AQP1 | Aquaporin |
| AQP4 | Aquaporin-4 |
| ATP | Adenosine triphosphate |
| Au | Gold |
| AuNF | Gold nanoflower |
| AuNP | Gold nanoparticle |
| AuNS | Gold nanosphere |
| Calcein AM | Calcein acetoxymethyl |
| CdMe ₂ | Dimethylcadmium |
| CdS | Cadmium sulfide |
| CdSe | Cadmium selenide |
| Chol | Cholesterol |
| ChR | Channelrhodopsin |
| CL4 | Compact ligand 4 |
| COVID-19 | Coronavirus disease 2019 |
| CRISPR | Clustered regularly interspaced short palindromic repeats |
| CSF | Cerebrospinal fluid |
| CTAB | Hexadecyltrimethylammonium bromide |
| DAPI | 4',6-diamidino-2-phenylindole |
| DLS | Dynamic light scattering |
| DNA | Deoxyribose nucleic acid |
| DOX | Doxorubicin |
| DPA | 1-Dodecylphosphonic acid |
| DPBS | Dulbecco's phosphate-buffered saline |
| EDC | 1-ethyl-3-(3-dimethylaminopropyl) carbodiimide |
| EDTA | Ethylenediaminetetraacetic acid |
| EGF | Epidermal growth factor |
| EGFR | Epidermal growth factor receptor |
| ELISA | Enzyme-linked immunosorbent assay |
| ELP | Elastin-like polypeptides |
| EPO | Erythropoietin |
| EPO-QD | Erythropoietin-quantum dot conjugate |
| EPOR | Erythropoietin receptor |
| FITC | Fluorescein isothiocyanate |

| | |
|-----------------------------|--|
| FDA | Food and Drug Administration |
| FRET | Fluorescence resonance energy transfer |
| GFP | Green fluorescent protein |
| GS | Glymphatic system |
| HA | Human astrocyte |
| HCl | Hydrochloric acid |
| HDA | Hexadecylamine |
| His | Histidine |
| Hsp | Hesperidin |
| IgG | Immunoglobulin G |
| IHC | Immunohistochemistry |
| IR | Infrared |
| JAK | Janus kinase |
| LCIS | Live cell imaging solution |
| mRNA | Messenger ribonucleic acid |
| MRSA | Methicillin resistant <i>S. aureus</i> |
| MTA | (11-mercaptoundecyl)-N,N,N-trimethylammonium |
| NHS | N-hydroxysuccinimide |
| NGF | Neural growth factor |
| NIR | Near-infrared |
| NP | Nanoparticle |
| PC-12 | Rat adrenal medulla pheochromocytoma |
| PD-10 | Protein desalting-10 |
| PEG | Polyethylene glycol |
| PTT | Photothermal therapy |
| QD | Quantum dot |
| QD-DOX | Quantum dot-doxorubicin conjugate |
| Rhodamine-PE | Lissamine Rhodamine B 1,2, dihexadecanoyl-sn-glycero-3-phosphoethanolamine |
| SARS-Cov-2 | Severe acute respiratory syndrome coronavirus 2 |
| Se | Selenium |
| SEM | Scanning electron microscopy |
| siRNA | Small interfering ribonucleic acid |
| SPR | Surface plasmon resonance |
| STAT | Signal transducer and activator of transcription |
| TA | Thioctic acid |
| TBE | Tris borate EDTA |
| TEM | Transmission electron microscopy |
| tetrachloroauric (III) acid | $\text{HAuCl}_4 \cdot 3\text{H}_2\text{O}$ |
| TMB | 3,3',3,5'-tetramethylbenzidine |

| | |
|--------------------|------------------------------------|
| TMS ₂ S | Hexamethyldisilathiane |
| TOP | Tri-n-octylphosphine |
| TOPO | Trioctylphosphine oxide |
| TPN-Q | Tertiapin-Q |
| TRITC | Tetramethylrhodamine |
| TrkA | Tyrosine kinase A |
| UV | Ultraviolet |
| VEGF | Vascular endothelial growth factor |
| YopM | <i>Yersinia</i> outer protein M |
| ZnEt ₂ | Diethyl zinc |
| ZnS | Zinc sulfide |

Chapter 1: Introduction

The Cell: A Machine that Spans a Range of Size Scales

Cells are the essential building blocks of life; they not only possess the capacity for self-replication and biochemical synthesis, but they also function as complex sensor-actuator systems that respond to cues from their environment. The cell is at the same time a signal receiver and transducer. Indeed, the cell is a living machine that spans a range of size scales. Mammalian cells, the focus of this dissertation, while on the micron size scale, are comprised of subcellular organelles (*e.g.*, the plasma membrane, endocytic vesicles, mitochondria) that are on the *nanoscale*. These nanoscale features work together to identify and interpret incoming signals, which in turn informs cellular behavior and processes such as cell proliferation, protein expression, metabolism, differentiation, and acute functions such as membrane depolarization.¹⁻³ Cells are able to detect a wide range of stimuli including physical, chemical, and electrical cues, and they translate this information into cellular responses that maintain cellular homeostasis. To accurately coordinate these multifaceted and complicated activities, cells possess a vast array of molecular sensory mechanisms that form elaborate intra- and extra-cellular networks. Further, the functionality of higher-order tissues and body organ systems are dependent on the interplay between cell types, where well-organized communication between groups of cells allows for harmonized combined behavior. This precise cellular signaling, either *via* chemical means (*e.g.*, growth factors, small molecules) or physical means (*e.g.*, electrical stimulation), is needed to maintain a normal physiological balance within an organism and these processes are conducted at the nanoscale.⁴ Therefore it is critical that we not only understand these physiological processes and but that we also develop the new functional tools to enable the control of cells at the nanoscale.

This is important not only for our furthered understanding of cellular function but also for the development of new, effective therapeutics.

The Evolution of the Controlled Modulation of Cellular Function

The treatment of disease through the use of medicines from natural sources such as mixed herbs, plants, and fungi has been documented since before 2000 B.C. from ancient civilizations including China, India, Mesopotamia, Egypt, Greece, and Rome.^{5,6} Ancient drugs such as salicylates found within white willow bark were used as an analgesic and anti-inflammatory medicine, with the exact mechanism of its inhibition of pro-inflammatory cytokines only discovered in the twenty-first century.⁷ As the breadth of knowledge in the field of chemical synthesis broadened, the diminished therapeutic effectiveness and negative off-target effects of naturally occurring medicines within plants prompted a shift towards the development of synthetic, man-made drugs.⁸ A key stride forward that led to the development of chemotherapy was made by Paul Ehrlich in the 1800s who noticed a selective affinity exhibited by dyes towards biological tissue. Ehrlich proposed the existence of specific ‘chemoreceptors’ on parasites, microorganisms and cancer cells that would be different than the corresponding structures within a host organism’s cells.⁹ The beginning of the 20th century in particular led to a boom in the fields of pharmacology and biochemistry, where the concepts of enzymes and receptors that can receive and generate specific signals within cells were found to be optimal drug targets.¹⁰ Building on these discoveries, in second half of the 20th century, the concept of cellular modulation became increasingly important as the influence of molecular biology began to intensify while considering new therapeutic approaches.

As the comprehension of the biological structure of molecules increased, there was a concomitant focus on the understanding of their action. Molecular biology significantly impacted

drug discovery by enabling the handling of genetic information in concrete biochemical and chemical terms.¹⁰ This progress in the understanding of genetics first enabled the ability to clone and express genes encoding therapeutically valuable proteins. In the late 20th and early 21st centuries, contemporary methodologies such as advanced high-resolution imaging modalities, high throughput technologies, and recently computational modeling have been able to further humanity's perspective on the operations of intracellular molecular mechanisms and how they affect cell function. Hence, a demand emerged within the scientific community for the development of nanoscale materials designed to interrogate cellular systems and, ultimately, manipulate them to regulate cellular behavior and enhance therapeutic outcomes.¹¹

The concept of the manipulation of matter at the atomic scale was famously introduced by Richard Feynman in 1959 in his landmark lecture, "There's Plenty of Room at the Bottom"¹² in which he postulated the realization of new functionalities of molecules if one could iteratively control the position of the atoms during their synthesis. In 1969, the first nanosized particles for targeted drug therapy were developed by Peter Paul Speiser.¹³ Soon afterward, the word "nanotechnology" was introduced by the scientist Norio Taniguchi to describe semiconductor processes at the nanometer scale.¹² During the 1990s, nanobiotechnology emerged as a prominent discipline, with a focus on the design, synthesis, characterization and use of nano-sized materials driven by the quest for better comprehension of molecular biology and the improvement of therapeutic medical strategies. In 1995, Doxil (liposomal encapsulation of the anti-cancer drug doxorubicin) became the first nano-drug approved by the U.S.'s Food and Drug Administration for the treatment of AIDS-related Kaposi's sarcoma.¹⁴ With the inception of the National Nanotechnology Initiative in 2000, interest in the use of nanotechnology has grown at a rampant pace, with over 66 approved nanomedicines by the U.S. Food and Drug Administration by the year

2022.¹⁵ Today, nanomedicine continues to enhance our understanding of pathophysiological mechanisms at the molecular level underlying disease, and to develop instruments for diagnosis, prevention, and therapeutic measures to improve clinical outcomes.¹⁶

Functional Nanomaterials for the Modulation of Cellular Behavior

A nanoparticle (NP) is defined as a material with at least one dimension between 1-100 nm in size.¹⁷ Many functional NPs are composed of three parts: 1) a central core, 2) a protective layer for biocompatibility and the prevention of premature degradation or release of the core contents, and 3) molecular linkers for the attachment or interaction with functional moieties (including targeting agents such as proteins, drugs, or other materials) to direct them to specific cells/cell types. However, the chemical composition of NPs can vary widely, including micelles, metal oxides, semiconductors, synthetic polymers or organic compounds.¹⁶ The shape of NPs can also vary widely from spherical to rod-shaped, or can include more complex structures. This high degree of variability in composite hybrid NP materials, along with their tunable size and physicochemical composition, enables NPs to perform a wide array of functions that can be tailored to specific niches for enhancing NP-based biotherapeutics.¹⁸

NPs offer several advantages that make them ideal for interfacing with cells both *in vitro* and *in vivo*. First, their nanoscale size places them between molecules and cellular organelles, and thus able to interface more easily with cellular machinery.¹⁷ Their small dimensions afford NPs with a large surface area to volume ratio, facilitating a substantial loading capacity for drugs, stealth agents, or targeting moieties on the surface of a single particle and thus decreasing the amount of scaffold materials needed to achieve therapeutic efficacy.¹⁸ This small size also allows for prolonged circulation within the bloodstream, as they can evade aggregation in microcapillaries and avoid phagocytosis by macrophages in the reticuloendothelial system. Enhanced penetration

into cells and tissues, reduced immunogenic effects from the body, and efficient renal clearance can be attributed to NPs' diminutive scale.^{18,19,20} The tunability of NP dimensions and materials allows for their use in a multitude of applications, as the dimension and dispersion of particles play a significant role in determining their biological fate, stability, toxicity, and targeting ability, while also influencing drug loading and release.¹⁹ Some NPs, such as semiconductor nanocrystals or quantum dots (QDs), even have inherent photophysical properties (*e.g.*, photoluminescence) that is determined by their size.¹⁸ Gold NPs (AuNPs) have photothermal properties that can be tuned based on NP shape and size. The use of hybrid materials can afford NPs a degree of multifunctionality, so that NPs can perform various distinct operations such as cellular targeting, intracellular localization, sensing, imaging, and drug delivery all on a single NP platform. Finally, as a therapeutic product, NPs can be delivered directly to the site of interest *via* intravenous or intramuscular injection, which gives them an edge against more invasive methods such as surgical implantation as well as non-specific oral drugs.^{21,22}

For NPs to be effective in the modulation of cellular function and behavior, they need to possess a number of required criteria. Foremost, NPs must be biocompatible and non-toxic. This is a fundamental requirement for NP utilization within a biological environment; biocompatibility ensures that the NPs do not instigate harmful immunogenic responses, which would lead to inflammation in the body or triggering of apoptosis within the cell.²⁰ A quintessential example of biocompatibility in NP design is the use of polyethylene glycol (PEG), a hydrophilic polymer, often employed as an NP coating. PEGylation of NPs has been shown to enhance their systemic circulation time by providing a 'stealth' cloak against immune recognition and minimizing non-specific protein binding, as well as improving QD solubility in aqueous environments.^{23,24} For example, Doxil is coated with PEG to improve circulation time.²⁵ Secondly, NPs must be

colloidally stable, which refers to the NP's ability to stay suspended within biological media, preventing particle aggregation. NPs designed with appropriate surface charges have shown improved colloidal stability, as the repulsion between similarly charged NPs keeps them well-dispersed.²⁶ Targeting specificity, another critical aspect of NP design, requires the precise interaction of NPs with the intended cellular or molecular targets. NPs that are able to only interact with the desired target minimize non-specific binding, leading to both enhanced therapeutic efficiency and reduced off-target damage.^{24,27} A common strategy to increase targeting ability in NPs is to include moieties such as antibodies, peptide, or small molecules on the NP surface that will direct NPs to conjugate to cells expressing the matching antigen. This paradigm can be extended to a multitude of protein-receptor combinations; for example, functionalizing a NP with folic acid has been a well-documented strategy for the targeting of cancer cells overexpressing folate receptors.²⁸ Taken together, these requirements highlight a final critical imperative within effective NP design, which is the ability to conjugate NPs with molecules that can modulate cellular function. Sufficient NP design should allow for drugs or growth factors, imaging agents, stealth targeting agents or other bioactive compounds to be attached to the NP surface (a process known as biofunctionalization) or encapsulated within the NP core.^{11,29} This ability is indispensable for drug delivery applications in particular, where the binding of these agents and/or controlled release at the site of action enhances therapeutic effectiveness and reduces negative off-target effects.³⁰

NPs can be broadly classified into two categories: hard and soft. This classification is based on the NP surface and the core's physicochemical properties, structural rigidity, and the way in which biomolecules are attached to or incorporated within the NP. Soft NPs include liposomes, micelles, emulsions, dendrimers, and other polymer or protein-based nanostructures. They are

currently well-studied, and they are the basis of more than quadruple the number of products compared to hard NPs.³¹ Soft NPs possess a flexible structure and central hydrophilic core that can be loaded with cargo, along with a surface amenable to cargo attachment. They are also usually synthesized with biodegradable materials such as lipids, enhancing their biocompatibility and making them good candidates for drug delivery. Indeed, lipid NPs have become well-known in the public eye as the carriers of the mRNA coronavirus (SARS-CoV-2) vaccines developed in response to the COVID-19 pandemic.³² However, while soft NPs have many advantages, they also have some limitations. Soft NPs tend to be larger than hard NPs, which limits their ability to penetrate dense tissues. They often lack inherent optical properties such as luminescence, which complicates applications that aim to use them for *in vivo* bioimaging/tracking. While their biodegradability is considered a strength, it is also a challenge when soft NPs break down prematurely.³³ Another concern is the propensity of soft NPs to aggregate, forming larger clusters that can hinder their functionality and limit their ability to effectively navigate biological systems.^{34,35}

On the other hand, hard NPs are characterized by a solid, non-flexible core, which provides a robust structure. The physicochemical properties of hard NPs is determined by their core and shell materials, and only the NPs's external surface is utilized for the attachment of cargo for the purpose of manipulating cell function. The attachment is typically achieved *via* passive absorption using electrostatic interactions, or through the formation of covalent bonds through pendant functional groups present on the NP surface. Specific examples include gold (Au) and silver (Ag) NPs, metal oxides, silica particles, and QDs. Although hard NPs have notably lesser biocompatibility when compared to soft NPs, their multifunctional capabilities extend beyond mere drug delivery, rendering them a compelling choice for pioneering novel applications in the

realm of nanobiotechnology. For example, iron oxide NPs have been applied in magnetic resonance imaging due to their superparamagnetic properties.³⁶ Meanwhile, QDs can achieve both drug delivery and bioimaging simultaneously, as they possess size-tunable photoluminescent emission.^{37,38} Overall, there remains much to be learned concerning the utilization of multifunctional hard NPs for the control of cellular behavior.

The work presented in this dissertation focuses on the development of novel NP materials for the controlled modulation of cellular behavior. We do this in the context of two new functional NP-bioconjugate systems: 1-the use of a new form of anisotropic AuNP for the photothermal-induced control of cellular membrane potential and 2-the employment of QDs for the multivalent display of growth factors for the enhanced induction of intracellular signaling and protein expression resulting in enhanced cellular water transport. These approaches both broaden our understanding of NP-cell interfaces but also pave the way for the continued development of NP-based tools for precise cellular modulation. Cumulatively, these works underscore the potential found in leveraging the unique properties of AuNPs and QDs as functional materials to modulate cellular behavior.

Specific Aims

Specific Aim 1: Photothermal-Enhanced Modulation of Cellular Membrane Potential Using Long-Wavelength-Activated Gold Nanoflowers.

The regulation of plasma membrane potential in mammalian cells is crucial for both physiological and pathological processes and is managed by a complex network of ion channels residing within the membrane. Within this aim, we seek to employ AuNPs to manipulate cellular biological functions, including the modulation of membrane potential. Photoexcitation of gold NPs tethered in proximity to the plasma membrane has been previously demonstrated to induce

membrane depolarization through localized heating of the AuNP surface and subsequent opening of voltage-gated sodium channels. However, past research has utilized spherical AuNPs (AuNS) with absorption in the 500–600 nm range for this purpose, which is not optimized for *in vivo* use due to the limited penetration depth of light in this optical window. In Specific Aim 1, we present the utilization of novel anisotropic-shaped AuNPs [gold nanoflowers (AuNFs)] featuring broad absorption extending into the near-infrared (NIR) region of the spectrum (~650–1000 nm) which can facilitate increased tissue penetration depth *in vivo*. The AuNFs are directly synthesized with bidentate thiolate ligands, which maintain the AuNF's morphology and colloidal stability while enabling conjugation to biomolecules. We delineate the characterization of the AuNF particles and exhibit their adherence to the plasma membrane upon bioconjugation to PEGylated cholesterol (PEG-Chol) moieties. The AuNF-PEG-Chol mediated the depolarization of rat adrenal medulla pheochromocytoma (PC-12) neuron-like cells more effectively than AuNS-PEG-Chol and unconjugated AuNS and AuNF when photoexcited at ~561 or ~640 nm. Additionally, we show that AuNF induction of depolarization does not negatively impact cellular viability. This aim explores the use of AuNPs and the tuning of AuNP surface moieties and physical characteristics as a promising nanomaterial for use in cellular depolarization and the spatiotemporal control of cellular activity.

Specific Aim 2: Multivalent Display of Erythropoietin on Quantum Dots Enhances Aquaporin-4 Expression and Water Transport in Human Astrocytes In Vitro.

As mentioned previously, the induction of intracellular signaling and protein synthesis by growth factors is vital for maintaining cellular physiology and homeostasis in mammalian cells. Specifically, within the brain's glymphatic system, aquaporin-4 (AQP4) membrane channels which are expressed in a polarized manner on astrocyte endfeet facilitate the clearance of waste

products through the transport of fluid and solutes. The glycoprotein erythropoietin (EPO) has been demonstrated to upregulate AQP4 expression *via* interaction with the EPO receptor and the subsequent downstream activation of the JAK/STAT signaling pathway. In this aim, we demonstrate a multivalent display of EPO on the surface of semiconductor QDs through polyhistidine-driven self-assembly that can achieve: 1) augmented activation of the JAK/STAT pathway; 2) a 1.8-fold enhancement in AQP4 expression in cultured primary human astrocytes (HA) compared to free EPO; and 3) a 2-fold increase in water transport rate in HA cells, as assessed by a calcein AM water transport assay. Importantly, the EPO-QD-induced augmented AQP4 expression does not negatively impact astrocyte viability. This aim is significant in relation to the potential applications of EPO-NP conjugates not only as research tools for understanding the glymphatic system but also as prospective therapeutics for modulating glymphatic system function. Overall, this aim pursues a novel concept for NP-mediated regulation of growth factor-induced protein expression.

Chapter 2: Gold Nanoparticles and Quantum Dots: A Topical Review on their Use for Modulation of Cellular Function

The field of nanomedicine has witnessed remarkable advancements over the past few decades, with NPs emerging as powerful tools to achieve the modulation of various aspects of cellular physiology. Among the diverse array of NPs that exist today, QDs and AuNPs have garnered significant attention due to their unique properties and potential applications. AuNPs, known for their tunable size, shape-dependent unique optical properties, and biocompatibility, have shown promise in modulating cellular activity and behavior.¹² On the other hand, QDs are luminescent semiconductor nanocrystals that exhibit size-dependent optoelectronic properties due to quantum effects from the trapped electrons within their small physical size, making them ideal candidates for use as trackable drug delivery scaffolds and imaging agents in biological systems.³⁹ Despite the promising potential of these NPs, some challenges persist, including issues related to solubility, stability, biodistribution, and long-term toxicity. This topical review aims to provide a comprehensive summary of AuNPs and QDs; the subsequent sections will explore in detail important considerations when developing AuNPs and QDs for use in biological applications, as well as cover some of the recent research efforts to harness their full potential in the realm of cellular modulation.

Gold Nanoparticles (AuNPs)

AuNPs are a type of NP that has garnered significant interest in the scientific community due to their unique optical properties and potential applications in various fields, including biosensing, biomedicine, electronics, and catalysis. In the field of nanomedicine, AuNPs have been recognized as an important tool for a multitude of biomedical applications, including drug delivery, imaging, photothermal therapy (PTT), and the treatment of severe diseases such as malignant cancer.⁴⁰ Their size tunability, on the size regime of biological molecules such as enzymes and

proteins, and their inert and non-toxic nature makes them an ideal candidate for biomedical applications. Furthermore, the ability to provide therapeutic benefits as well as acting as a probe for diagnostic imaging allows AuNPs to act as a multimodal agent, thereby enhancing our understanding of the progress of disease and treatment efficacy.⁴¹ The use of AuNPs in medicine dates back to ancient India and China, but it is only over the past several decades that AuNPs have gained attention from researchers due to their unique qualities and potential applications.⁴¹ Some of the most beneficial characteristics of AuNPs include their tunable size and shape-dependent physical properties. The size and shape of AuNPs can be controlled during synthesis, which in turn allows for the versatility in their optical and electronic properties. This tunability extends to their biocompatibility and the ease with which their surfaces can be modified, making them suitable for a variety of biomedical applications.⁴² Lastly, AuNPs can act as photothermal therapeutic agents, due to the localized plasmonic heating response of AuNPs when excited by an incident light beam.¹¹

There are several established methods of synthesizing AuNPs, each with its own set of benefits and considerations. The process by which AuNPs are synthesized will influence the resulting particles' physical structures. The Turkevich method is a very commonly used aqueous-based synthesis technique that involves the reduction of gold (HAuCl_4) using citrate. The reducing agent donates electrons to the gold ions, converting them into $\text{Au}(0)$ which aggregate into NPs. While this method is straightforward and efficient, it often results in AuNPs with a broad size distribution, with limited control over the developed particle shapes. Reaction conditions, such as temperature, pH, and reactant concentration can influence the size and shape of the AuNPs, but this control is often imprecise. An alternative chemical reduction method is the Brust-Schiffrin technique, which uses a two-phase system where gold salts are reduced in the organic phase using

sodium borohydride and then transferred into the aqueous phase using water-soluble thiol ligand. This synthesis method allows for AuNP stabilized with the thiol ligands form a protective layer around the NPs via strong Au-S bonding, which helps prevent aggregation and can be used as linkers for further surface modifications.^{43,44} Although this method allows better size control, the resulting size is limited to less than 10 nm. Additionally, there are less often used but various types of techniques have been studied. For example, other techniques utilize physical methods such as using a high-intensity laser to ablate a gold mass submerged in liquid; the gold atoms then aggregate to form NPs. An evaporation-condensation method of synthesis also exists, where gold is evaporated in a tube furnace at high temperatures, and the vapor is subsequently condensed to form NPs. Other physical methods include microwave or ultraviolet (UV) radiation.⁴¹ Yet another set of unusual approaches to AuNP synthesis uses biological organisms or biomolecules to reduce gold ions to AuNPs, where bacteria, fungi, yeast, or other microbes may act as both a reducing and stabilizing agent.^{43,44}

However, one of the most favored methods of AuNP synthesis today is the seed-growth method, due to its ability to generate high yields monodispersed AuNPs of controlled size and shape. This method involves two basic steps: first, the preparation of AuNP seeds, and then a subsequent growth phase where the AuNPs are enlarged layer by layer. The seed particles are typically generated by the rapid reduction of a gold precursor such as HAuCl_4 while in the presence of citrate for spheres or a stabilizing agent such as hexadecyltrimethylammonium bromide (CTAB) for other AuNP shapes. The rapid reduction by sodium borohydride ensures that the formation of uniform seed particles that serve as nucleation sites for the following growth step. In the growth phase, a “growth” solution containing a mild reducing agent (such as ascorbic acid) and more of the gold precursor is added to the seed solution with ligand (such as citrate). The less reactive

nature of the reducing agent allows the reaction to proceed at the surface of the gold seeds, leading to their layer-by-layer growth into larger AuNPs. This method is highly versatile and can be adapted to reliably produce AuNPs of different shapes and larger sizes *via* modification of the growth conditions and seeds formation.^{43, 45} Despite these benefits, the method is a complex one that involves a laborious and lengthy process with many synthesis agents (some of which can be cytotoxic, such as CTAB), as well as risking potential change in the shape of NPs during ligand exchange. Therefore, while the seed-growth method is the gold standard for AuNP synthesis, there has been some exploration into one-pot seedless methods.⁴⁶⁻⁴⁸

Once the AuNPs have been synthesized, post-synthesis surface functionalization is essential to prepare them for use in biological applications, with the goal being to improve solubility, stability of the AuNPs, and specificity to the desired targets. One common approach for surface modification involves the use of thiolated molecular linkers. Thiols have a strong affinity for gold, allowing them to firmly anchor to the AuNP surface; they can then be used to conjugate AuNPs with various biofunctional molecules.⁴⁹ Conjugation can be achieved through a variety of mechanisms, including hydrophobic interactions, electrostatic forces, covalent conjugation, dative covalent bonding, oligonucleotide hybridization, and photolabile linkages *via* molecular surface linkers. Biological moieties such as proteins, drugs, enzymes, or PEG can be attached to the AuNP surface through these various methods. Proteins such as targeting antibodies can be attached via covalent bonding using crosslinking agents, while drugs can be conjugated through the formation of stable amide bonds. PEGylation, the process of attaching PEG molecules to AuNPs, can enhance AuNPs' stability, biocompatibility, and resistance to protein adsorption, improving their suitability for *in vivo* applications. Lipids, such as cholesterol, can facilitate binding to the plasma membrane.¹¹ Each of these modifications can be tailored to the specific

requirements of the application, offering a high degree of flexibility and control over the properties and performance of the AuNPs.

Functionalized AuNPs have a wide range of uses in the fields of biosensing, diagnostics, imaging, PTT, and drug/gene delivery. Here, we explore uses of AuNPs that specifically focus on modifying or controlling cellular function. One of the most unique features of AuNPs are their surface plasmonic characteristics. This phenomenon, known as localized surface plasmon resonance (SPR), is a result of the strong resonant oscillation of the gold metal's conduction band electrons resonating with visible light frequencies. This oscillation then non-radiatively decays into heat. The SPR of a given AuNP is contingent on several factors, including the metal type, NP size and shape, and the dielectric constant of the surrounding environment, thereby bestowing a distinctive optical tunability to these nanostructures.^{50,51} As the size of the AuNP increases, there is a redshift in the maximum absorption of the surface plasmon due to increased scattering from a larger optical cross section. When these NPs aggregate or assemble, this maximum absorption redshifts further into the near-infrared (NIR) region, which is advantageous for use in biological tissue due to the ability of NIR light to penetrate more deeply within tissues. Interestingly, this phenomenon is particularly observed when the shape of the AuNPs is altered from spherical to an anisotropic shape such as stars or rod-like forms.⁵² This tunability of AuNPs has significant implications in biotechnology, particularly in the field of cancer treatment. Finally, AuNPs have high extinction coefficients on the order of $\sim 10^9 \text{ M}^{-1} \text{ cm}^{-1}$.⁴⁵ The photothermal properties of AuNPs, which allow them to efficiently convert absorbed light energy into heat, can be harnessed for PTT of cancers.

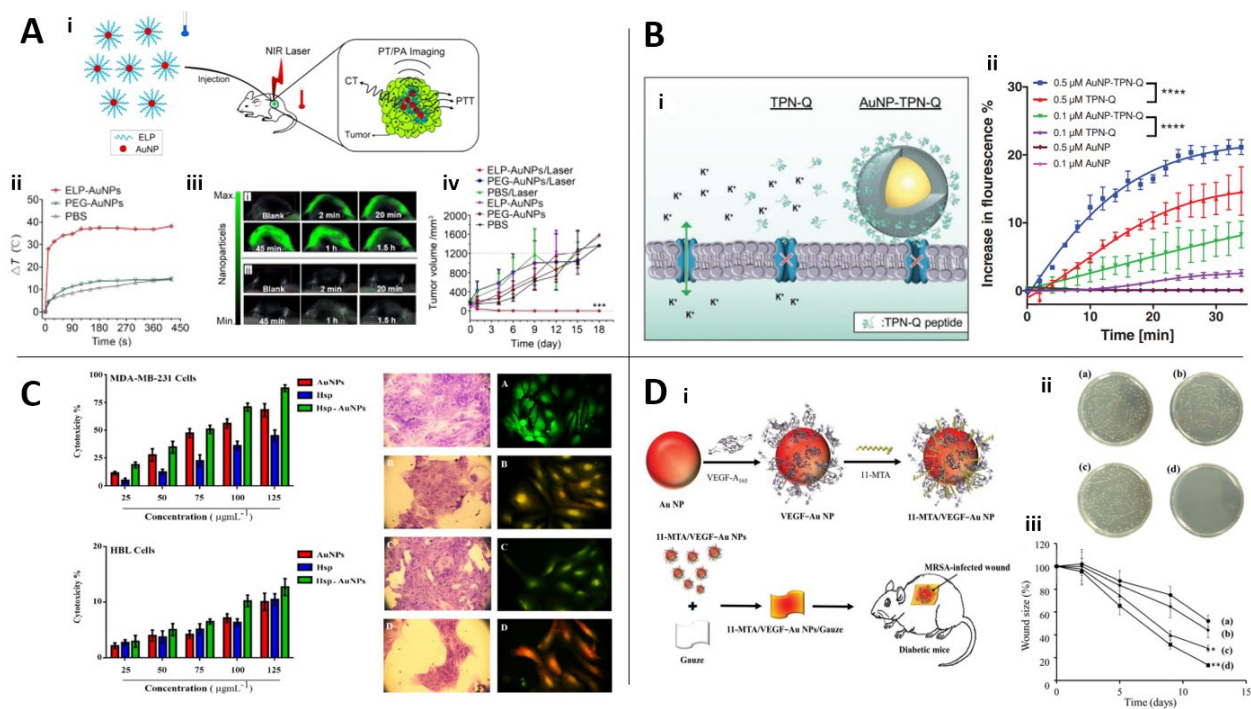


Figure 1. Uses of AuNPs for the control of cellular function seen within recent scientific literature. (A) (i) Schematic of the use of elastin-like polypeptide (ELP)-AuNPs, and their multimodal use for cancer imaging and photothermal therapy. **(ii)** Increase in temperature of C8161 tumors under laser irradiation (1.5 W) over time, within a mouse model that were injected at the tumor site with ELP-AuNPs or controls. **(iii)** Photoacoustic imaging of tumor tissue before and after (recorded from 2 min to 1.5 hr) injection of 18 μg ELP-AuNPs (top) or PEG-AuNPs (bottom). **(iv)** C8161 tumor growth after single-injection treatment with AuNPs and 7 min laser treatment at 808 nm, 1.5 W. ELP-AuNPs heating with laser treatment results in a lack of tumor growth compared to other experimental groups. ($p < 0.001$) Image adapted from Sun © ACS Publications (2017) Ref. [53] **(B) (i)** Schematic of an AuNP-tertiapin-Q (Au-TPN-Q) system used to depolarize PC-12 cellular membrane potential via the targeting of inward rectifier potassium channels (Kir) in a more effective manner than with monomeric TPN-Q alone. **(ii)** Time-resolved depolarization of cells incubated with AuNP-TPN-Q versus free TPN-Q, tracked using the voltage-sensitive probe oxonol. For concentrations of both 0.5 μM and 0.1 μM, AuNP-TPN-Q mediated significantly greater levels of membrane depolarization. ($p < 0.0001$) Image adapted from Muroski © WILEY-VCH Verlag GmbH & Co. KGaA, Weinheim (2019) Ref. [54] **(C)** Hesperidin-conjugated to AuNPs (Hsp-AuNPs) therapeutic treatment of human breast cancer MDA-MB-231 cells induce greater levels of apoptosis in MDA-MB-231 cells versus normal human breast epithelial cells (HBL-100). Right panel shows images of MDA-MB-231 cells treated with (a) non-treated, (b) treated with Hsp (c) treated with AuNPs and (d) treated with Hsp-AuNPs, which was the most effective therapy. Image adapted from Sulaiman © Springer Nature (2020) Ref. [55] **(D) (i)** Schematic representation of the preparation of dual-functional antimicrobial and proangiogenic AuNPs (11-MTA/VEGF-AuNPs) and their use in treating methicillin resistant *S. aureus* (MSRA)-infected wounds on diabetic mouse models. **(ii)** Colony formation of MSRA on luria bertani agar plates treated with (a) non-treated, (b) 11-MTA, (c) VEGF₆₀ -AuNPs, and (d) 11-MTA/VEGF-AuNPs. **(iii)** Decrease in size over time of wounds treated with (a) non-treated, (b) 11-MTA, (c)

VEGF₆₀ -AuNPs, and (d) 11-MTA/VEGF-AuNPs. (** p < 0.001). Image adapted from Wei © Royal Society of Chemistry (2019) Ref. [56]

The use of laser-stimulated AuNPs in plasmonic PTT is well documented, with many studies utilizing this aspect of AuNPs to develop methods for inducing hyperthermia to ablate tumor cells.⁵¹ One specific example from Sun *et. al.* conjugated elastin-like polypeptides (ELPs) to AuNPs for dual imaging and anti-cancer ablation capabilities. The group was able to demonstrate a 28 °C increase in temperature of C8161 cell tumors under 1.5 W laser irradiation of the ELP-AuNPs within 10 seconds, as well as a halt in tumor growth *in vivo* (Figure 1A).⁵³ Other researchers have focused on gentler uses of AuNP photothermal stimulation to heat the surface of cells by 1-2 degrees in order to achieve more subtle changes in physiology such as depolarization of the cellular plasma membrane.⁵⁷ The use of photothermal stimulation for the control of cellular membrane depolarization is explored further in Chapter 3.

However, the uses of AuNPs extend beyond their optical properties – due to the ease in which they can be externally modified with biological moieties and their biocompatible nature, they are excellent candidates to use as vehicles for drug and gene delivery applications. AuNPs exhibit a large surface to volume ratio, and thus a relatively large amount of drugs, vectors, and genes can be immobilized on the surface of AuNPs. There have been a wide variety of applications utilizing these advantages; one of the more unique approaches to modulating cellular function by Muroski *et. al.* has been the attachment of the honeybee venom protein tertiapin-Q to AuNPs (AuNP-TPN-Q) in order to target inward rectifier potassium channels on neuron-like differentiated PC-12 cells and induce effective plasma membrane depolarization (Figure 1B).⁵⁴ One of the most typical uses of AuNPs for drug delivery include the attachment of anti-cancer drugs to the surface of AuNPs to induce apoptosis in cancer cells. An example of this technique can be seen by the

work of Sulaiman *et. al.*, which conjugated hesperidin to AuNPs (Hsp-AuNPs) to overcome solubility and bioavailability difficulties with delivering monomeric hesperidin. The group was able to demonstrate increased levels of apoptosis (up to a 20% increase) when incubating Hsp-AuNPs with MDA-MD-231 human breast cancer cells versus free Hsp or control AuNPs, and significantly overall lower levels of cytotoxicity in normal human breast epithelial cells (Figure 1C).⁵⁵ The use of AuNPs as drug vehicles is not restricted to cytotoxic anti-cancer drugs, as AuNPs have also been explored to control angiogenesis as well. Wei *et. al.* attached both vascular endothelial growth factor-A₁₆₅ (VEGF) and the antimicrobial (11-mercaptoundecyl)-N,N,N-trimethylammonium (11-MTA) to AuNPs, producing dual-functional pro-angiogenic and antimicrobial NPs that could be applied to wounds. The group successfully showed that continuous treatment of infected wound sites in diabetic mice with 11-MTA/VEGF-AuNPs slowed growth of methicillin resistant *S. aureus* and significantly decreased wound sizes in comparison to control groups after 12 days (Figure 1D).⁵⁶ Notably, these various techniques are not necessarily distinct from each other; delivery techniques can also be combined with PTT for the formulation of AuNP-conjugated drugs that are actively released once the AuNP is heated via laser pulse.⁵⁸ Additionally, targeting moieties such as antibodies may also be placed on hard AuNP surfaces to improve the specificity of treatments. Overall, the unique properties of AuNPs, particularly their ability to conduct PTT and to carry drug cargo, provide exciting new avenues for biological applications involving the control of cellular functions.

Quantum Dots (QDs)

QDs are nanoscale semiconductor inorganic crystals, typically ranging in size from approximately 2 to 10 nm in diameter. These nanocrystals are characterized by a unique tripartite structure that includes a semiconductor core, a shell, and a layer of surface-coating ligands called

the cap. The core, which is responsible for the QDs' fundamental optical and semiconductor properties, is overcoated by a shell that acts as a physical barrier. This shell separates the core from the surrounding medium, suppressing surface defects by eliminating trap sites and binding up any the surface “dangling” bonds on the core that quench photoluminescence. This structural feature significantly enhances the optical properties of QDs, reducing photobleaching and blinking, and increasing quantum yield. Additionally, the shell helps to passivate the core and keep the core materials (which often contain cadmium) from leaching out into the surrounding medium. Within biological applications, the QD cap typically exists to improve biocompatibility and solubility in aqueous solutions. The capping ligands, which can include alcohols, primary amines, carboxylic acids, and thiols, play a major role in determining the QD's colloidal stability, solubility, particle size distribution, and particle morphology of the QDs. These ligands facilitate bioconjugation with a variety of biological molecules, including peptides, carbohydrates, DNA fragments, viruses, and natural products, through hydrophobic interactions or electrostatic and covalent coupling.⁵⁹ Additionally, while some metallic QD cores such as CdSe are considered cytotoxic due to their oxidative instability, capping ligands can decrease or even eliminate cytotoxicity when the QD is applied at nanomolar-order concentrations.^{60,61} QDs are characterized by their bandgap energy, which is the energy needed to excite an electron from one electronic band to a higher one. This process forms an electron-hole pair, or exciton, which emits energy as a fluorescent photon when it returns to its ground state. The QD gains unique electrical and optical properties when its size is in the range of 2-10 nm.^{62,63}

One of the more unique characteristics of QDs is the inverse relationship between QD size and energy band gap, known as the quantum size effect. This allows tuning of QDs' fluorescent color and absorbance range by varying its size. A QD's fluorescence can be tuned along a wide

wavelength range of 400–4000 nm through the variance of size, enabling measurement across the ultraviolet, visible, and near-infrared regions. As the size of the QDs decreases, the degree of confinement increases, which produces an exciton of higher energy and thereby increases the band gap energy. This results in emission towards the shorter wavelength blue region due to the high band gap energy; on the other hand, the fluorescence of larger QDs are shifted towards the red spectrum. Furthermore, QDs possess large absorption extinction coefficients, making them brighter probes within *in vivo* conditions where light intensities are severely attenuated by scattering and absorption. They also have high fluorescent quantum yields, an intrinsic property of fluorophores defined as the ratio of photons absorbed to photons emitted through fluorescence. Due to their inorganic nature, QDs are exceptionally resistant to light and chemical degradation, making them effective imaging probes over long periods. This means that QDs are unlikely to experience photobleaching, a phenomenon where luminescent material decomposes irreversibly due to optical excitation, leading to a decrease in fluorescence intensity.⁵⁹

Within the field of nanomedicine, QDs are primarily used for bioimaging, tracking, and sensing technologies, due to their bright emission and trackability. However, there has also been some interest in the use of QDs for the manipulation of cell function, typically in the form of drug delivery, where QDs can be utilized for both imaging and drug-carrying capabilities. QDs have the potential to serve as carriers of drugs or biomolecules due to their potential biocompatibility after ligand attachment, uniform size, and surface properties, making them highly suitable for a variety of biomedical and clinical applications. Recent research has demonstrated a growing interest in leveraging QDs as a promising instrument in drug delivery, either by using these QDs as direct carriers or by attaching them to specific drug entities.^{60,64}

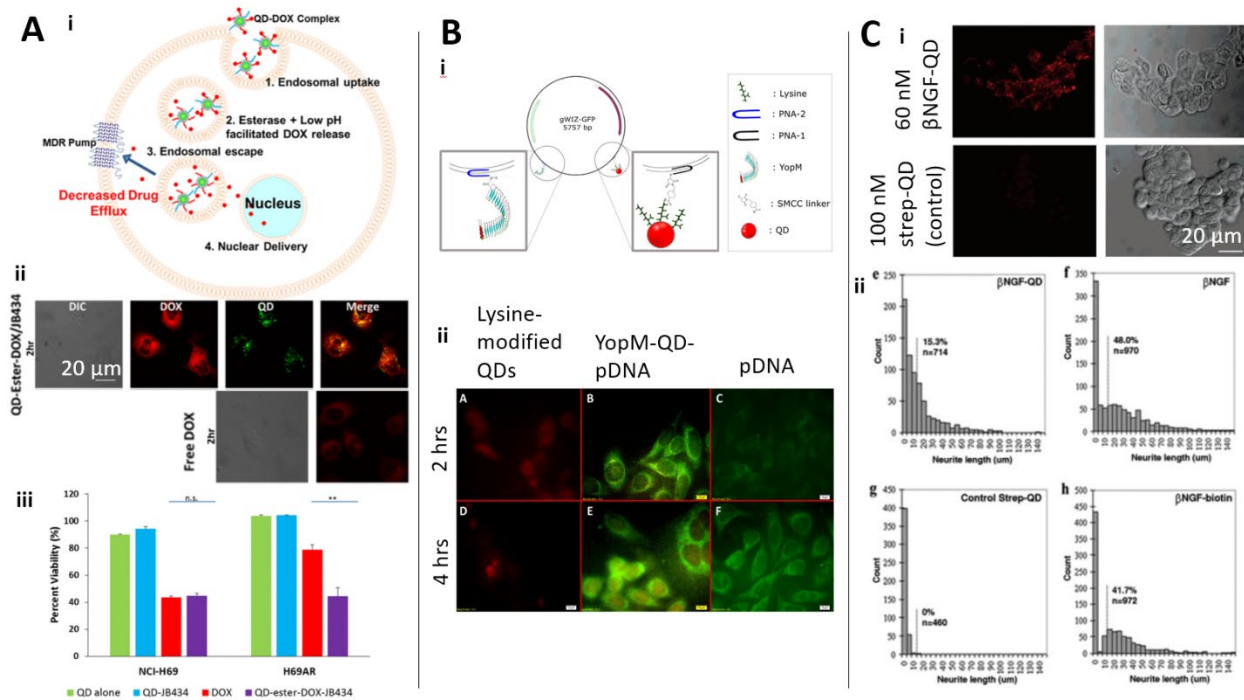


Figure 2. Uses of QDs for the control of cellular function seen within recent scientific literature. (A) (i) Schematic of QD-doxorubicin (QD-DOX) conjugated via an esterase-cleavable peptide (JB434) for the targeting of multidrug-resistant cancer cells. QD-DOX is brought into the cell via endosomal uptake, where esterases cleave the JB434 peptide, releasing DOX close to the nucleus instead of near membrane pumps. (ii) Confocal fluorescence imaging demonstrates greater uptake of QD-DOX into cells versus free DOX after 2 hours. (iii) QD-ester-DOX-JB434 bioconjugates display significant cytotoxicity in DOX-resistant H69AR cells, and equivalent cytotoxicity to free DOX in DOX-sensitive cells (NCI-H69). Image adapted from Sangtani © ACS Publications (2019) Ref. [65] (B) (i) Schematic of the YopM-QD-pDNA conjugate. pDNA contains encoding for green fluorescent protein. (ii) Qualitative analysis of successful pDNA transfection into HeLa cells, which can be seen via production of GFP reporter. Note the higher levels of fluorescence from cells transfected with YopM-QD-pDNA versus naked pDNA. Image adapted from Uğurlu © Elsevier (2020) Ref. [66] (C) (i) β NGF-QD effect on PC-12 cell differentiation into a neural-like cell type after 1 hr. (ii) Histograms demonstrating neurite growth in PC-12 cells after 3 days of exposure to different forms of β NGF or control (Streptavidin-QD). Here, β NGF-QD conjugates did stimulate limited neurite growth in PC-12 cells compared to β NGF or biotinylated β NGF. Image adapted from Vu © ACS Publications (2005) Ref. [67]

Perhaps the most common use of QD as a drug carrier is for the delivery of chemotherapeutic drugs to cancer cells. The utilization of QDs as nanoscaffolds for drug delivery is a logical choice given their capacity to be functionalized with multiple modalities, including targeting ligands like antibodies, and therapeutic pharmaceuticals. Moreover, the conjugation of

drugs to the QD surface can be engineered to facilitate controlled drug release under specific conditions, such as a designated temperature, pH, or enzymatic presence, thereby enhancing the therapeutic efficacy and specificity.⁵⁹ An illustration of the success of this tactic can be seen in the research completed by Sangtani *et al.* who developed a form of doxorubicin (DOX) conjugated to a QD via an esterase-cleavable peptide (JB434). The QD–ester–DOX–JB434 conjugate may be taken up into DOX-resistant cancer cells through the endosomal pathway. Commonly, drug-resistant cancer cells are able to expel drugs due to endosomal release near to membrane transporters which use ATP hydrolysis to expel drugs from the cytoplasm. However, QD–ester–DOX–JB434 conjugates can avoid expulsion due to the fact that DOX is cleaved by esterases within the endosomal pathway, leading to release closer to the nucleus and a subsequent increase in cytotoxicity within DOX-resistant cell lines (Figure 2A).⁶⁵ Here, the use of QDs has afforded significantly greater control over drug release and efficacy versus use of free drug molecules.

Gene delivery is another field that is beginning to employ QDs as well. Uğurlu and colleagues transfected plasmid DNA-containing green fluorescent protein-encoding sequences that were conjugated to QDs and *Yersinia* outer protein M (YopM) to improve localization into the cytoplasm and nucleus. They qualitatively observed higher levels of green fluorescent protein fluorescence as well as the presence of QDs within HeLa cells (red) in comparison to naked plasmid DNA transfected using a transfection reagent (Figure 2A).⁶⁶ However, it may be possible to employ QDs for even more varied approaches to controlling cellular behavior. The use of a QD as a delivery vehicle for growth factors to affect intracellular signaling is a nearly unexplored paradigm. A solitary publication by Vu *et al.* provides a proof-of-concept demonstration of QD-growth factor conjugate capabilities. In their study, they engineered a complex of the β subunit-neural growth factor (β NGF) and a QD, thereby illustrating the potential of ligand-QD assemblies

in modulating tyrosine kinase A-mediated cellular signaling pathways; in particular, they focused on the ability of β NGF-QDs to promote neuronal differentiation in PC-12 cells. While Vu's research group was able to demonstrate clear stimulation of neural differentiation compared to a streptavidin-QD control, they were unsuccessful in showing improved cellular signaling over monomeric β NGF (Figure 2C).⁶⁷

Although the use of QDs for bioimaging and sensing applications is widely established in the literature, QD's application has been explored less thoroughly for the purpose of improving our control over cell function. In particular, the potential benefits of QD-growth factor conjugation have not been investigated. In this thesis, we aim to bridge this technology knowledge gap by investigating the potential enhancements in growth factor efficacy when conjugated to QDs as a delivery scaffold, for the purpose of contributing to the advancement of nanotechnology in cellular manipulation.

Chapter 3: Photothermal-enhanced Modulation of Cellular Membrane Potential using Long Wavelength-activated Gold Nanoflowers⁶⁸

Reprinted with permission from Rogers, K. E., Nag, O. K., Susumu, K., Oh, E., & Delehanty, J. B. (2023). Photothermal-Enhanced Modulation of Cellular Membrane Potential Using Long-Wavelength-Activated Gold Nanoflowers. *Bioconjugate Chemistry*, 34(2), 405-413. Copyright 2023 ACS Publications.

Introduction

The plasma membrane plays a vitally important role in the preservation of cellular homeostasis and physiology. It separates the cytoplasm, organelles, and nucleus from the surrounding environment, creating an enclosed ecosystem of cellular machinery and nutrients while excluding toxic substances. In addition to maintaining the integrity of the intracellular environment, the plasma membrane also maintains an electrical potential (voltage) across its 5 nm thickness through the controlled regulation of ion movement through membrane-resident ion channels. The concentrations of potassium (K^+) and sodium (Na^+) ions within the cell are modulated by a series of embedded pumps and channels, which control membrane potential. Membrane potential helps to regulate normal cellular physiology (e.g., proliferation, differentiation, neuronal cell intercommunication) and great interest has emerged in the development of new nanoscale tools for the control of cellular membrane potential that can overcome some of the inherent limitations of current technologies such as patch clamp, microelectrodes, or pharmaceutical agents.⁶⁹⁻⁷³ For example, patch clamp is limited to the manipulation of single cells while microelectrodes do not afford single cell resolution/interrogation and drugs can have off-target toxic side effects.^{72, 73} New, noninvasive tools that can address some of these roadblocks are highly desired.

Functional NP bioconjugates are promising new materials for imaging, sensing, and the control of cellular function. Given their nanoscale size, NPs' physicochemical properties (e.g.,

catalytic activity, fluorescence, absorption, or scattering) can be taken advantage of in cellular applications through their bioconjugation and targeting to specific subcellular organelles.^{18,74} In particular, gold NPs (AuNPs) have shown great utility in both sensing and drug delivery applications.^{75,76} Recently, AuNPs have emerged as attractive materials for the controlled modulation of cellular membrane potential via their photothermal properties. We have previously demonstrated the utility of membrane-tethered 20 nm diameter spherical AuNPs (functionalized with PEGylated cholesterol) that were photostimulated with a 561 nm laser for the controlled, reversible initiation of action potentials in living neurons.⁷⁷ Heating of the AuNP surface transduced heat into the plasma membrane bilayer resulting in a modest increase (1–2 °C) in membrane temperature and opening of sodium ion channels. We further showed the ability to tune the efficiency of the system in a distance-dependent manner by controlling the length of the PEG linker/spacer.⁵⁷ Importantly, the modulation of membrane potential using these AuNP conjugates showed no impact on cellular health or viability. Photoresponsive AuNPs offer a number of advantages over genetically engineered channelrhodopsins (ChRs) for light-mediated control of membrane potential. First, AuNPs do not require cellular transfection or modification of germline DNA, which limits the utility of ChRs in vivo. Second, AuNPs have extinction coefficients ($\sim 10^9 \text{ M}^{-1} \text{ cm}^{-1}$)⁷⁸ that are orders of magnitude larger than ChRs ($\sim 10^4 \text{ M}^{-1} \text{ cm}^{-1}$).^{79,80}

Given the optical properties of biological tissues wherein the penetration of light is optimal in the NIR ‘tissue transparency’ (therapeutic) window ($\sim 650 - 1350 \text{ nm}$)⁸¹ due to minimal absorbance/scattering by biological molecules (e.g., hemoglobin), there is an ever increasing desire to realize new functional nanomaterials that can stimulate neurons in this NIR window. While spherical AuNPs have proven their utility for neuronal stimulation in the visible window, anisotropic shaped AuNPs, such as nanorods or nanostars, offer absorption profiles in the

expanded red or NIR/IR range. Heretofore, a critical challenge in Au nanorod/nanostar synthesis has been their limited long-term shape stability and the limited library of suitable surface-capping ligands with which to render the NPs biocompatible.

In this chapter, we describe a novel technique for the ‘seedless’ synthesis of anisotropic AuNPs we refer to herein as Au nanoflowers (AuNFs). We show that both AuNF size and shape can be iteratively controlled over the size range of ~20 – 500 nm by modulating various aspects of the growth conditions (e.g., the capping ligand:Au ratio, reaction acidity) while simultaneously controlling the nature of the functional group on the ligand termini. The AuNFs possess unique optical and photothermal properties compared to their gold AuNS counterparts. Specifically, while AuNS have a single absorption peak (surface plasmon resonance band), AuNFs have non-symmetric absorption features (with a combination of multiple absorption bands) due to their anisotropic shape and they more efficiently absorb incident photons (~10-fold greater) at longer wavelengths in the visible and near NIR region of the spectrum. We demonstrate the utility of AuNFs for the enhanced photoactivated depolarization of membrane potential. Compared to AuNS, AuNFs exhibit ~50% greater efficiency in the induction of membrane depolarization in PC-12 cells when tethered to the plasma membrane by a PEGylated cholesterol moiety. The magnitude of depolarization tracks directly with incident laser power when the NPs are excited at 640 nm. Our results demonstrate the flexibility of the new AuNF synthesis process and the utility of the materials in modulating plasma membrane potential when excited in the NIR window.

Materials and Methods

Synthesis of spherical AuNP (AuNS) in aqueous phase. AuNS were synthesized using a seed-growth method previously reported by us.⁷⁷ For 10 nm seed AuNS, 200 μ L of 100 mM tetrachloroauric (III) acid ($\text{HAuCl}_4 \cdot 3\text{H}_2\text{O}$) (2.0×10^{-5} mol) aqueous stock solution and 200 μ L of

100 mM of citric acid (2.0×10^{-5} mol) aqueous solution were added to 50 mL of deionized water and the reaction mixture was vigorously stirred at room temperature for 5 min. Then, 200 μ L of 200 mM *L*-ascorbic acid (4.0×10^{-5} mol) aqueous solution was added to the reaction mixture, followed by vigorous stirring for 30 min. Next, the growth solution was prepared with 0.4 mM tetrachloroauric (III) acid and 0.8 mM sodium citrate in 50 mL of deionized water. To synthesize 20 nm AuNS, 7 mL of seed AuNS solution was added to the growth solution followed by addition of *L*-ascorbic acid (2 mM final concentration). The reaction mixture was stirred for 3 h at room temperature and kept without stirring for an additional 24 h to complete the AuNS growth and deactivate the *L*-ascorbic acid. The successful synthesis of AuNS was confirmed by a red shift of the surface plasmon band peak and the decrease of the ascorbic acid and aurate peaks in the UV region (< 300 nm) using UV-vis spectroscopy. The final AuNS sizes were confirmed by TEM and DLS measurements.

Seedless one-pot synthesis of gold nanoflower (AuNF) in aqueous phase. We developed a novel method of AuNF synthesis using thioctic acid (TA)-based ligands, *L*-ascorbic acid as reducing agent, and sodium hydroxide for pH-dependent control of the AuNF cluster size in aqueous phase.⁴⁷ For 20 nm AuNF, 200 μ L (2.0×10^{-5} mol) of 100 mM tetrachloroauric (III) acid ($\text{HAuCl}_4 \cdot 3\text{H}_2\text{O}$) aqueous stock solution, 100 μ L of 2M NaOH and 100 μ L of 100 mM TA stock solution were added to the 50 mL of deionized water. The reaction mixture was vigorously stirred at room temperature for 5 min, and the desired amount of freshly prepared 200 mM *L*-ascorbic acid aqueous solution ($6.0 \times 10^{-5} \sim 2.0 \times 10^{-4}$ mol) was added to the reaction mixture, followed by stirring for the next 3 h and maintaining for additional 24 h at room temperature for aging without agitation.

Ligand exchange of AuNPs with TA-PEG-COOH/TA-PEG-Methoxy. In preparation for the modification of the AuNS and AuNFs with PEG-cholesterol, the AuNPs were first ligand-exchanged with mixed ligands of 30% TA-PEG-COOH (molecular weight of PEG ~600 g/mol) and 70% TA-PEG-methoxy (molecular weight of PEG ~550 g/mol) to modulate fixed amount of COOH functional group on the surface. Briefly, 10 mL of AuNPs (AuNS and AuNFs with absorbance ~1 O.D. at peak position) was mixed with 100 μ L of 100 mM ligand stock solution, and the solution was adjusted to pH 8 using NaOH. The reaction solution was stirred for 8 h, and the AuNPs dispersions were purified from free ligands through multiple washes using a centrifugal membrane filtration device (50 kDa molecular weight cut-off) and deionized water.

Gel electrophoresis. Gel electrophoresis experiments were performed on a 1% agarose gel using TBE (tris borate EDTA; 100 mM Tris, 83 mM boric acid, 1 mM EDTA, pH 8.3). NP samples were prepared to 1 nM concentration and mixed with a 10% glycerol solution prior to loading. The gel was run at 8 V/cm for 30 min and imaged using white light on a Kodak Gel Logic 2200 imaging system.

UV-Vis Spectroscopy. Absorption spectra (extinction spectra) were recorded using a Shimadzu UV-1800 UV-vis spectrophotometer to monitor the changes of spectra before and after cholesterol conjugation on AuNPs. Given the small size of the AuNPs and no scattering signal, we use the term “absorption” spectra for the resulting UV-vis spectroscopy here. The concentration of AuNPs was measured using the molar extinction coefficient of $1.1 \times 10^9 \text{ M}^{-1} \text{ cm}^{-1}$ at 523 nm for AuNS and $9.3 \times 10^8 \text{ M}^{-1} \text{ cm}^{-1}$ at 618 nm for AuNF.

Transmission electron microscopy (TEM) and scanning electron microscopy (SEM). Structural characterization and elemental analysis of AuNPs was carried out using a JEOL 2100-LaB6 analytical high-resolution transmission electron microscope with a 200 kV accelerating voltage.

Samples for TEM and SEM were prepared by spreading a drop (5 to 10 μL at 1 nM) of AuNPs dispersion onto an ultrathin carbon/holey support film on a 300 mesh Au grid (Tedpella, Inc.) and allowing it dry. Individual particle sizes were measured using a Gatan Digital Micrograph (Pleasanton, CA). Average sizes along with standard deviations were extracted from analysis of at least 50-100 NPs.

Dynamic light scattering. Dynamic light scattering (DLS) measurements were carried out using a ZetaSizer NanoSeries equipped with a HeNe laser source ($\lambda = 633 \text{ nm}$) (Malvern Instruments Ltd, Worcestershire, UK) and analyzed using Dispersion Technology Software (DTS, Malvern Instruments Ltd, Worcestershire, UK). Similar concentration of TEM samples were loaded into disposable cells and data were collected at room temperature. All the samples were prepared in $0.1 \times$ PBS buffer (pH 7.4). For each sample, the autocorrelation function was the average of five runs of 30 seconds each (repeated about three to six times). CONTIN analysis was then used to determine the NPs in a view of number profile versus hydrodynamic size for the dispersions studied.

Conjugation of AuNPs to NH₂-PEG2000-Chol and NH₂-PEG2000-FITC. AuNF and AuNS were capped with thioctic acid (TA) and covalently conjugated to NH₂-PEG2000-Chol (cholesterol, for membrane tethering) and NH₂-PEG2000-FITC (fluorescein isothiocyanate, for visualization) using carbodiimide chemistry. Both NH₂-PEG conjugates were provided by NANOCS. Briefly, a solution of AuNS or AuNF was added to 1-ethyl-3-(3-dimethylaminopropyl) carbodiimide (EDC) and N-hydroxysuccinimide (NHS); NH₂-PEG2000-Chol and NH₂-PEG2000-FITC dissolved in H₂O were added at a 7:3 ratio of NH₂-PEG2000-Chol and NH₂-PEG2000-FITC. The solution was stirred in the dark at room temperature for 2.5 hours. Afterward, the reaction was purified using a PD10 column. Conjugation of the complex was confirmed through fluorescence spectra using a

RF-6000 Spectrofluorophotometer (Shimadzu Scientific Instruments) by excitation at 488 nm for direct excitation of the FITC. Also, the conjugation was confirmed through size retention analysis by agarose gel electrophoresis and DLS.

Cell culture. Rat adrenal medulla pheochromocytoma (American Type Culture Collection (ATCC, product no. CRL-1721) (PC-12 cells)) were cultured using growth medium (RPMI-1640, Millipore-Sigma) supplemented with 5% fetal bovine serum (ATCC), 10% heat-inactivated horse serum (ATCC), and 1% (v/v) antibiotic-antimycotic (Sigma). For differentiation, PC-12 cells were plated on 35 mm MatTek dishes (MatTek, 14 mm, #1 coverglass growth surface) that had been pre-coated with 50 $\mu\text{g}/\text{mL}$ of human collagen IV (Millipore-Sigma). Cell density was $\sim 7 \times 10^4$ cells/mL. The plated PC-12 cells were grown in differentiation medium consisting of RPMI-1640, 1% heat-inactivated horse serum, and 200 ng/mL nerve growth factor (NGF, from Sigma) and developed a neuron-like morphology with neurite projections once differentiated. Experiments involving PC-12 cells were conducted within 4-5 days after cell plating, once NGF-induced differentiation had occurred. Cultures were maintained in T25 flasks and incubated at 37°C under a 5% CO₂ humidified atmosphere and passaged every 3-4 days at 75-85% confluency. All cells used in this study were between passages 3 and 20.

Demonstration of AuNP-PEG-Chol/FITC localization to the plasma membrane. Differentiated PC-12 cells were incubated with AuNPs (3 nM) for 20 minutes at room temperature. They were gently washed and then incubated with 2 μM Lissamine™ Rhodamine B 1,2-dihexadecanoyl-sn-glycero-3-phosphoethanolamine (Rhodamine-PE, ThermoFisher) for 10 minutes at room temperature to counterstain the plasma membrane. The cells were excited with the 488 nm and 561 nm lasers and images were captured using fluorescence confocal microscopy.

Characterization of AuNP-PEG-Chol-mediated membrane potential depolarization.

Differentiated PC-12 cells were incubated with 100 μ L of the potentiometric dye DiSBac2(3) (Life Technologies) (1 μ M in LCIS) for 5 minutes at 4°C. After staining, cells were gently washed with Dulbecco's phosphate-buffered saline (DPBS). PC-12 cells were then incubated with a solution of AuNPs in LCIS for 20 minutes at room temperature, then washed again to remove any unbound NPs. During the experiment, laser-induced plasmonic heating of AuNPs was achieved by laser excitation every 2 minutes over a 20 minute time period. The laser excitation wavelength (561 nm or 640 nm) and power density used were the experimental variables. Cells were illuminated in scanning mode for 500 ms using the following acquisition settings: 0.19 μ m² focused spot size, 2.2 μ s/pixel, total image size 512 \times 512 pixels, leading to a physical image size of 0.21 x 0.21 mm). Directly after each laser excitation of the AuNPs, images of the cells were captured at 561 nm using the DiSBac2(3) dye was imaged by excitation with 488 nm laser (0.3% laser power; approximately 2.8 x 10³ mW/cm²) and the emission collected with a Texas Red filter (542-582 nm) to record fluorescence emission at each time point. Image analysis was performed on each image and the fluorescence intensity of each cell at each timepoint was recorded and normalized to the fluorescence value at 0 minutes. This allowed for the quantitation of potentiometric change within the cells due to heating of the AuNPs at different laser wavelengths and intensities. For each combination of laser excitation wavelength and power density, a control experiment was also performed where cells were incubated with LCIS alone instead of an AuNP solution, which were used to normalize the graphical data.

Cellular cytotoxicity of AuNPs in PC-12 cells. Differentiated PC-12 cells were incubated with 1 nM of AuNPs for 20 minutes at room temperature. The cells were rinsed with LCIS and stained with a live/dead cell viability assay kit (Thermo Fisher) according to manufacturer instructions.

Calcein-acetoxymethyl (AM) (0.4 μM) and ethidium homodimer (0.2 μM) were dissolved in LCIS and incubated with cells for 30 minutes at 37°C. PC-12 cells were then subjected to the same AuNP labeling and laser conditions as described above in the cellular depolarization experiments with laser power set to $2.5 \times 10^4 \text{ W/cm}^2$ (561 nm) or $6.3 \times 10^3 \text{ W/cm}^2$ (640 nm). During this time, the calcein AM signal for live cells was also captured via a brief excitation at 488 nm (2.2 μs exposure at $1.3 \times 10^3 \text{ W/cm}^2$), while the ethidium homodimer signal was captured during the aforementioned laser excitation at 561 nm. Cellular viability was determined by counting calcein (live) or ethidium homodimer (dead) dead cells. Viability was reported as the percentage of live cells compared to the total cell count.

Microscopy and Image Analysis. All imaging was performed using a Nikon A1RSi laser scanning confocal imaging system. The following imaging settings were used (laser excitation/dichroic/emission range): AuNF-FITC-Chol/AuNS-FITC-Chol, 488 nm/510 nm/500-550 nm; ethidium homodimer and Rhodamine-PE, 561 nm/595 nm/570-620 nm. Each channel was imaged sequentially to prevent bleed-through between the channels. Image analysis and image preparation was done using NIS-Elements AR (ver. 4.30.02).

Statistical Analysis. Univariate analysis of variance (ANOVA) was used to analyze the data utilizing GraphPad Prism 7.0 software for Windows (La Jolla, CA). Average values were calculated as mean \pm standard error of mean. A probability of significance of $p < 0.05$ was accepted.

Results and Discussion

Synthesis and characterization of AuNF-PEG-Chol and AuNS-PEG-Chol.

Our goal in this study was to characterize a new synthesis method for the production of anisotropic AuNFs that could be used for the photoactivated depolarization of membrane potential in electrically excitable cells (Figure 3A). The novel synthesis technique is ‘seedless’, using bidentate thiolate ligands (disulfide form used here) to yield anisotropic NPs. Typically the synthesis of NPs of this type involves binding ligands and reducing agents. In our approach detailed here, we reduced aurate ions with ascorbic acid in the presence of TA-based bidentate ligands to produce NPs with a three-dimensional branched structure, referred to herein as gold nanoflowers (AuNFs). For this study, we combined TA ligands with aurate ions at a ratio of 1:2 (ligand:aurate ion) to produce AuNFs with a diameter of 20 ± 2 nm with ~6 to 7 lobes or ‘pods’ formed on the NP surface. High resolution transmission electron microscopy imaging confirmed the excellent crystallinity of the AuNF materials (Figure 3B). The absorption spectrum of the AuNFs showed the distinctive broad, red-shifted, long wavelength absorption due to the additional surface plasmon band of the protruding pods compared to 520 nm absorption peak of AuNS. The colloidal color of the AuNFs was tin blue and AuNS was red wine, reflecting their long wavelength absorption (Figure 3C).

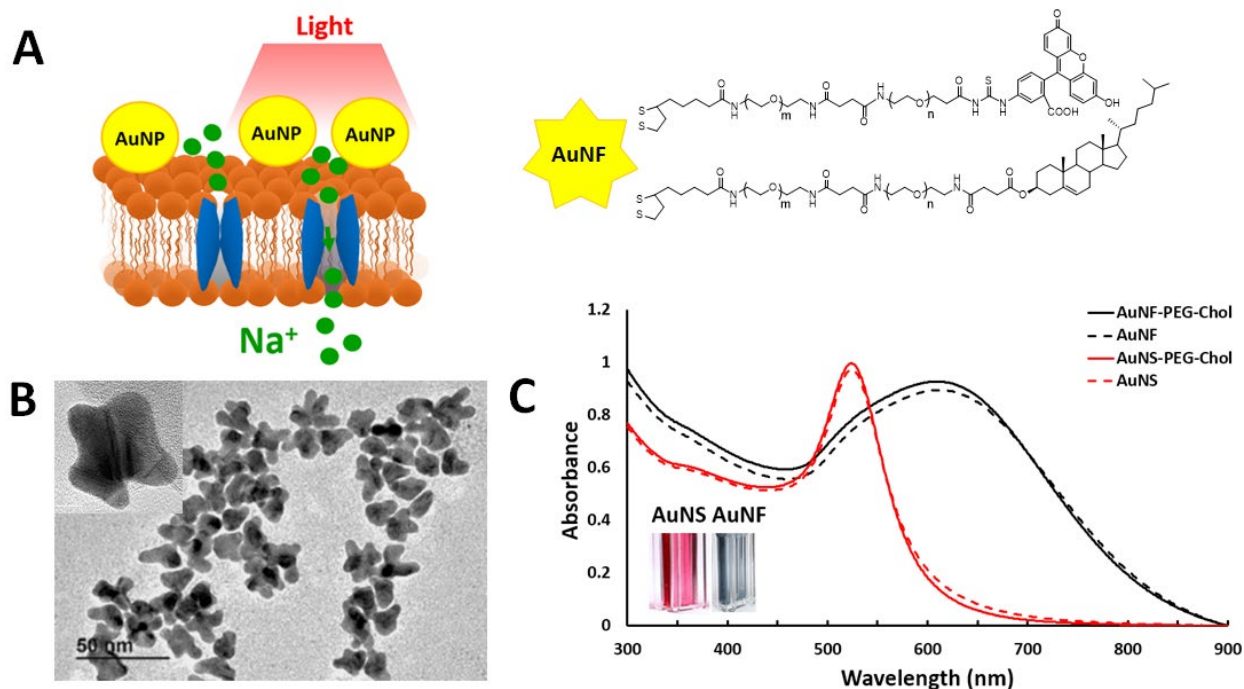


Figure 3. Characterization of AuNF and AuNF-PEG-Chol conjugates. (A) Schematic of photothermal excitation of AuNPs appended to plasma membrane by cholesterol moiety and opening of ion channels. Photoactivated membrane depolarization occurs via opening of voltage-gated sodium channels (left). Schematic of AuNF capped with PEGylated ligands that terminate in fluorescein (for visualization) or cholesterol (for membrane tethering) (right). (B) TEM of as-synthesized AuNFs demonstrating their unique anisotropic shape. The average size of the AuNFs is 20 ± 2 nm. (C) Absorbance spectra of unconjugated and cholesterol-conjugated AuNS (dashed and solid red traces) and AuNF (dashed and solid black traces) showing the significant red-shift of the AuNF absorbance spectra. Inset shows the visual color of the AuNS (red) and AuNF (tin blue).

Ligand exchange was performed on the AuNFs using a mixture of 30% TA-PEG-COOH (molecular weight of PEG ~600) and 70% TA-PEG-OCH₃ (molecular weight of PEG ~550) to modulate the surface functional groups. The terminal carboxylic acid functional group in TA-PEG-COOH was added for use in NP-ligand conjugation (*via* covalent bonding between carboxylic acid and amine groups in targeted molecules). The TA-PEG-methoxy ligand was added as the majority ligand to mediate solubility of AuNFs in aqueous solutions and to prevent the aggregation of cholesterol-functionalized AuNFs. Meanwhile, AuNS were synthesized as previously described

as a control to compare with AuNF but with the same ratiometric mixture of ligands used for AuNF as described above.^{57,77}

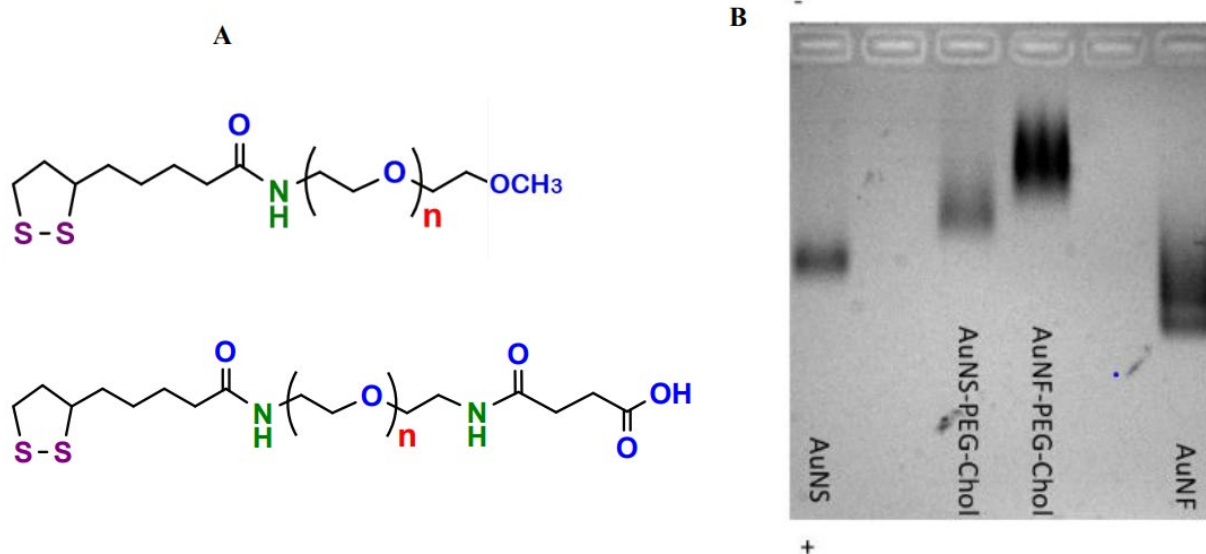


Figure 4. Capping ligands and AuNP conjugation. (A) Ligand structure for AuNPs. TA-PEGMethoxy (top) and TA-PEG-COOH (bottom). (B) Gel electrophoresis characterization of AuNF-PEG-Chol, AuNS-PEG-Chol, AuNF, and AuNS. AuNF-PEG-Chol and AuNS-PEG-Chol show slower migration in the gel towards the positive electrode compared to non-Chol derivatives due to their enlarged colloidal size imparted by the addition of the PEG-Chol ligand.

After the ligand exchange, we further modified the NPs by adding NH₂-PEG2000-Chol (amine-terminated PEG-cholesterol, for membrane tethering) and NH₂-PEG2000-FITC (fluorescein isothiocyanate, for visualization) to AuNF-PEG-Chol and AuNS-PEG-Chol (Figure 3A). Gel electrophoresis showed that the conjugated particles exhibited slower electrophoretic mobility than the unconjugated NPs (Figure 4), indicating successful bonding between TA-PEG-COOH and NH₂-PEG-Chol. As anticipated, negatively charged AuNS and AuNF (with TA-PEG-COOH) showed clear, rapid mobility toward the anode (+). However, after conjugation with PEG-Chol (and the resulting consumption of negatively charged free carboxyl groups), the AuNF-PEG-Chol and AuNS-PEG-Chol exhibited shorter migration toward the anode, confirming the decrease

in negative surface charges as a result of conjugation. Next, DLS was used to estimate the hydrodynamic size and particle concentration of AuNF and AuNS before and after conjugation to PEG-Chol. The average hydrodynamic sizes of both the AuNF-PEG-Chol and AuNS-PEG-Chol were measured to be ~36 nm which is ~5 nm larger than the unconjugated particles (Table 1). This increase in particle diameter can be attributed to the conjugation of PEG-Chol on the surface of the particles, changing the colloidal size of the AuNPs. Finally, zeta potential characterization of the AuNPs showed that particle surface charge changed from -39.3±4.8 mV (AuNS) and -32.5±2.7 mV (AuNF) to -22.8±0.2 mV and -16.0±2.8 mV for AuNS-PEG-Chol and AuNF-PEG-Chol, respectively (Table 1). Additionally, conjugation had no effect on the spectral absorbance profiles of the AuNPs (Figure 3C). Taken together, these data provide strong evidence of the successful conjugation of PEG-Chol onto the surface of AuNS or AuNF. The calculated extinction coefficient of AuNF assuming 100% reaction yield in the synthesis of 20 nm AuNF (based on the NP size by TEM and considering the original amount of Au used), was $\sim 9.3 \times 10^9 \text{ M}^{-1} \text{ cm}^{-1}$ at peak position (~618 nm) which is slightly larger than that observed for 20-25 nm gold nanostars ($\sim 6-7 \times 10^8 \text{ M}^{-1} \text{ cm}^{-1}$) and 20 nm AuNS used here ($\sim 1.1 \times 10^8 \text{ M}^{-1} \text{ cm}^{-1}$ at ~ 523 nm).^{82,83}

Table 1. Characterization of AuNPs.

| Sample Name | D _{TEM} ¹ Size | D _{DLS} ² (nm) | Z-Potential (mV) | ϵ^3 (M ⁻¹ CM ⁻¹) | SPB ⁴ peak (nm) |
|---------------|---------------------------------------|---------------------------------------|---------------------|---|-------------------------------|
| AuNS | 20 nm | 31.7±0.7 | -39.3±4.8 | 1.1 x 10 ⁸ | 523 |
| AuNS-PEG-Chol | 20 nm | 36.2±0.9 | -22.8±0.2 | 1.1 x 10 ⁸ | 523 |
| AuNF | 20 nm | 30.9±0.3 | -32.5±3.3 | 9.3 x 10 ⁹ | 618 |
| AuNF-PEG-Chol | 20 nm | 36.9±0.8 | -16.0±2.8 | 9.3 x 10 ⁹ | 618 |

¹ Average diameter of NPs measured by TEM

² Average hydrodynamic size of AuNPs measured by DLS

³ Extinction coefficient of AuNS (at 523 nm) and AuNFs (at 618 nm)

⁴ Surface plasmon band

Tethering of AuNF-PEG-Chol and AuNS-PEG-Chol to the plasma membrane.

We first determined the ability of the cholesterol-functionalized NPs to specifically label the plasma membrane bilayer (Figure 5). Nerve growth factor (NGF)-differentiated pheochromocytoma cells (PC-12) derived from rat adrenal medulla were plated on collagen-IV coated coverslip glass and were subsequently incubated for 20 min at room temperature with 3 nM AuNS or AuNF or their corresponding PEG-Chol conjugates. The NPs were also labeled with PEG-FITC for visualization by fluorescence imaging. The cells were counterstained with the fluorescent membrane marker, Rhodamine-PE (see Methods), to confirm localization of the NP-Chol conjugates to the plasma membrane. Figure 5 shows the resulting fluorescence micrographs of PC-12 cells after labeling with the NP-Chol-FITC conjugates. Figure 5 A, B shows the minimal degree of non-specific binding of the AuNPs in the absence of the PEG-Chol tether on the AuNPs. Pearson's colocalization analysis revealed colocalization coefficients of 0.29 and 0.37 for the AuNS-PEG-FITC and AuNF-PEG-FITC conjugates, respectively, with the Rhodamine-PE membrane marker. Conversely, the AuNS-PEG-Chol-FITC and AuNF-PEG-Chol-FITC conjugates exhibited localization coefficients of 0.87 and 0.91, respectively, demonstrating the highly efficient labeling of the plasma membrane mediated by the Chol moiety (Figure 5 C, D). These results are consistent with our previous studies demonstrating the efficiency of the Chol-based tethering strategy for appending AuNPs to the plasma membrane.^{57,77}

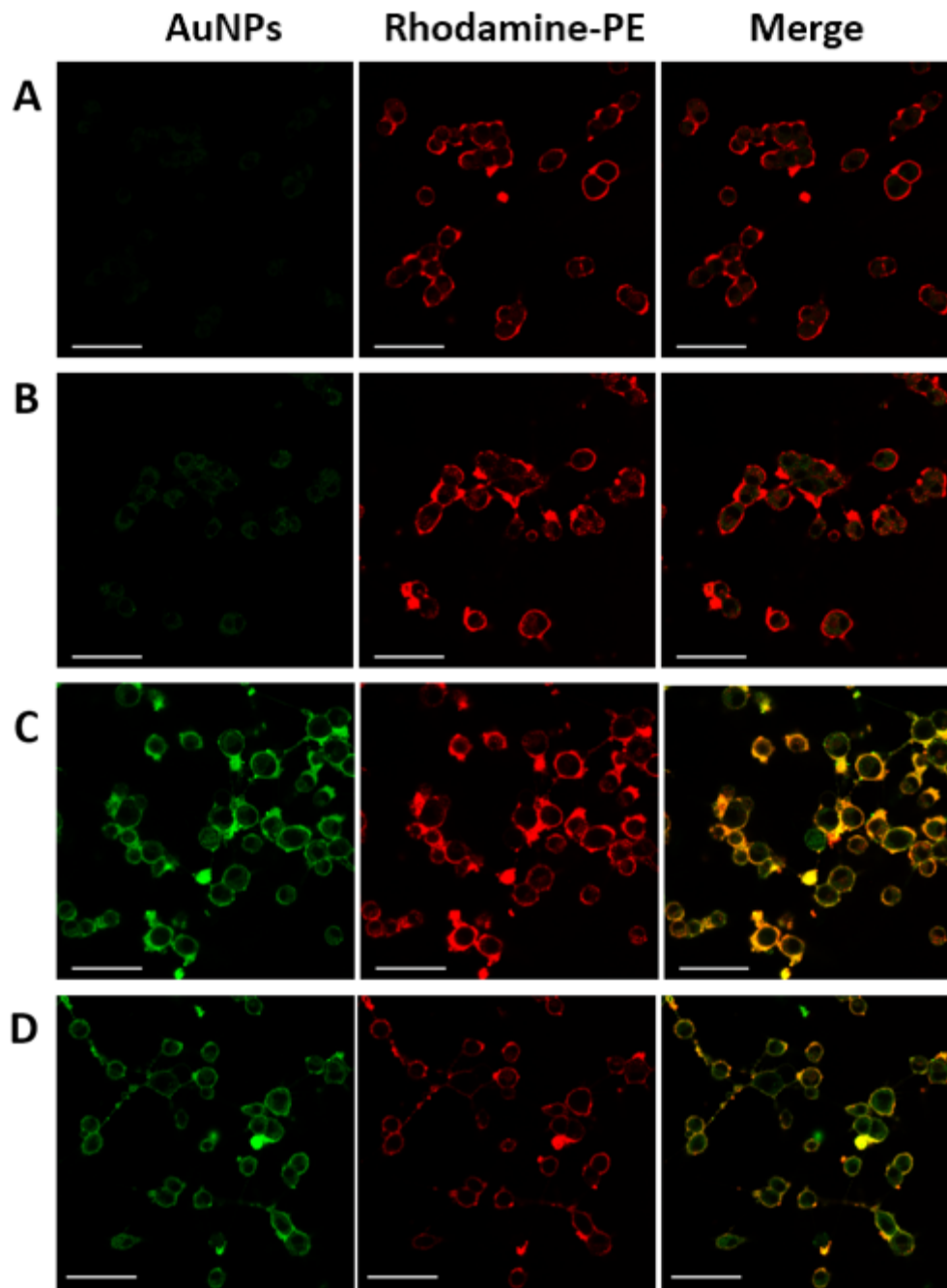


Figure 5. Localization of AuNS-Chol and AuNF-Chol conjugates to the plasma membranes. PC-12 cells were labeled with AuNPs (3 nM) and Rhodamine-PE (2 μ M). FITC dye conjugated to AuNS-PEG-Chol and AuNF-PEG-Chol was excited using 488 nm laser and Rhodamine-PE was excited with 561 nm laser. The images show the minimal nonspecific binding of the Chol-unconjugated AuNPs to the plasma membrane while the AuNP-Chol conjugates exhibit specific labeling that is largely colocalized with the Rhodamine-PE membrane marker (merged images). Panels show cells incubated with (A) AuNS-PEG-FITC, (B) AuNF-PEG-FITC, (C) AuNS-PEG-Chol-FITC, and (D) AuNF-PEG-Chol-FITC. Scale bar, 50 μ m.

Depolarization of membrane potential via photoexcitation of AuNS-PEG-Chol and AuNF-PEG-Chol conjugates.

We next investigated our hypothesis that the anisotropic properties of the AuNF-PEG-Chol conjugates would enable improved photothermal-induced membrane depolarization compared to AuNS-PEG-Chol, particularly in the NIR excitation window. PC-12 cells were labeled with AuNS-PEG-Chol or AuNF-PEG-Chol conjugates as well as the slow-response potentiometric probe DiSBAC₂(3), which we have used previously to track the distance-dependent nature of membrane depolarization of AuNS-PEG-Chol conjugates.⁵⁷ DiSBAC₂(3) is initially localized to the plasma membrane bilayer; depolarization causes an influx of the anionic probe into the cytosol where it binds to intracellular proteins, resulting in an increase in intracellular fluorescence that tracks with the magnitude of membrane depolarization.^{57,84} The fluorescence response was imaged every 2 min for 20 min and expressed as the average fluorescence per cell, normalized to the starting baseline fluorescence (100%). Thus, a normalized fluorescence intensity above 100% indicates an increase in fluorescence corresponding to an increase in membrane depolarization. In some instances, control cells (not incubated with any AuNPs) showed a very modest time-dependent increase in probe fluorescence signal above baseline (<10% over the 20 min experimental time course); these values were subtracted from the appropriate AuNP signals at each time point.

We first characterized the magnitude of photoinduced membrane depolarization mediated by the AuNS-PEG-Chol and AuNF-PEG-Chol conjugates when cells were incubated with AuNPs at a fixed concentration (1 nM of AuNPs) and subsequently photoexcited at either 561 nm or 640 nm at various laser power densities (Figure 7, indicative timelapse images in Figure 6). The data

showed that while the depolarization tracked with both increasing laser power density and time, there were clear differences in the magnitude of the depolarization response depending on the AuNP material, excitation wavelength, and laser power density. When excited with a 561 nm laser at a power density of $2.5 \times 10^4 \text{ W/cm}^2$, there was negligible difference in the response between the AuNS and AuNF conjugates (Figure 7A). This is consistent with the comparable absorption cross sections of the materials at 561 nm (Figure 7C). However, when excited at 640 nm, the AuNF-PEG-Chol conjugates exhibited ~50% greater depolarization efficiency over the 20 min time course (Figure 7B). When the laser power density was decreased ~4fold to $6.3 \times 10^3 \text{ W/cm}^2$, a similar trend was observed, albeit with a lower overall magnitude of depolarization response as expected (Figure 7 C, D). These data are consistent with the significantly larger absorption cross section of the AuNF materials in the NIR. Similar to our previous reports using AuNS, the estimated photothermal heat generated by our laser system was on the order of 1 °C, thus we do not expect any shape change nor membrane disruption.^{57,77}

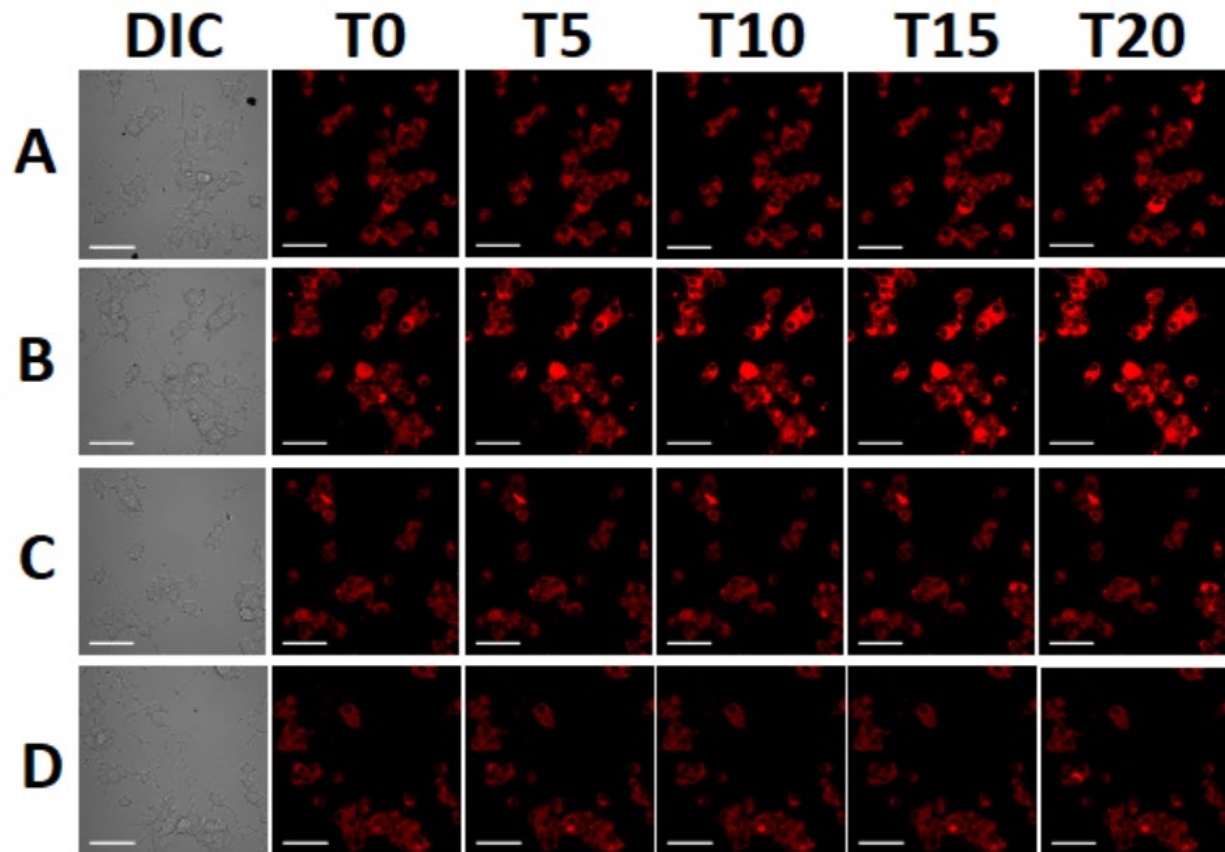


Figure 6. Timelapse images of AuNF-Chol and AuNS-Chol mediated membrane depolarization. Data show the NP-mediated depolarization response in PC-12 cells at time points: 0 minutes (T0), 5 minutes (T5), 10 minutes (T10), 15 minutes (T15) and 20 minutes (T20), accompanied by an image taken with differential interference contrast at T0. PC-12 cells were labeled with either AuNF-Chol or AuNS-Chol NPs at 1 nM concentration and excited with a laser power density of approximately 2.5×10^4 W/cm² (561 nm) or 2.5×10^7 W/cm² (640 nm) every 2 minutes. The potential-sensitive probe DiSBAC2(3) was used to visualize depolarization as enhanced fluorescence. Scale bar, 50 μ m. Panels correspond to cells labeled with (A) AuNF-Chol excited by a 561 nm laser; (B) AuNFChol excited by a 640 nm laser; (C) AuNS-Chol excited by a 561 nm laser; or with (D) AuNS-Chol excited by a 640 nm laser.

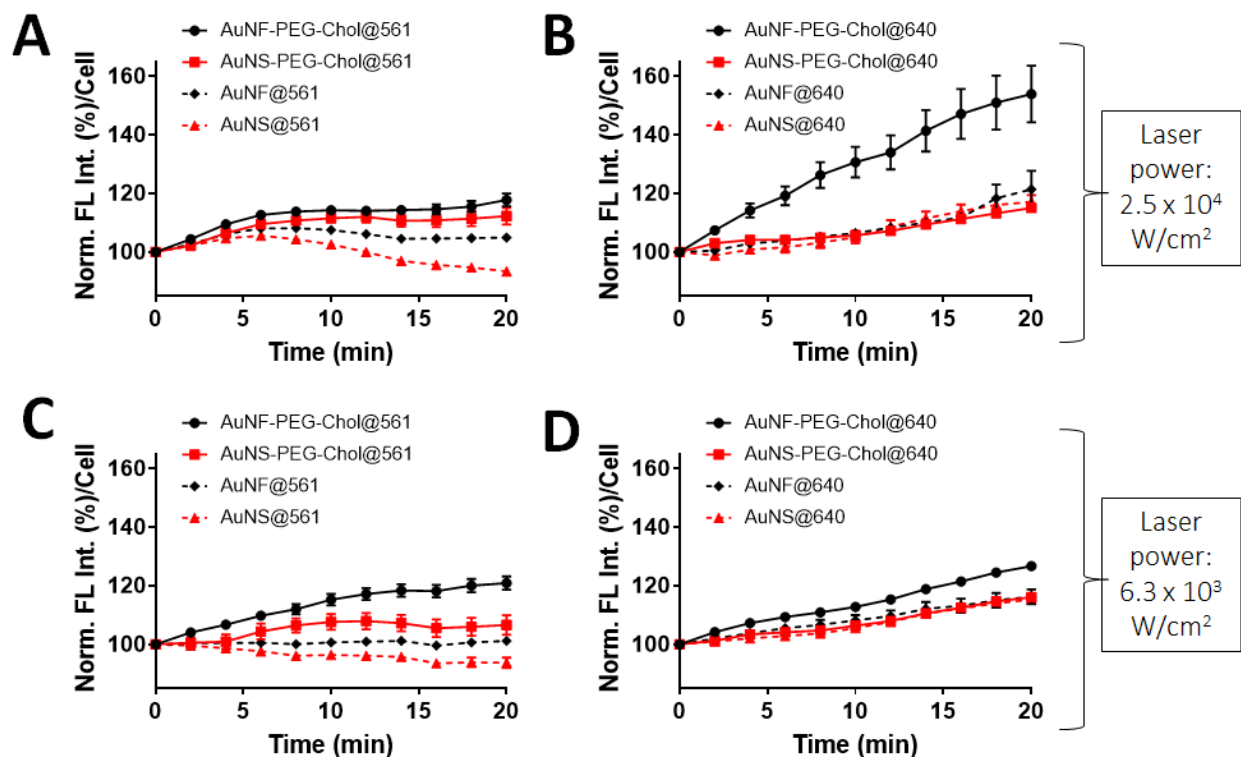


Figure 7. Membrane depolarization of PC-12 cells labeled with 1 nM AuNPs and excited using a 561 nm or a 640 nm laser at various power densities. Membrane depolarization was visualized every 2 minutes for 20 minutes with the potentiometric dye, DiSBAC2(3). The data show the fluorescence intensity per cell over time relative to the initial cell fluorescence at time 0 min (100%). The panels correspond to cells excited with (A) 561 nm laser, 2.5×10^4 W/cm² (B) 640 nm laser, 2.5×10^4 W/cm², AuNF-PEG-Chol@640 values found to be significantly different compared to all other values measured at time points ≥ 2 minutes ($p < 0.01$); (C) 561 nm laser, 6.3×10^3 W/cm², AuNF-PEG-Chol@561 values found to be significantly different compared to all other values measured at time points ≥ 12 minutes ($p < 0.01$); (D) 640 nm laser, 6.3×10^3 W/cm², AuNF-PEG-Chol@640 values found to be significantly different compared to all other values measured at time points ≥ 6 minutes ($p < 0.01$). All statistical analysis was performed using a one-way ANOVA using 30 ± 5 cells.

We next examined the efficiency of depolarization mediated by the AuNP-PEG-Chol conjugates when the cellular labeling was performed with conjugates that had been adjusted to equal optical density (O.D. = 0.52) at the excitation wavelength of 561 nm (Figure 8). When stimulated at 561 nm at a laser power of 2.5×10^4 W/cm², AuNF-PEG-Chol and AuNS-PEG-Chol mediated membrane depolarization with comparable efficiency (Figure 8A). When excited at 640

nm at this same laser power, AuNF-PEG-Chol demonstrated higher signal response (~30% over the 20 min time course) compared to AuNS-PEG-Chol (Figure 8B). At a lower laser power ($6.3 \times 10^3 \text{ W/cm}^2$), the data sets were clean with less photobleaching. PC-12 cells labeled with AuNF-PEG-Chol showed the greatest amount of depolarization, despite the AuNPs having been adjusted to equal absorbance at 561 nm (Figure 8C). We postulate this may be due to the “branched”, pod-bearing anisotropic shape of the AuNF which presents a greater surface area and elongated surface features compared to AuNS. This could result in the AuNFs being appended in closer contact to or greater overall surface contact with the plasma membrane resulting in more efficient heat transfer from the AuNF surface. Previous research has shown that shape affects NP-membrane binding and uptake. A study by Tree-Udom *et al.* demonstrated that elongated spherical NPs had increased cellular uptake in human cells versus spherical NPs or hexagonal particles.⁸⁵ Additionally, computer modeling and experimental research performed by Choo *et al.* demonstrated that nanostar-shaped particles showed advantages over nanospheres when attaching to a specific binding site; the authors suggested that a branched structure provides multiple potential areas of membrane or ligand contact, increasing binding affinity and/or avidity.⁸⁶ These studies support our hypothesis that AuNFs have distinct advantages over AuNS due to their anisotropic shape and protruded pods.

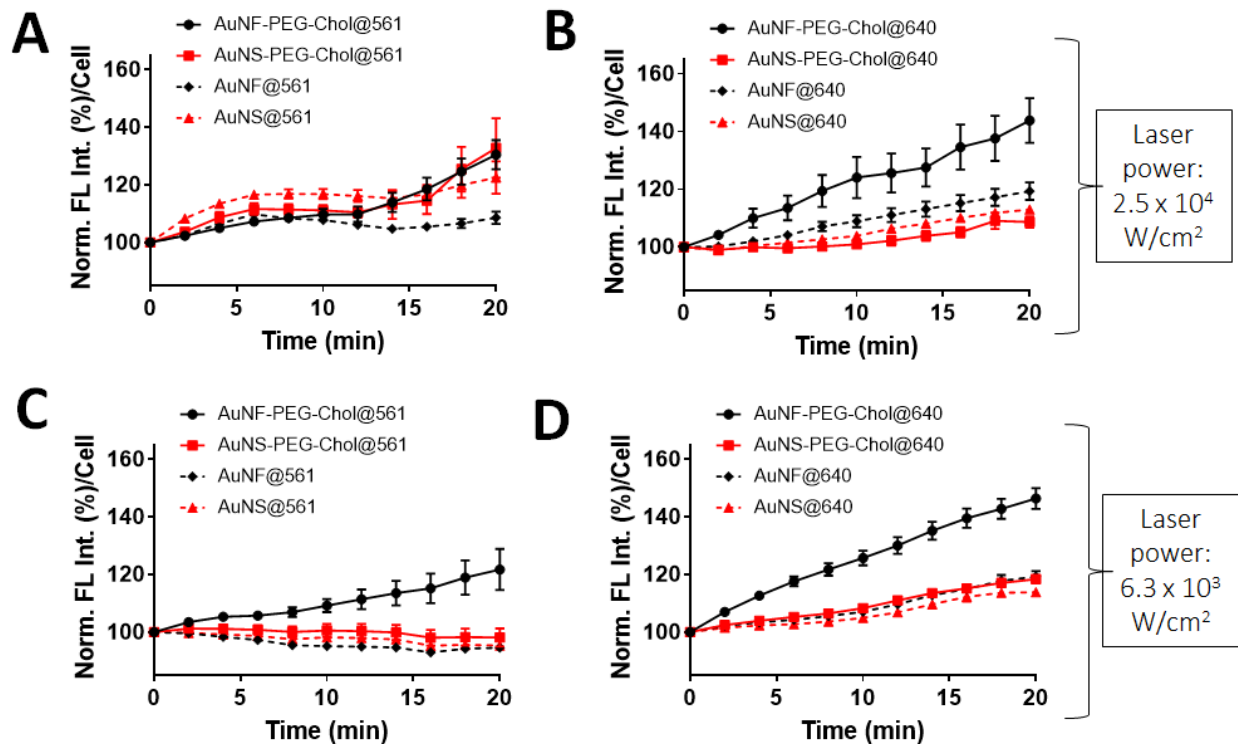


Figure 8. Membrane depolarization of PC-12 cells labeled with AuNPs adjusted to the same optical density (OD = 0.52) at 561 nm. PC-12 cells were labeled with AuNPs at different concentrations and subsequently photoexcited using a 561 nm or 640 nm laser. Cell depolarization was tracked and quantified as described in Figure 7. The panels correspond to cells excited with (A) 561 nm laser, 2.5×10^4 W/cm²; (B) 640 nm laser, 2.5×10^4 W/cm², AuNF-PEG-Chol@640 values found to be significantly different compared to all other values measured at time points ≥ 6 minutes ($p < 0.01$); (C) 561 nm laser, 6.3×10^3 W/cm², AuNF-PEG-Chol@561 values found to be significantly different compared to all other values measured at time points ≥ 2 minutes ($p < 0.01$); (D) 640 nm laser, 6.3×10^3 W/cm², AuNF-PEG-Chol@640 values found to be significantly different compared to all other values measured at time points ≥ 2 minutes ($p < 0.01$). All statistical analysis were performed using a one-way ANOVA using 35 ± 5 cells.

Effect of AuNP-PEG-Chol-mediated membrane depolarization on cellular viability.

The effect of the photoexcited membrane-bound AuNS-PEG-Chol and AuNF-PEG-Chol conjugates on cellular health and viability during depolarization was assessed by live-dead cell staining using calcein-AM and ethidium homodimer-1. PC-12 cells were incubated with AuNS-PEG-Chol, AuNF-PEG-Chol, AuNF and AuNS at 1 nM AuNP concentration. AuNP-labeled cells were photoexcited at $\sim 2.5 \times 10^4$ W/cm², using conditions that replicated the membrane depolarization experiments, with 561 nm or 640 nm laser over a 20 min excitation period. Neither

the process of labeling nor membrane depolarization showed any significant impact on cellular viability with the cells exhibiting >95% viability for cells labeled with the AuNP-PEG-Chol conjugates or the non-Chol AuNPs (Figure 9A,B). These data demonstrate that neither the AuNP materials themselves nor the photoexcitation used for depolarization negatively impacted cell viability. These results agree well with our previously published studies and they further show the excellent biocompatibility of the new AuNF materials.^{57,77} This observed lack of cytotoxicity or phototoxicity is essential for the continued development of AuNFs as a promising material for cellular membrane potential modulation in biological systems.

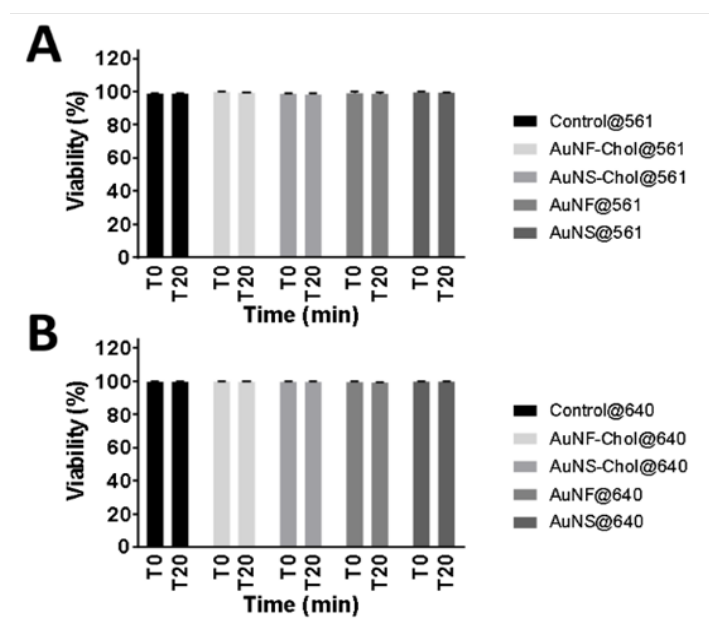


Figure 9. PC-12 cellular viability under AuNP-mediated membrane depolarization. Cells were labeled with 1 nM AuNPs and cellular cytotoxicity was determined using a live/dead cell staining (calcein-AM/ethidium homodimer-1). After incubation with AuNPs, cells were subjected to laser excitation every 2 minutes for 20 minutes. Images of live/dead stain were taken at 0 minutes and at 20 minutes and viability determined by quantifying live and dead cells. Viability is expressed as the percentage of live cells in the total cell population. Neither the AuNP-labeling nor the laser excitation resulted in significant cell death ($p < 0.05$). **(A)** Cellular viability of PC-12 cells excited by 561 nm laser at 2.6×10^4 W/cm². **(B)** Cellular viability of PC-12 cells excited by a 640 nm laser at 2.6×10^4 W/cm². Two-way ANOVA analysis demonstrated no statistical differences between each of the different groups at time T0 or T20 min. The data at each time point correspond to the average viability \pm S.D. from at least 200 cells.

Conclusion

The use of NPs for the controlled modulation of cellular processes and behavior continues to be an area of rich experimental exploration. To date, studies have demonstrated the utility of NP bioconjugates in a range of applications including cell movement, protein expression, drug delivery, and imaging.⁸⁷⁻⁹⁰ The utilization of the plasmonic properties of AuNPs of various geometries has led to photothermal therapy of cancers that are now in multiple clinical trials.⁹¹ With this has emerged the use of AuNPs for the controlled optical modulation of cellular membrane potential and this is now a rapidly-growing area of research. Several studies have now confirmed both the optocapacitive and distance-dependent nature of photothermal opening of ion channels for neuronal stimulation/activation.^{54,77} Much of this work has focused on spherical AuNPs with absorption in the visible part of the spectrum. One desired goal is the development of AuNPs with efficient absorption in the NIR so as to enable neuronal photostimulation with lower power and deeper penetrating light.

To that end, our goal in this study was to employ a new 'seedless' AuNP synthesis strategy to realize AuNFs with far red-shifted absorption that spans beyond 800 nm. This variation of NP is advantageous due to the fact it can absorb light at near infra-red wavelengths, which is less phototoxic to cells and has improved tissue penetration *in vivo* in comparison to shorter wavelengths.^{81,92,93} During synthesis of our novel AuNF, we demonstrate the ability to control the size diameter of the particles to $20 \text{ nm} \pm 2 \text{ nm}$, with excellent colloidal stability. AuNF possessed a broader region of absorbance with a peak at 618 nm compared to the sharper peak of AuNS at 520 nm, a characteristic that was sustained post-conjugation with PEG-Chol and PEG-FITC. After

initial synthesis, both AuNF and AuNS were amenable to bioconjugation with PEG-Chol and PEG-FITC via EDC-NHS chemistry. PEG-Chol was attached in order to facilitate closer localization with the plasma membrane of PC-12 cells in order to improve cellular depolarization, while PEG-FITC was used for visual tracking.⁵⁷ We found that the Chol moiety was instrumental in mediating close membrane localization, as demonstrated previously.⁵⁷ As expected from the observed absorbance spectra, AuNF facilitated more efficient photothermally-initiated depolarization at 640 nm as compared to AuNS, with a 50% increase in depolarization efficiency at $2.5 \times 10^4 \text{ W/cm}^2$. Interestingly, for both cases where AuNPs were applied to cells in equal concentration and fixed OD at 561 nm, higher levels of depolarization were observed in AuNF-treated cells during stimulation with the 561 nm laser. We hypothesize this is due to a positive effect exerted by the branched pods on the surface of the AuNF on affinity to the cell, supported by former observations of increased binding affinity in nanostars over nanospheres.⁸⁶ Finally, PC-12 cells undergoing AuNF-PEG-Chol- and AuNS-PEG-Chol-mediated depolarization suffered no notable reduction in viability after incubation with NPs or after photothermally-activated depolarization.

The work presented herein expands upon previous work within our group in the effort to develop AuNPs for modulated control of cellular depolarization via the opening of voltage-gated sodium channels and induced depolarization of membrane potential.^{54,57,77} In addition, we build upon other studies that have examined the use of laser irradiation of other types of NPs such as gold nanospheres or gold nanorods as a method to control neuronal stimulation.⁹² AuNFs provide benefits over other types of unique gold NP shapes given their colloidal stability, which is a challenge to do while avoiding cytotoxicity in other anisotropic AuNPs such as nanorods.^{93,94} Most importantly, for use in therapeutic applications, the AuNFs have a peak shifted toward NIR

wavelengths, which is extremely beneficial for use in an in vivo setting. Ideally, to be used in vivo, the AuNP-mediated plasma membrane depolarization system should preferentially absorb light in the NIR and IR spectra “tissue optical transparency” window, which allows for deeper light penetration to 1 mm and carries lower phototoxicity.^{95,96} Investigations from other groups have also illustrated some success using gold nanorods to depolarize cells in the IR range. Gold nanorods injected into the sciatic nerve of Sprague Dawley rats were pulsed with a 980 nm laser (power approximately 0.01 kW cm^{-2}) which induced an ~6-fold increase in action potentials versus the uninjected group, while also avoiding significant neural damage.⁹⁷ This in vivo work is an extremely promising indication that AuNPs excited in the IR range are suitable for therapeutic modulation of membrane potential. We expect that our AuNF materials will find great utility in the in vivo modulation of cellular membrane potential.

Chapter 4: Multivalent Display of Erythropoietin on Quantum Dots Enhances Aquaporin-4 Expression and Water Transport in Human Astrocytes *In Vitro*

Introduction

The development of a fundamental understanding of cellular processes and how to control them in a spatiotemporal manner continues to be a major goal of biotechnology. Within this pursuit, biofunctionalized nanomaterials are playing a significant role as new NP-biological hybrids for the control of cellular physiology continue to emerge at a steady pace.^{98,99} The implementation of increasingly sophisticated multifunctional NP bioconjugates now includes composite materials for advanced imaging and sensing¹⁰⁰, drug delivery²⁹, and the actuation of cellular physiology (*e.g.*, membrane potential).⁷¹ One area that has received considerable attention is the use of NPs for the regulated control of gene expression. To date, this has typically been achieved through the cellular delivery of NP-plasmid or NP-mRNA constructs.^{101,102} One theme that remains largely underexplored is the control of intracellular signaling/gene expression *via* the interfacing of NP-growth factor bioconjugates with cell surface signaling receptors. For example, Vu *et al.* conjugated nerve growth factor to the surface of semiconductor QDs to bind to and activate tyrosine kinase A (TrkA) receptors and invoke intracellular signaling and differentiation.⁶⁷ The Nakanishi group recently showed the use of epidermal growth factor (EGF)-functionalized gold NPs to mediate clustering of EGF receptors and activation of downstream kinase activity and regulation of apoptosis.¹⁰³ Despite these examples, much remains to be learned regarding the use of NP-growth factor conjugates as value-added materials for the induction of cellular signaling.

The glymphatic system (GS) is a recently discovered macroscopic fluid pumping system in the brain that is responsible for both the elimination of wastes and the distribution of critical nutrients (*e.g.*, glucose, amino acids, growth factors).¹⁰⁴ Discovered only recently in 2012, this

system has been characterized as a brain-wide perivascular transit network between cerebrospinal fluid (CSF) and interstitial solutes comprised of a CSF influx pathway and a perivenous efflux pathway.¹⁰⁵ It has now become well-established that this convective flushing/transport system functions nearly exclusively during late stage, non-rapid eye movement sleep and it is disengaged during wakefulness.¹⁰⁶⁻¹⁰⁸ Thus, the GS not only plays a critical role in restful sleep and cognition but impaired GS function has also been linked to a number of neurodegenerative diseases, including Alzheimer's disease.¹⁰⁶ The transport of fluid and solutes is facilitated by the water-conducting activity of AQP4 membrane channels expressed in polarized fashion on the endfeet of human astrocytes (HA). Given this critical role of AQP4 membrane channels in the GS, there is considerable interest in the controlled modulation of AQP4 expression and water transport activity. However, the number of available therapeutics with which to achieve this remains limited.

The work of Brissaud *et al.* established the role of the cytokine EPO in the induction of AQP4 expression in an *in vivo* rat model of hypoxic ischemia¹⁰⁹ and Siddiqui *et al.* showed the neuroprotective effect of EPO-induced increased AQP4 expression in the treatment of hydrocephalus.¹¹⁰ The binding of EPO to the EPO receptor (EPOR) induces receptor dimerization and the activation of the Janus kinase/signal transducer and activator of transcription (JAK/STAT) signaling pathway.^{111,112} In HA, this signaling results in the synthesis and localization of AQP4 channel proteins to the plasma membrane. Further, it has been shown that EPOR signaling is membrane raft-dependent, where the clustering of EPOR and the formation of membrane raft microdomains is essential for EPO-induced signaling *via* the EPOR.¹¹³ Taking this as motivation, our working hypothesis in the present study was that the multivalent display of EPO on the surface of QDs (EPO-QD) would facilitate the simultaneous ligation and clustering of multiple EPOR, resulting in augmented EPOR-mediated signaling compared to free, monomeric EPO. QDs are an

ideal NP platform for this approach as their small size and comparatively large surface area enable the display of multiple copies of EPO to interact with EPOR. Further, their bright, photostable luminescence enables the time-resolved tracking and imaging of the EPO-QD conjugates using confocal microscopy. Lastly, the QDs used here are capped with small zwitterionic ligands that render them highly colloiddally stable and biocompatible and enable the facile assembly of EPO to their surface (*vide infra*).^{114,115}

Herein our approach was to self-assemble recombinant human EPO bearing a C-terminal polyhistidine domain (EPO-his) to the surface of CdSe-CdS/ZnS core-shell QDs (~5 nm diameter) where the histidine tract binds to the ZnS shell through metal affinity coordination. We have used this assembly strategy in a multitude of configurations for the generation of stable QD-peptide and QD-protein bioconjugates for cellular applications.¹¹⁶⁻¹²⁰ Here we show that EPO-his self-assembles to the QD surface in a ratiometric manner and that the bioconjugates bind specifically to EPOR-expressing HA cells. Incubation of EPO-QD with HA for 24 h results in a 1.8-fold greater induction of AQP4 expression compared to free EPO at the same concentration. This is coupled with the augmented activation of the JAK/STAT signaling pathway as confirmed by ELISA.¹²¹ The increased AQP4 expression is coupled with a 2-fold increase in water efflux from HA as determined by a calcein AM water transport quenching assay. We discuss our results in the context of their implications on our furthered understanding of the GS and the potential control of the GS through the rational design of functional nanomaterials. More generally, our results demonstrate the utility of NP-growth factor bioconjugates for the controlled modulation of gene expression/protein synthesis.

Materials and Methods

Chemicals. Cadmium acetylacetonate (98%), tri-*n*-octylphosphine (TOP; min. 97%), selenium (Se; 99.99%), dimethylcadmium (CdMe₂; 99.995+%) and diethylzinc (ZnEt₂; min. 95%) were purchased from Strem Chemicals. Hexadecylamine (HDA; technical grade, 90%), trioctylphosphine oxide (TOPO; technical grade, 90%), oleylamine (technical grade, 70%), hexamethyldisilathiane ((TMS)₂S) were purchased from Sigma Aldrich. 1-Dodecylphosphonic acid (DPA; 95%) was purchased from Alfa Aesar. Diisooctylphosphinic acid (technical grade, 90%) was purchased from Fluka. Human erythropoietin, mouse anti-EPOR monoclonal antibody, mouse anti-AQP4 monoclonal antibody, and 4',6-diamidino-2-phenylindole (DAPI) were purchased from Sigma. Normal goat serum and goat anti-mouse tetramethylrhodamine (TRITC) conjugate were obtained from Jackson ImmunoResearch. LCIS and DPBS were purchased from ThermoFisher Scientific. Recombinant EPO bearing a C-terminal 6-histidine tract (EPO-his, ~20 kDa) was purchased from Novus Biologicals.

CdSe core synthesis. Se (0.33 g, 4.2 mmol) was mixed with 5.0 mL of TOP in a 20 mL vial, which was sealed with a septum. The mixture was degassed under vacuum at 80 °C for 10 min, filled with N₂, and stirred until Se was dissolved. Cadmium acetylacetonate (0.310 g, 1.0 mmol), 1-dodecylphosphonic acid (0.250 g, 1.0 mmol), diisooctylphosphinic acid (0.35 mL, 1.1 mmol), TOP (14 mL), and HDA (5.0 g) were loaded into a 50 mL three-neck round-bottom flask. The reaction mixture was degassed under vacuum at 100 °C for 30 min. After backfilling with N₂, the reaction mixture was heated to 300 °C with a heating mantle to dissolve the cadmium precursor. The heating mantle was removed, and the TOP:Se solution was swiftly injected at 300 °C with vigorous stirring. Then the reaction mixture was quickly cooled below 180 °C by blowing air. After cooling to 60 °C, *n*-butanol (10 mL) was added to prevent solidification of the reaction mixture. The reaction mixture was aliquoted to 40 mL vials. Excess acetone was added to each vial to flocculate

the QDs. The mixtures were centrifuged at 3,800 rpm for 5 min. The supernatant was discarded, and the QD pellets were dissolved in a minimum amount of toluene. This cleaning procedure was repeated one more time. The final CdSe QD concentration was estimated following the literature method.¹²²

Overcoating of CdSe core QDs with CdS/ZnS shell. TOPO (18.0 g), oleylamine (5.0 mL), TOP (5.0 mL) and the CdSe QD core (1.0 μmol in toluene solution) were loaded into a 100-mL three-neck round-bottom flask. The reaction mixture was degassed under vacuum at 100 °C to remove toluene and other volatiles, and backfilled with N₂. The amount of shell precursors used for the overcoating was calculated following the literature procedure.¹²³ For the coating of half monolayer of CdS, a mixture of CdMe₂ and (TMS)₂S in TOP was added dropwise starting at 130 °C. During the CdS precursor addition, the reaction mixture was heated to 140 °C. Subsequently a mixture of ZnEt₂ and (TMS)₂S in TOP was added dropwise, and the reaction mixture was heated from 140 to 175 °C during the ZnS precursor addition. The reaction mixture was subsequently annealed at 190 °C for 4 h at 80 °C overnight.

Ligand exchange of CdSe/CdS/ZnS QDs. Hydrophobic CdSe/CdS/ZnS QDs were transferred to water *via* ligand exchange with Compact Ligand 4 (CL4) ligands using previously published methods.¹¹⁵ CL4 ligands were chosen due to their two terminal COOH groups providing colloidal stability to the QDs. The final CL4 QDs were found to have an emission wavelength centered at 540 nm.

EPO-his assembly to QDs. EPO-his was self-assembled to the surface of QDs *via* metal affinity coordination between the polyhistidine tract and Zn atoms in the ZnS shell. QDs at a fixed concentration were incubated with EPO-his at various EPO-his:QD ratios for 1 h at room

temperature. In some instances, assemblies were allowed to form overnight at 4 °C prior to use. Bioconjugate formation was confirmed by gel electrophoresis, DLS, and zeta potential (*vide infra*). *Gel electrophoresis.* Gel electrophoresis experiments were performed on a 1% agarose gel using TBE (100 mM Tris, 83 mM boric acid, 1 mM EDTA, pH 8.3). EPO-QD assemblies were prepared by mixing QDs (fixed at 10 nM concentration) with varying molar ratios of EPO-his, incubating for 1 h, followed by mixing with a 10% glycerol solution prior to loading into the gel. The gel was run at 8 V/cm for 30 min and imaged using UV light illumination on a Kodak Gel Logic 2200 imaging system.

Zeta potential and DLS. Zeta potential and DLS measurements were carried out using a Malvern ZetaSizer Ultra/Pro (Malvern Instruments Ltd, Worcestershire, UK) and analyzed using Dispersion Technology Software (DTS, Malvern Instruments Ltd, Worcestershire, UK). To characterize zeta potential, QDs were mixed with varying ratios of EPO-his as described above. Samples were prepared in 0.1× DPBS (pH 7.4) and loaded into disposable electrode-bearing cells and data collected at room temperature. The autocorrelation function was the average of five runs of 30 seconds each (repeated three to six times). CONTIN analysis was used to determine the number of QDs in a field of view versus hydrodynamic size for the dispersions studied.

Cell culture. Primary human astrocytes (HA) isolated from human brain (Creative Biolabs, product no. NCC20-9PZ01) were cultured using the supplier's basal medium amended to contain fetal bovine serum, growth factors, and penicillin/streptomycin (CocKit™ Astrocyte Growth Medium Kit, Creative Biolabs). Cultures were maintained in T25 flasks and incubated at 37°C in a 5% CO₂ humidified atmosphere and passaged when 70-80% confluent. All cells in this study were used between passages 2 and 7. For experimental procedures, HA were plated on 35 mm MatTek dishes

(MatTek, #1 coverglass, 14 mm growth surface) at a cell density of 1×10^5 cell/ml (3×10^5 cells/dish).

Characterization of EPO-QD cellular labeling. HA cells were plated onto dishes as described above and incubated with EPO-QDs (at different EPO/QD ratios) for varying lengths of time over a 24 h period to determine the time-resolved nature of the conjugates' binding interaction with and uptake by the cells. After washing with DPBS to remove unbound EPO-QD conjugates, the cells were imaged by confocal microscopy using 488 nm laser excitation. NIS-Elements AR (ver. 4.30.02) software was used to quantify the average QD fluorescence per cell. Individual cells were treated as regions of interest and quantitative analysis was performed on at least 100 cells across multiple experiments.

Induction of AQP4 expression using monomeric EPO or multivalent EPO-QDs. HA were plated to dishes in complete growth media and allowed to attach overnight. The cells were then washed with DPBS and subjected to serum starvation (complete medium components minus fetal bovine serum) for 18 hours. Cell monolayers were then incubated with either EPO or EPO-QDs (at equivalent EPO concentration) for 24 h to induce AQP4 expression. The cells were washed and subjected to immunohistochemical staining to quantify AQP4 expression levels (*vide infra*).

Immunohistochemistry (IHC). We performed antibody staining on HA to confirm expression of EPOR and to quantify the induction EPO- or EPO-QD-induced expression of AQP4. For these experiments, HA were fixed for 30 min with 4% paraformaldehyde diluted in DPBS and subsequently permeabilized with 0.05% Triton X-100/DPBS for 5 minutes. Nonspecific binding sites were blocked with 1% normal goat serum (Jackson ImmunoResearch) in DPBS. HA were then incubated with the primary antibody overnight at 4° C diluted in 0.01% normal goat serum with DPBS. Mouse anti-EPOR monoclonal antibody (10 µg/mL) or mouse anti-AQP4

monoclonal antibody (20 $\mu\text{g}/\text{mL}$) were incubated with the cells overnight at 4 °C followed by washing and incubation with goat anti-mouse IgG-TRITC conjugate (20 $\mu\text{g}/\text{mL}$) for 1 h at room temperature. All antibody incubations were performed in 0.1% normal goat serum in DPBS. Finally, HA were labeled with DAPI (5 $\mu\text{g}/\text{mL}$) to visualize nuclei.

EPO and EPO-QD mediated activation of JAK/STAT signaling pathway. We quantified the activation of the JAK/STAT signaling pathway by using a human phosphotyrosine JAK/STAT ELISA Kit (RayBiotech) according to manufacturer instructions. HA ($\sim 8 \times 10^6$ cells) were treated with free EPO or EPO-QD conjugates and subsequently lysed using the provided lysis buffer. Cell lysates were added to the wells of a 96-well plate that was coated with anti-JAK2 monoclonal antibody and incubated for 2.5 h. After washing, a biotinylated anti-phosphotyrosine antibody was incubated in each well for 1 h. Following washing, a horseradish peroxidase streptavidin conjugate was added and incubated for 45 min. 3,3',3,5'-tetramethylbenzidine (TMB) peroxidase substrate was added and color was allowed to develop for 5 min before adding 1N HCl stop solution. Absorbance was immediately read at 450 nm using a SparkCyto Tecan plate reader.

Characterization of AQP4 water transport activity. Water transport activity mediated by AQP4 channels in HA after treatment with EPO or EPO-QD conjugates was quantified using a calcein AM quenching assay adapted from Kitchen *et al.*¹²⁴ This assay tracks the quenching of calcein AM as cells are induced to efflux water out of the cell under hypertonic conditions. After treatment with EPO or EPO-QDs as described, cells were washed with DPBS and then incubated with calcein AM (8 μM in LCIS) for 45 minutes at 37° C. Cells were washed with DPBS and the extracellular medium was made hypertonic (~ 450 mOsm) by the addition of 0.5M NaCl to the dish at a rate of 50-100 $\mu\text{L}/\text{sec}$. Cell images were acquired approximately every 2 seconds over the course of 180 seconds using the following acquisition settings: 488 nm excitation, 500 ms, 0.19

μm^2 focused spot size, 2.2 $\mu\text{s}/\text{pixel}$, and a total image size 512×512 pixels leading to a physical image size of 0.21 x 0.21 mm. HA were then returned to isotonic conditions by the addition of sterilized water. Image analysis was performed and the fluorescence intensity of each cell at each timepoint was recorded and normalized to the fluorescence value at 0 seconds (starting isotonic conditions). To find the rate of water transport in HA, that part of the raw data corresponding to the beginning and end of changes to calcein AM fluorescence intensity induced by hypertonic conditions (typically $t = 20$ to 30 sec) were isolated from the rest of the data and an exponential decay curve of the form $y = Ce^{(-kt)}$ was fitted to each curve using GraphPad Prism 7.0 software. The rate constant C is equal to y_0 (the initial value of y) at $t = 20$ seconds (amplitude fit parameter for normalized data) and k is proportional to plasma membrane water permeability.

Cellular cytotoxicity of EPO-QDs. HA were incubated with varying concentrations of free EPO or EPO-QDs for up to 48 h. The cells were washed with LCIS and stained with a live/dead cell viability assay kit (ThermoFisher). Calcein AM (0.4 μM) and ethidium homodimer (0.2 μM) were dissolved in LCIS and incubated with cells for 30 min at 37°C. Fluorescence imaging to capture calcein AM and ethidium homodimer signal was performed with 488 nm and 561 nm excitation, respectively. Cell viability was determined by counting the number of calcein- (live) or ethidium homodimer (dead)-positive cells (at least 450 cells counted for each treatment condition). Viability was reported as the percentage of live cells compared to the total cell count.

Microscopy and Image Analysis. All imaging was performed using a Nikon A1RSi laser scanning confocal imaging system. The following imaging settings were used (laser excitation/dichroic/emission range): QDs and calcein, 488 nm/510 nm/500-550 nm; TRITC and ethidium homodimer, 561 nm/595 nm/570-620 nm. Each channel was imaged sequentially to

prevent bleed-through between the channels. Image analysis and image preparation was done using NIS-Elements AR (ver. 4.30.02).

Statistical Analysis. Univariate analysis of variance (ANOVA) was performed using GraphPad Prism 7.0 software for Windows.

Results and Discussion

Our goal in this study was to realize a multivalent EPO-NP system capable of mediating the augmented stimulation of EPOR signaling in HA cells, resulting in the increased expression of AQP4 and enhanced water transport. To accomplish this we chose QDs as a prototypical NP scaffold not only for their superior brightness and photostability (for imaging) but also for their amenability to stable bioconjugate formation *via* metal affinity coordination self-assembly of peptides and proteins bearing polyhistidine domains.¹²⁵ Figure 10A depicts schematically the self-assembly of EPO bearing a C-terminal six-histidine tract (EPO-his) to the surface of CdSe-CdS/ZnS core-shell QDs. These QDs (~5 nm in diameter) exhibit excellent crystallinity as shown by TEM with emission centered at 540 nm (Figure 11, Figure 12).

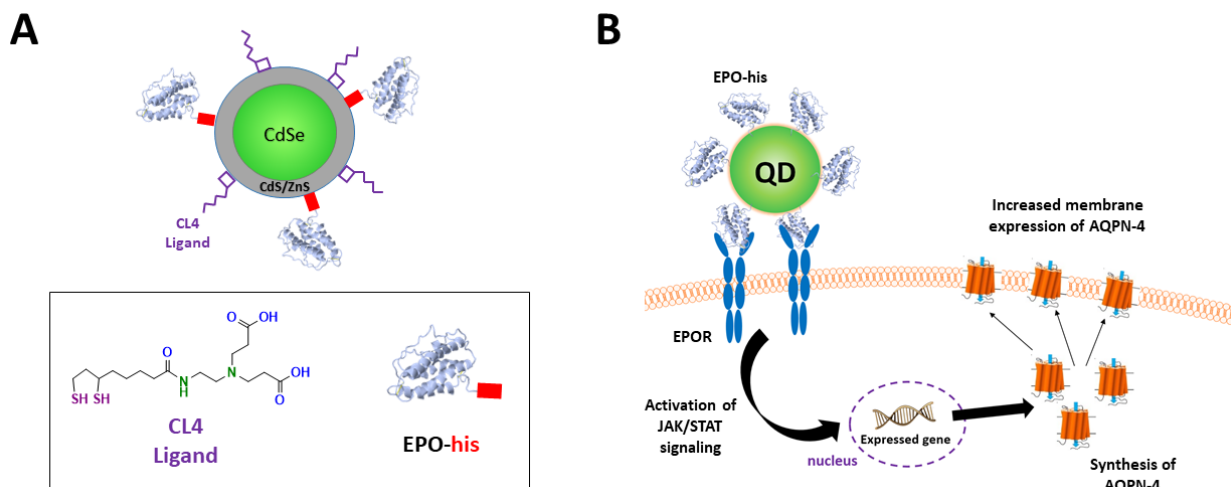


Figure 10. EPO-QD bioconjugate system. (A) The bioconjugate system is comprised of CdSe-CdS/ZnS core-shell QDs capped with the zwitterionic ligand, CL4. Erythropoietin (EPO) bearing a C-terminal polyhistidine domain (EPO-his, in red) is assembled to the QD surface *via* metal affinity interaction between the his domain and ZnS shell. (B) The multivalent display of EPO-his enables ligation of multiple EPO receptors (EPOR) for enhanced activation of the JAK/STAT signaling pathway resulting in the augmented synthesis and localization of AQPN-4 to the plasma membrane. Note: figure is not to scale.

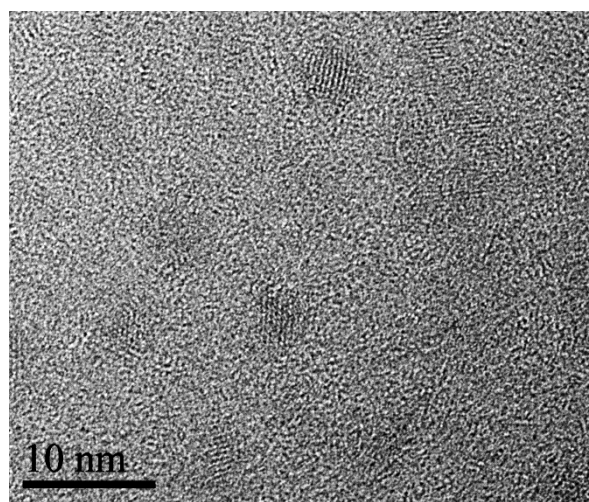


Figure 11. Transmission electron microscopy (TEM) of QDs used in this study. Shown is a TEM image of the 540 nm-emitting QDs (capped with CL4 ligands) used herein. The QDs are 4.7 ± 0.5 nm in diameter.

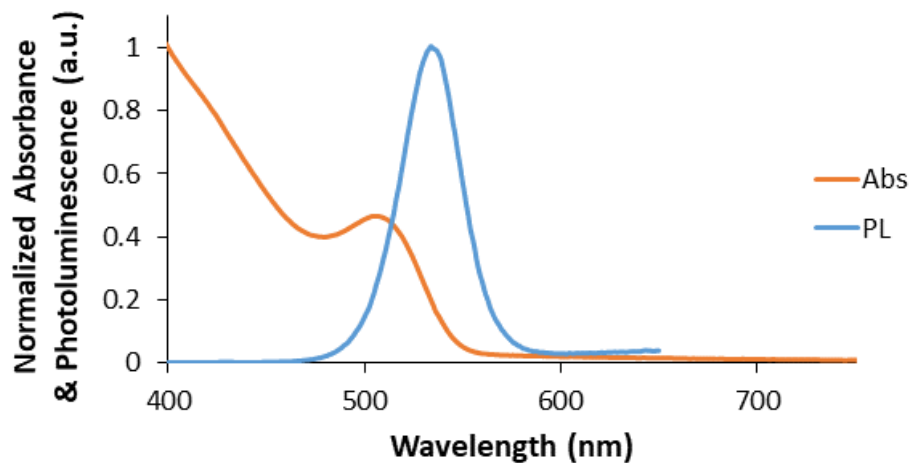
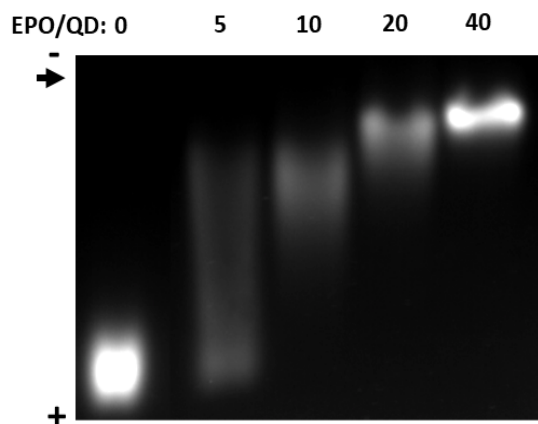


Figure 12. Absorption and emission spectra of QDs. Shown is the normalized absorption (Abs, orange) and photoluminescence (PL, blue) spectra of the QDs used in this study. The QD emission is centered at 540 nm.

The zwitterionic capping ligand, CL4, affords excellent water solubility and its short extended length (~1.8 nm) enables the robust and stable assembly of his-tagged proteins to the QD surface. Indeed, we have shown in numerous studies the long-term intracellular stability and biocompatibility of QD bioconjugates capped with this and similar ligands.^{114,115,126} Thus we had great confidence in our ability to create functional EPO-QD conjugates capable of simultaneously ligating multiple EPOR to stimulate AQP4 expression *via* the JAK/STAT intracellular signaling pathway (Figure 10B).

Characterization of EPO-QD bioconjugates. We first confirmed the assembly of EPO-his to the QD surface by gel electrophoresis, DLS, and zeta potential measurements. Figure 13A shows that when assembled with increasing ratios of EPO-his, the gel migration of the negatively-charged

A**B**

| Sample ¹ | EPO/QD | D_h (nm) ² | Zeta Potential (mV) |
|---------------------|--------|-------------------------|---------------------|
| 10 nM QD only | -- | 12.0 ± 0.5 | -30.2 ± 0.4 |
| 20 nM EPO-QD | 2 | 13.0 ± 0.5 | -23.6 ± 1.5 |
| 50 nM EPO-QD | 5 | 14.3 ± 0.9 | -18.6 ± 0.6 |
| 100 nM EPO-QD | 10 | 14.7 ± 1.1 | -13.2 ± 1.6 |
| 200 nM EPO-QD | 20 | 18.2 ± 0.6 | -13.7 ± 0.9 |
| 400 nM EPO-QD | 40 | 19.9 ± 0.5 | -5.2 ± 0.5 |

¹[QD] was 10 nM in all cases

²Hydrodynamic diameter (D_h) as measured by dynamic light scattering

Figure 13. Physical characterization of EPO-QD bioconjugates. (A) Gel electrophoresis analysis of QDs and EPO-QD conjugates. The EPO/QD ratio is shown as is the negative (cathode) and positive (anode) electrodes. The arrow indicates the location of the sample loading wells. (B) DLS (for determination of D_h) and zeta potential (surface charge) analysis for QDs and EPO-QD conjugates.

QDs towards the anode (positive post) is slowed. This is consistent with both the shielding of the negative CL4 ligands at the QD surface and the formation of larger conjugates when QDs are assembled with increasing ratios of EPO-his. Based on the gel migration, a ratio of 20 EPO-his per QD resulted in maximum QD surface loading as addition of EPO-his beyond this ratio did not retard QD movement any further. This is consistent with our previous work showing that for proteins on the size order of EPO-his (approximately 30 kDa), maximal packing on a 5 nm diameter QD is ~20 proteins.¹²⁷ DLS analysis and zeta potential showed a consistent increase in hydrodynamic diameter (D_h) and a decrease in overall negative QD surface charge with increasing addition of EPO-his, respectively (Figure 13B). Cumulatively, these results confirm the controlled, ratiometric assembly of EPO-his to the QD surface.

Characterization of EPO-QD binding to EPOR on HA. We next determined the efficiency of binding and uptake of the EPO-QD conjugates to the EPOR on HA. First, we confirmed by IHC the expression of EPOR in HA cell monolayers (Figure 14).

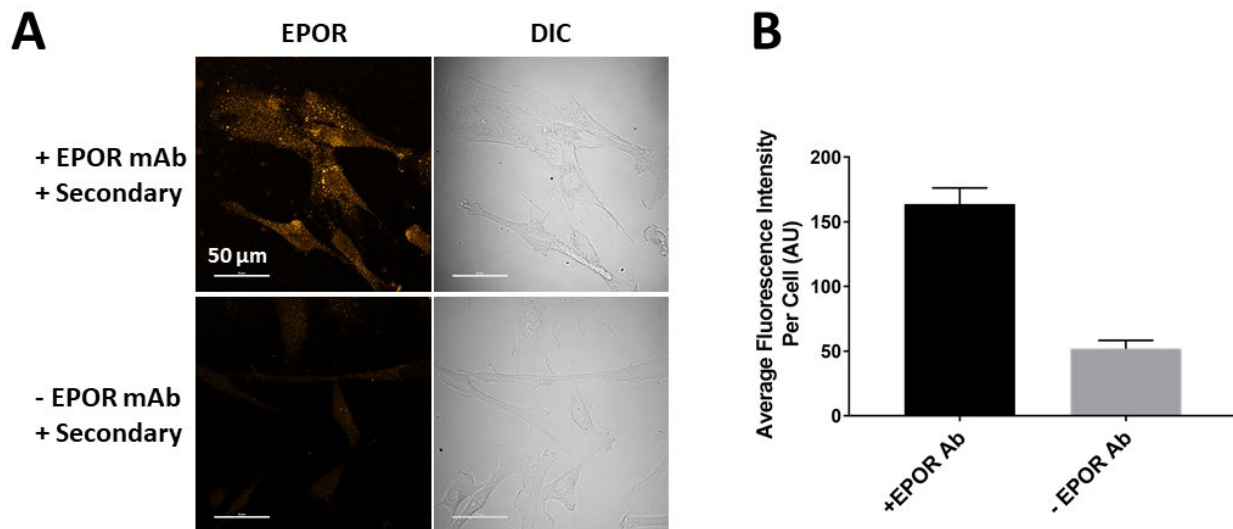


Figure 14. Immunohistochemistry (IHC) for visualization of EPOR expression in HA. (A) IHC was performed on fixed, permeabilized HA (see Methods for details) to confirm expression of EPOR. Cells were incubated overnight at 4 °C with mouse anti-EPOR monoclonal antibody (mAb, 10 $\mu\text{g}/\text{mL}$) when present and 1 h at room temperature with goat anti-mouse IgG-TRITC conjugate (secondary, 20 $\mu\text{g}/\text{mL}$). Antibodies were diluted in 0.01% normal goat serum/D-PBS. Cells were also stained with DAPI (5 $\mu\text{g}/\text{mL}$). (B) Quantification of the cellular fluorescence staining of the image in (A) showing the specificity of the anti-EPOR mAb for the EPOR in HA. The quantification is representative of three independent experiments.

Shown in Figure 15A are the resulting fluorescence micrographs when HA were incubated for 24 h with 10 nM QDs assembled with increasing amounts of EPO-his (20, 50, and 100 nM corresponding to EPO/QD ratios of 2, 5, and 10, respectively). We chose this 24 h incubation time window to avail adequate time for AQP4 protein synthesis and translocation to the plasma membrane. Results from our previous work demonstrating the long-term intracellular stability of QD conjugates generated through histidine-based assembly gave us great confidence in the integrity of the EPO-QD conjugates over this time frame.¹²⁶ Interestingly, quantification of this data revealed that maximal cellular labeling occurred at a ratio of 5 EPO/QD (Figure 15B). When

the ratio was increased to 10 EPO/QD there was no significant increase in cellular labeling, suggesting maximal interaction of EPO-QD with the EPOR at the former ratio. This is consistent with the generally accepted nature of the interaction of NPs with cells wherein both NP size, surface curvature and surface protein density critically determine the efficacy of cellular binding of NP-bioconjugates.¹²⁸ Time-resolved imaging over a 24 h time period where HA were incubated with 10 nM QD (5 EPO/QD) showed a steady increase in the amount of cellular QD labeling (Figure 15C and 16). Further, the EPO-QD conjugates were largely colocalized with an AlexaFluor546-transferrin endocytosis marker (Figure 17). This is consistent with the known EPO-induced endocytosis of EPOR which is regulated by JAK activity.¹²⁹ Control, competition binding experiments where cells were co-incubated with a 50 nM EPO/10 nM QD and a five-fold molar excess of free EPO showed significant inhibition of EPO-QD binding to HA cells, demonstrating the specificity of interaction of EPO-QD with the EPOR (Figure 18).

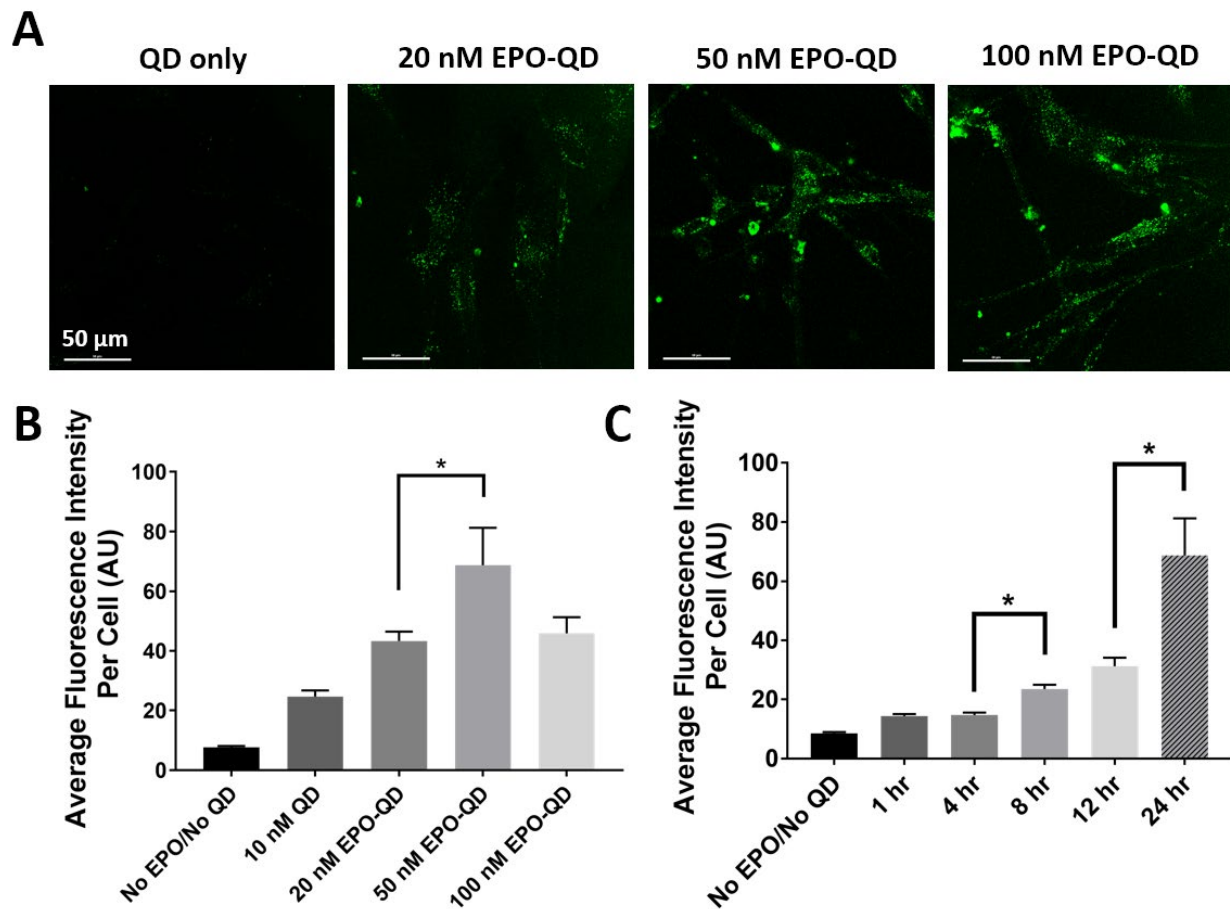


Figure 15. Quantification of the binding of EPO-QD to EPOR on HA. (A) Micrographs showing the resulting fluorescence when 10 nM QDs alone or 10 nM QDs assembled with the EPO concentrations indicated were incubated with HA for 24 h followed by washing and imaging. 20, 50, and 100 nM EPO correspond to EPO/QD ratios of 2, 5, and 10, respectively. (B) The quantification of fluorescence images shows the increase in fluorescence signal of the membrane-bound QDs that reaches a maximum at a ratio of 5 EPO/QD. There is no statistical significance between 5 and 10 EPO/QD. (C) Time-resolved quantification of EPO-QD (at 5 EPO/QD) binding to astrocytes. The EPO-QD conjugates were incubated on the cells for the times indicated. Cell images corresponding to panel C are shown in Figure 16. In panels B and C, the data correspond to analysis of at least 100 cells across two independent experiments and * indicates $p < 0.01$.

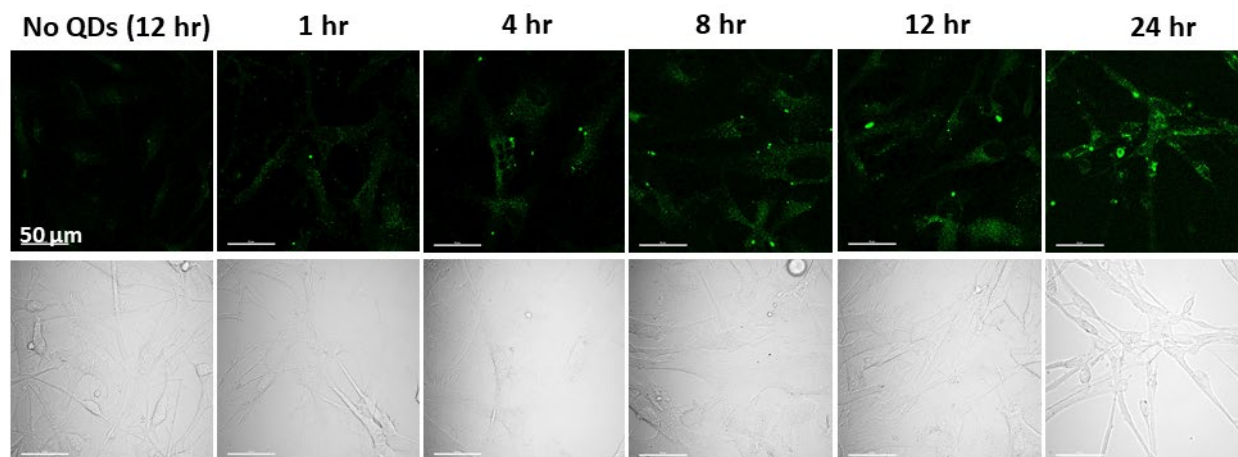


Figure 16. Time-resolved labeling of HA with EPO-QD conjugates. HA cell monolayers were incubated with 50 nM EPO/10 nM QD (5 EPO/QD) or 10 nM QDs alone for the times indicated and the imaged for QD fluorescence.

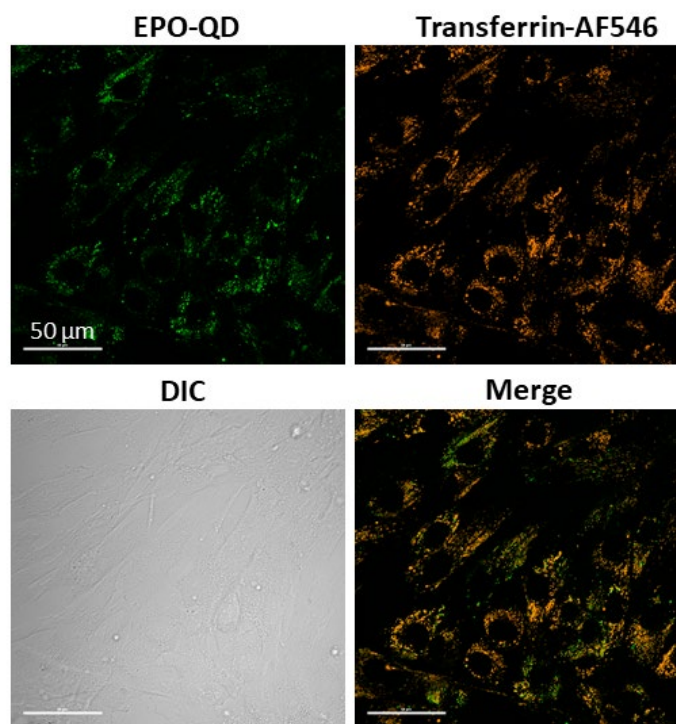


Figure 17. Colocalization of EPO-QD with transferrin endocytosis marker. HA cell monolayers were incubated with 50 nM EPO/10 nM QD (5 EPO/QD) for 12 hr and colabeled with an AlexaFluor546-transferrin conjugate to assess localization of EPO-QD within the endocytic pathway. Pearson's colocalization coefficient for green QDs localized with red transferrin marker was 0.55.

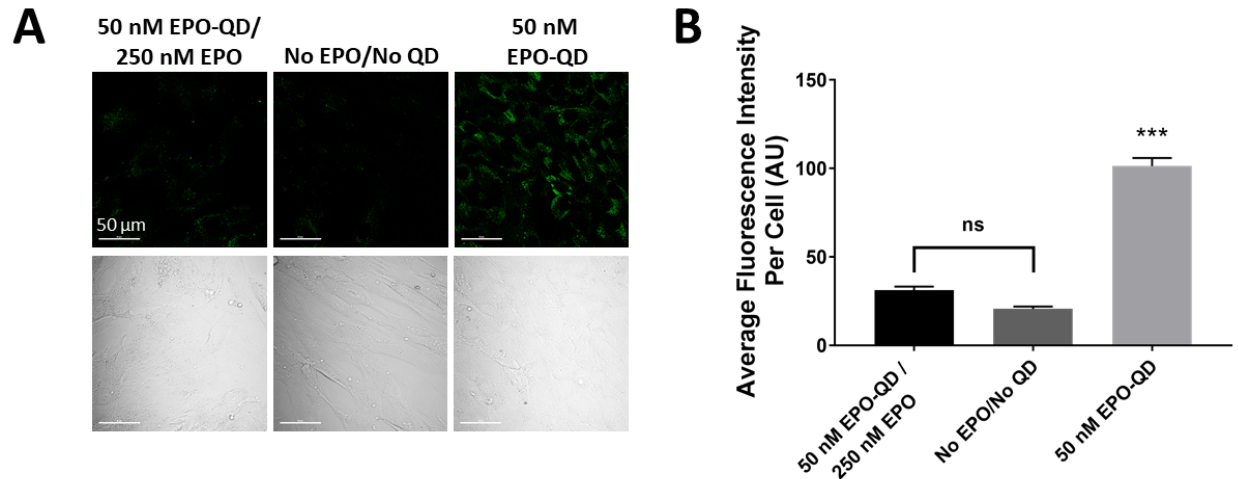


Figure 18. Competitive EPO-QD binding assay in HA. (A) HA were incubated with 50 nM EPO-QD or 50 nM EPO-QD plus 250 nM free EPO to demonstrate specificity of binding of the EPO-QD conjugates to the EPOR. (B) Quantification of the image data in (A). The average fluorescence intensity per cell ($n = 62$ cells each condition) shows statistically significant difference (one way ANOVA, $p < 0.001$) between EPO-QD and EPO-QD plus free EPO.

Induction of AQP4 expression by EPO and EPO-QD bioconjugates. Having characterized the optimal conditions for binding of EPO-QD conjugates to HA cells, we next characterized the EPO-QD-induced activation of the JAK/STAT signaling pathway and the induction of AQP4 expression. The activation of the JAK/STAT signaling pathway in HA was quantified using a sandwich ELISA for the detection of phosphorylated JAK2 proteins after cells were incubated for 24 h with 50 nM EPO or 50 nM EPO/10 nM QD (Figure 19). Under these conditions, EPO-QD conjugates induced a two-fold greater phosphorylation of JAK2 compared to free EPO (Figure 19). Similar to our results here, Al-Sarraf *et al.* showed the important role played by EPO-induced JAK signaling in EPO-mediated protection against anoxia in cultured astrocytes.¹³⁰ Liu *et al.* reported similar results in EPO-mediated protection against oxidative stress in rat astrocytes.¹³¹

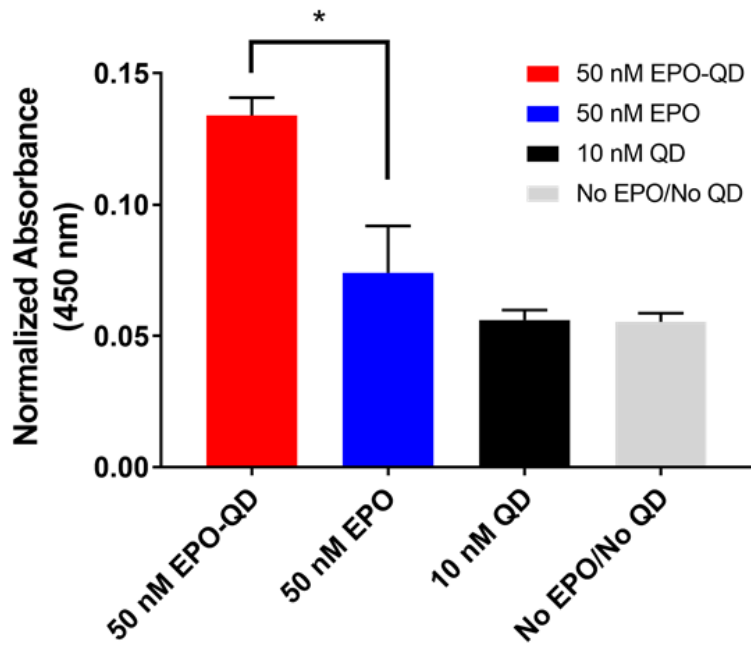


Figure 19. Quantification of JAK2 phosphorylation in HA. A sandwich ELISA was used to quantify the levels of JAK2 phosphorylation in HA in response to EPO-QD or free EPO. HA cell lysates were captured by anti-JAK mAb and detected with a mAb directed against phosphorylated JAK2. Detection was achieved with a horseradish peroxidase conjugate/TMB substrate system. One way ANOVA showed statistical significance ($p < 0.05$) between EPO-QD and EPO alone.

We next confirmed the induction of expression of AQP4 using IHC (Figure 20A). HA monolayers incubated with free EPO or EPO-QD under the same conditions as those used for the ELISA were probed with an anti AQP4 monoclonal antibody and a TRITC-labeled secondary antibody. Quantification of the fluorescence images revealed that across all EPO concentrations there were statistically significant differences between free EPO and EPO-QD conjugates in the induction of AQP4 expression (Figure 20B). Notably, at a ratio of 5 EPO/QD we observed a 1.8-fold increase in AQP4 expression over the level of induction mediated by free EPO at the same concentration. While it is established that EPO induces the upregulation and expression of AQP4 in astrocytes both *in vitro*¹³² and *in vivo*¹¹⁰, our results here demonstrating the greater level of JAK/STAT signaling and overall induction of protein expression by EPO-QD versus free

EPO are, to our knowledge, the first demonstration of the augmented expression of AQPN-4 mediated by a NP-displayed form of EPO.

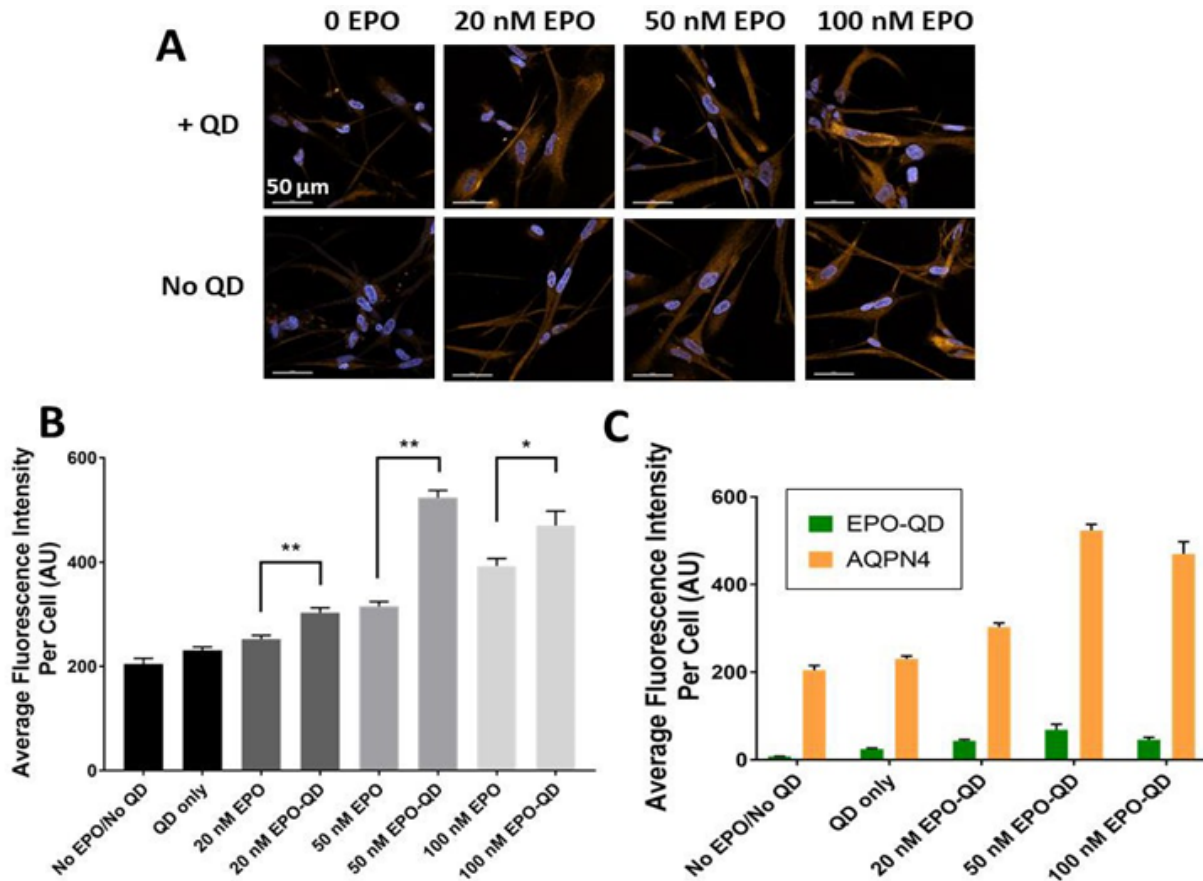


Figure 20. Induction of AQPN-4 expression by free EPO and EPO-QD. (A) EPO-QD appended with EPO protein at 20, 50, or 100 nM (corresponding to 2, 5, or 10 copies/QD) (top row) or free EPO (bottom row) were incubated on HA for 24 h and then cells were probed with antibodies to quantify AQPN-4 expression. QDs were used at 10 nM when present. (B) Quantification of AQPN-4 expression shows that in all cases, EPO-QD induces a greater level of AQPN-4 expression compared to free EPO at the same concentration. 5 EPO/QD is the best case where AQPN-4 induction was increased by 1.8-fold. * indicates $p < 0.05$; ** indicates $p < 0.001$. The data correspond to analysis of at least 100 cells across two independent experiments. (C) The level of AQPN-4 expression tracks directly with the level of EPO-QD binding to the plasma membrane as seen in Figure 15B.

Quantification of water transport in EPO and EPO-QD-treated HA. The critical question in this study was whether the increased expression of AQPN-4 induced by EPO-QD translates into increased water transport in treated HA cells. To address this, we performed water transport assays

based on the quenching of calcein AM (Figure 21). Using a modified protocol described by Kitchen *et al.*, we first treated HA with either 50 nM EPO or 50 nM EPO/10 nM QD for 24 h to induce expression of AQP4 as detailed previously.¹²⁴ Cells were then washed and loaded with calcein AM and we then rendered the extracellular environment hypertonic by the addition of 0.5M NaCl. As calcein AM self-quenches when its concentration increases, the movement of water out of the cells under hypertonic conditions results in a time-resolved decrease of calcein AM fluorescence intensity. Indeed, the fluorescence images in Figure 21A show that, in cells treated with 50 nM EPO/10 nM QD for 24 h, when we tracked the calcein AM signal over 90 min there was a concomitant decrease in the signal intensity. Figure 21B shows the calcein AM signal traces for HA treated with 50 nM EPO or 50 nM EPO/10 nM QD or control cells treated with either 10 nM QD or no treatment. Notably, the most rapid change in signal was observed in the 20 to 30 sec time window, immediately after addition of the NaCl to the dish at $t = 20$ sec, corresponding to rapid water efflux followed by immediate calcein AM quenching. The data in the 20 to 30 sec time window were fitted with the exponential equation $y = Ce^{(-kt)}$ where t is time in sec, k is proportional to the plasma membrane permeability/water transport rate, and C is an amplitude fit parameter for the normalized data (Figure 21C). A comparison of the k values in that 10 sec time window across the samples demonstrated several key features. First, both 50 nM EPO and 50 nM EPO/10 nM QD exhibited statistically greater water transport rates than HA incubated with 10 nM QDs alone or control cells by themselves. Further, the relative water transport rate of HA cells incubated with EPO-QD ($k = 0.103$) was approximately twice that of cells incubated with free EPO ($k = 0.055$) ($p < 0.0001$), providing clear evidence of the functional impact of the increased AQP4 expression mediated by the EPO-QD conjugates (Figure 22).

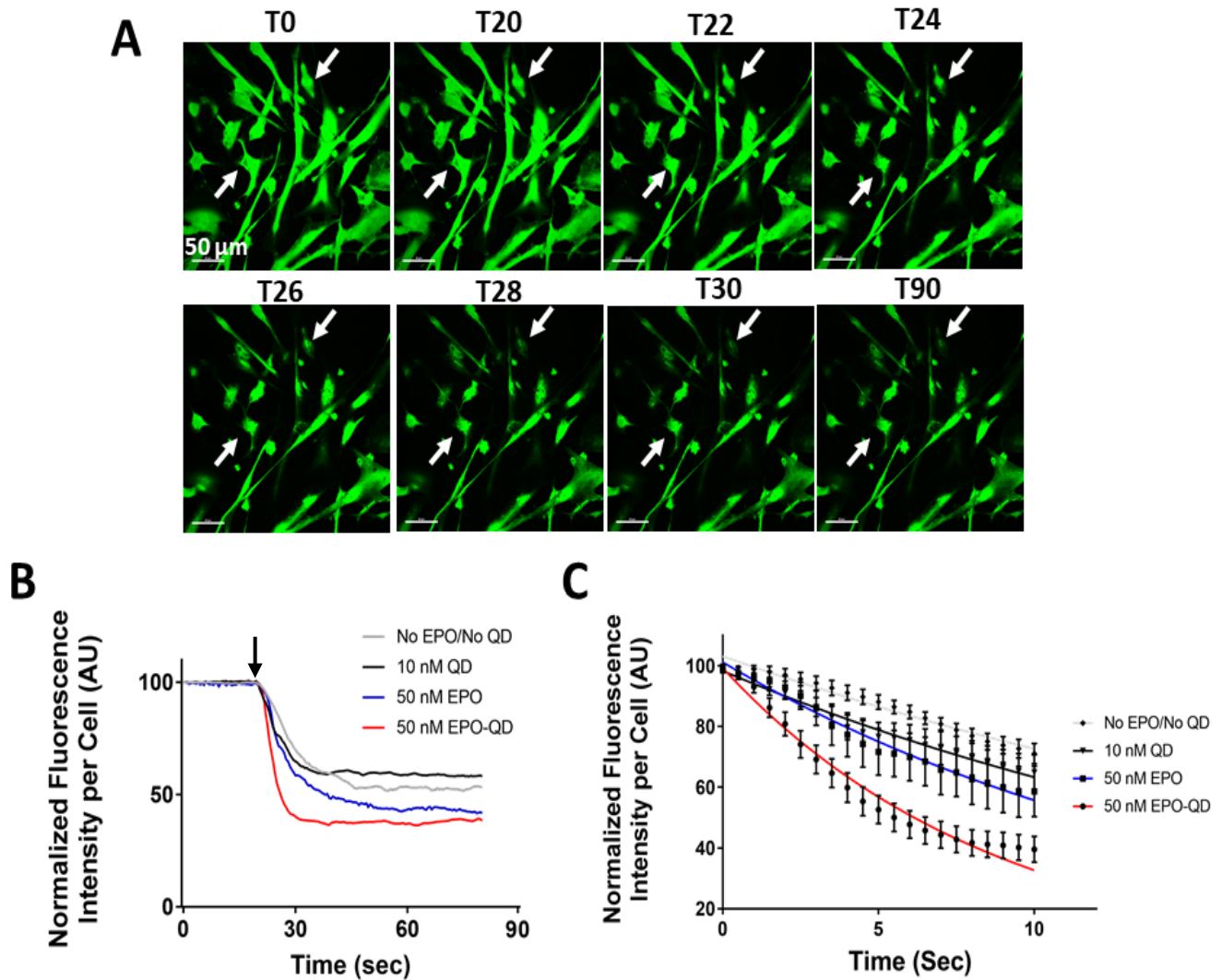


Figure 21. Quantification of water transport in EPO treated HA using calcein AM assay. A calcein AM quenching assay was used to visibly track and quantify the rate of water efflux in HA treated with EPO-QD or free EPO. Calcein AM fluorescence quenches with increasing dye concentration. When water effluxes out of the cell, calcein AM concentration increases, resulting in its quenched fluorescence. (A) Time-resolved calcein AM quenching. After incubation with 50 nM EPO-QD (10 nM QD/5 EPO per QD) for 24 h, HA were loaded with calcein AM. Starting in physiological salt conditions (300 mOsmol, isotonic) at T0 sec (high calcein fluorescence), the extracellular solution was made hypertonic (~500 mOsmol) at T20 sec by addition of NaCl (black arrow). Calcein AM fluorescence begins to quench at T20 sec, indicative of water efflux. The white arrows highlight two cells in each frame for ease of tracking fluorescence change. (B) Plot of the comparative calcein AM quenching extracted from the images in panel A. Each data trace corresponds to the average of 60 cells and is representative of four independent experiments. (C) Plots of the calcein AM fluorescence response over the time period T20 sec - T30 sec (from the traces in panel B) are fit to the exponential identity $y = Ce^{(-kt)}$ where k is proportional to the membrane water permeability or water transport rate. The curve fit values (R^2) are: 50 nM EPO-QD, 0.94; 50 nM EPO, 0.96; QD only, 0.98; and no EPO/no QD, 0.98.

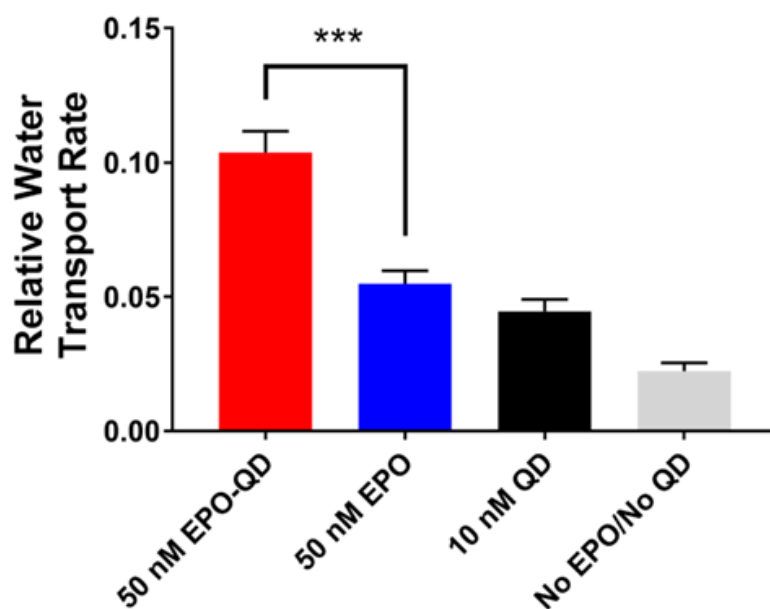


Figure 22. Quantification of relative water transport rates in EPO-treated HA. Plotted are the water transport rates determined from the curve-fit of the quenching plots in Figure 21C. *** indicates $p < 0.001$. The values of (the water permeability rate constant) were found to be as follows: 50 nM EPO-QD, $k = 0.103$; for 50 nM EPO, $k = 0.055$; for 10 nM QD control, $k = 0.044$; for untreated cell control (No EPO/No QD), $k = 0.022$.

Cytotoxicity of EPO-QD bioconjugates.

Finally, we assessed the effect of the incubation of HA with EPO-QD (or free EPO) on HA cellular proliferation under the conditions required to induce the increased expression of AQP4. Controls again included HA cells incubated with 10 nM QDs alone or untreated cells (medium only) (Figure 23). Here, we saw no statistical difference in cell viability between cells treated with the EPO-QD conjugates, EPO alone, or QDs alone compared to untreated control cells. These results demonstrate not only the negligible impact on HA cellular health in the context of EPO-QD-induced AQP4 expression but they further exemplify the minimal impact of the QD scaffold on cellular viability. Indeed, our previous work has established the biocompatibility of high

quality, colloiddally stable QDs as a scaffold for the transport and delivery of a range of biologicals (proteins, peptide, nucleic acids).¹¹⁴⁻¹²⁰

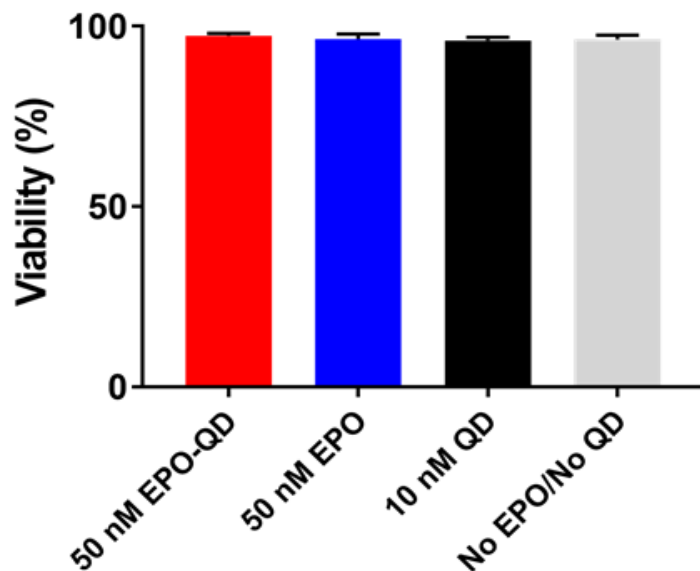


Figure 23. Cytotoxicity of EPO and EPO-QD bioconjugates. HA cell mono- layers were incubated for 24-48 hr with the materials as indicated and then a live/dead cell analysis (calcein/ethidium homodimer 1) was performed. The data show greater than 96% cell viability for all treatment conditions and the control (no EPO/no QD).

Conclusion

The use of NPs for the regulation and control of cellular physiology and behavior is an ever-expanding focal area of bionanotechnology research. Specifically, the use of NP bioconjugates for the control of gene expression continues to develop at a rapid pace. To date, the vast majority of strategies for NP-mediated modulation of gene expression within cells have relied on the delivery of gene-encoding plasmids, mRNA, or CRISPR-Cas9 tools. Indeed, the recently developed COVID-19 vaccines, mRNA-based liposomal NPs to direct the synthesis of SARS-CoV-2 spike protein, highlight the utility of NP carriers for controlled cellular gene expression.¹³³⁻

¹³⁵ One area, however, that remains ripe for exploration is the use of NPs for the extracellular induction of intracellular signaling and gene expression. There are numerous literature examples of the latter, particularly in the context of NP-mediated activation of G protein-coupled receptors (reviewed in Ma, *et al.*).¹³⁶ However, reports of the use of growth factor-functionalized NPs for the activation of intracellular signaling and protein expression remain limited. Yamamoto *et al.* showed that EGF-gold NP (AuNP) conjugates modulate EGF signaling by altering the nature of EGF-EGF receptor (EGFR) endocytosis and downstream kinase activity.¹³⁷ More recently, Zhang *et al.* demonstrated that the multivalent presentation of EGF on AuNPs augmented the phosphorylation of EGFR and the formation of reactive oxygen species.¹³⁸

In this study, we have presented a NP-based strategy for the controlled induction of AQPN-4 expression in HA cells that is built upon the self-assembly and multivalent display of EPO on the surface of a 5 nm QD scaffold. Given that EPOR are known to cluster upon binding of EPO and subsequent signaling, our working hypothesis was that the multivalent presentation of EPO to EPOR would facilitate enhanced JAK/STAT signaling and synthesis of AQPN-4 membrane channels. Indeed, the incubation of 50 nM EPO self-assembled to 10 nM QD (5 EPO/QD) for 24 h on HA results in a 1.8-fold increase in AQPN-4 expression compared to free EPO at the same concentration. This is coupled with the augmentation of intracellular JAK kinase activity. This, in turn, translates to a 2-fold increase in the water transport rate from HA cells treated with EPO-QD compared to free EPO. Importantly, treatment of HA with EPO-QD for water transport augmentation has no deleterious effect on HA viability. Cumulatively, our findings detailed here build upon previous work that have shown the capability to modulate intracellular signaling and cellular behavior with growth factor-NP bioconjugates. Still many interesting questions remain regarding the nature of the interaction of these conjugates with HA (and other cell types).

Specifically, we hypothesize that NP size, curvature, and surface topography (spherical vs. faceted vs. lobed) plays a profound role in the efficacy of growth factor-receptor interaction when presented to cells. These studies are currently ongoing in our laboratory and we anticipate that the lessons learned will impact the future development of growth factor-NP conjugates as both research tools and clinical therapeutics.

Chapter 5: Conclusions and Future Outlook

The ability to modulate single cell function and behavior is critical for the continued development of a thorough understanding of cellular signaling and pathways. Additionally, this ability is paramount for the expansion of therapeutics that can modify cell function with high temporal and spatial specificity. The current favored strategy to achieve these ends is typically nucleic acid technology, such as CRISPR or the introduction of siRNA or mRNA into the cell. These approaches, while effective, may permanently modify genetic information and are difficult to deliver to the nucleus efficiently due to the nuclear membrane acting as a barrier. Furthermore, these methods often require viral vectors for efficient delivery, which can lead to off-target effects and immune responses.¹⁴⁰⁻¹⁴² Bio-functional NPs can address some of these limitations as they are nonpermanent, able to be introduced directly to the site of disease and are more stable than nucleic acids. They are also highly tunable in size on the nanoscale, shape, and physical properties, can be made to display a wide variety of biological moieties which can be tailored to any target, and can have multifunctional imaging and therapeutic capabilities.¹⁹ The work presented in this thesis explores the use of two types of hard NPs to control cell function.

In Specific Aim 1, we focused on the use of photoexcited anisotropic-shaped AuNFs to modulate membrane potential. Membrane potential is a fundamental cellular property that is crucial for various cellular functions, including the propagation of nerve impulses in neurons and muscle contraction in muscle cells. Abnormalities in membrane potential can lead to various diseases, including epilepsy and certain types of cancer.¹⁴³⁻¹⁴⁶ Therefore, the ability to control membrane potential can have significant remedial implications for these conditions. Building upon previous research in the Delehanty Laboratory utilizing AuNSs for depolarization of cellular membrane potential, we examined the effectiveness of AuNF-PEG-Chol in depolarizing PC-12

cell membranes as compared to AuNS-PEG-Chol.^{57,77,147} In particular, the use of AuNFs, which have a broad absorption extending into the near-infrared (NIR) region of the spectrum, allows for increased tissue penetration depth of activation light *in vivo* and increased responsiveness to NIR laser photoexcitation.⁸¹ We found that AuNF-PEG-Chol more efficiently induced membrane depolarization relative to AuNS-PEG-Chol when a relatively lower laser power is used within the 500-600 nm spectrum where the optical densities of both groups were set to equal. This surprising discovery implies that the novel anisotropic shape of AuNF-PEG-Chol may contribute to greater photothermal heating and stimulation at the cell plasma membrane. Overall, this work has contributed to a deeper understanding of the laser pulse-induced photothermal method and has furthered our understanding of the use of photothermal heating of AuNPs to increase cell temperature by a few degrees. This is a significant departure from the more well-explored harsh uses of photothermal heating in cancer ablation using AuNPs, which typically involve heating the NPs to temperatures high enough to kill cancer cells. Our approach, on the other hand, involves a more subtle modulation of cell surface temperature, which as demonstrated can have profound effects on cell function with high temporal control and without causing cell death.

Specific Aim 2 focused on the multivalent display of EPO on QDs. EPO is a glycoprotein that has been shown to have neuroprotective effects and can upregulate AQP4 expression. AQP4 is a water channel protein that is expressed in a polarized manner on astrocyte endfeet and it facilitates the clearance of waste products through the convective transport of fluid and solutes. It is a critical component of the glymphatic system, which clears the brain of waste during sleep to restore and maintain optimal cognitive function.¹⁰⁴ The dysregulation of the glymphatic system has also been postulated to play a role in the onset of neurodegenerative diseases. Thus, the ability to upregulate AQP4 expression can have significant implications for the treatment of

various neurological conditions, including Alzheimer's disease and traumatic brain injury.^{C11} Introducing semiconductor QDs expressing a multivalent display of EPO (EPO-QD) resulted in an enhancement in AQP4 expression as well as the water transport rate in HA as compared to monomeric EPO introduced at the same concentration for a similar time of incubation. Importantly, the EPO-QD-induced augmented AQP4 expression did not negatively impact astrocyte viability. This work has established a new paradigm for initiating cellular signaling and protein expression with QD conjugates, particularly with the attachment of growth factors to a trackable semiconductor QD to alter protein expression within a cell. This area of research is currently extremely underexplored, with only a few papers on the subject.⁶⁷ However, the potential benefits for this technology are enormous. Potential applications of EPO-NP conjugates to modulate and improve glymphatic system efficiency could act as a potential treatment for patients suffering from insomnia, traumatic brain injury, and improving warfighter performance during deployment in the field, where sleep debt is a major concern. From a more fundamental science perspective, our findings contribute to the understanding of interactions between NPs and cell processes and provide new insights into the potential of QDs as scaffolds for growth factor-based therapeutic agents within the glymphatic system.

The work enabled for the Delehanty Laboratory by this thesis is significant. It has expanded upon previous work in developing AuNPs for modulated control of cell membrane depolarization. Specifically, it has built upon the work of Muroski *et al.*, who examined the effects of varying the length of PEG linker and cholesterol moiety on the effectiveness of cell membrane depolarization.⁵⁷ Herein, we have improved upon this paradigm by using AuNFs, which can be stimulated using NIR light wavelengths, thereby increasing their potential for *in vivo* applications through tissue. The cumulative findings detailed in this thesis also build upon previous work that

has shown the capability to modulate intracellular signaling and cellular behavior with growth factor-NP bioconjugates, and work that describes the benefits of a multivalent presentation of growth factors on a NP scaffold. In particular, the use of QDs as an underexplored tool for this purpose has been particularly significant. These findings pave the way for future studies within the Delehanty Laboratory to expand upon both aims separately or with a combinatorial approach. It is known that the shape that cells “see” often determines how they respond to what is attached.^{74,86,148} Thus, attachment of EPO or other growth factors to an anisotropic AuNF scaffold has the potential to allow one to controllably enhance or change how HA respond to EPO; a schematic of this system is illustrated in Figure 24.

Additionally, the work using QD-EPO is supportive of the findings by McGraw et. al. suggesting that EPOR clustering upon binding with EPO is raft dependent.¹¹³ Further investigations concerning the nature of EPOR clustering in response to EPO presented on a multivalent NP scaffold are expected to follow within the Delehanty Laboratory. First, HA may be genetically manipulated using plasmid transfection to produce recombinant EPOR expressing a red fluorescent mCherry protein tag on the cytoplasmic domain. These EPOR-mCherry-expressing HA will be treated with QD-EPO bioconjugates and imaged to visualize receptor clustering and aggregation over time using confocal microscopy; these data can be quantified using co-localization analysis. In a second set of experiments, two equal populations of recombinant EPOR will be expressed in cells, with one population containing EPOR tagged with green GFP and the other containing EPOR tagged with red mCherry. Fluorescence resonance energy transfer (FRET)-based techniques have been successful when utilized to determine receptor-ligand and receptor clustering interactions.¹⁴⁹⁻¹⁵¹ Here, FRET may be used to great effect to quantify EPOR cluster formation, where energy transfer occurs between closely spaced GFP and mCherry

fluorophores. Cells treated with QD-EPO are expected to show greater FRET efficiency compared to free EPO treatment, indicative of denser EPOR clustering mediated by the multivalent EPO presentation on QDs. These planned experiments will provide further insight into the mechanism of enhanced EPOR activation by QD-EPO and will allow for observation of a direct comparison of EPOR clustering behavior between cells treated with free EPO vs. those treated with QD-multivalent EPO.

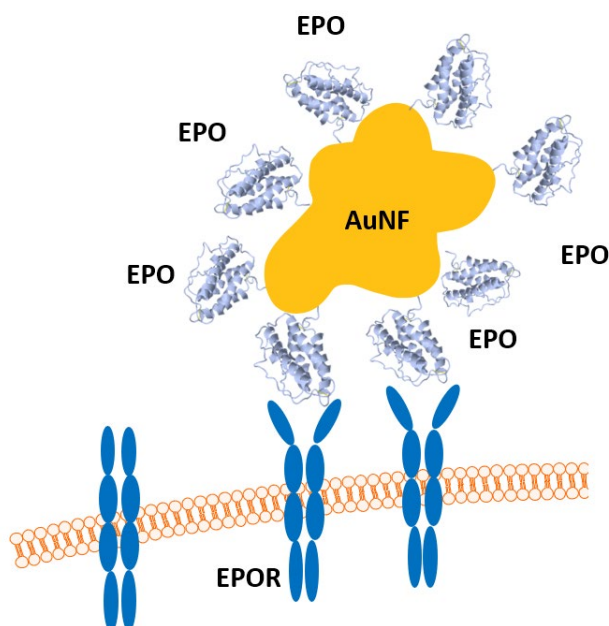


Figure 24. Schematic of a combinatorial approach using techniques explored in Aim 1 and Aim 2. An AuNF scaffold is used to present a growth factor display (such as EPO) to the matching receptors on the plasma membrane in order to enhance the cellular response.

Looking forward, the systems presented here can be applied to other hard NP platforms. Future studies might directly compare different types of anisotropic AuNPs (such as nanorods, nanostars, and NFs) and examine their effectiveness in facilitating cellular membrane depolarization. Within the Delehanty Lab, there are multiple potential studies that will enhance the

work using EPO-QDs, or QDs attached to other growth factors, to modify the signaling pathways and protein expression within cells; the role of NP size, curvature, and surface topography could be explored in the efficacy of growth factor-receptor interactions. Further works could also explore the use of alternate QDs, such as graphene QDs, in this endeavor. Alternatively, these experiments could be attempted in a 3D matrix as opposed to with a 2D monolayer of cells. This would provide a more realistic model of the *in vivo* environment and could yield important insights into the potential therapeutic applications of AuNPs and QDs. In conclusion, the work presented in this thesis has significantly advanced our understanding of how hard NPs can be used to control cellular behavior and function. It demonstrates the potential of anisotropic-shaped AuNPs and growth-factor presenting QDs for modulating membrane potential and protein expression, respectively. These findings help to provide a strong foundation for future research in the field of NP-mediated cellular modulation.

Appendix

Contribution to Science

Publications

- 1) Photothermal-Enhanced Modulation of Cellular Membrane Potential Using Long-Wavelength-Activated Gold Nanoflowers.** Rogers, K. E., Nag, O. K., Susumu, K., Oh, E., & Delehanty, J. B. (2023). *Bioconjugate Chemistry*. 34(2), 405-413. *Supplemental Cover*.
- 2) Multivalent Display of Erythropoietin on Quantum Dots Enhances Aquaporin-4 Expression and Water Transport in Human Astrocytes *In Vitro*.** Rogers, K. E., Nag, O. K., Stewart, M.H., Susumu, K., Oh, E., & Delehanty, J. B. (2023). *In Submission*.
- 3) Determining the Cytosolic Stability of Small DNA Nanostructures *In Cellula*.** Mathur, D., Rogers, K. E., Diaz, S. A., Muroski, M. E., Klein, W. P., Nag, O. K., Lee, K., Field, L. D., Delehanty, J. B., Medintz, I. L. (2022). *Nano Letters*. 22(12), 5037-5045.
- 4) Seedless Synthesis of Anisotropic Gold Nanoflowers and their Use in Cellular Control and Drug Delivery Applications.** Oh, E., Susumu, K., Sangtani, A., Rogers, K. E., Nag, O.K., Lee, K., Vurgaftman, I., Weiblin, R. J., Kim, M., Delehanty, J. (2022). Filed as US patent application ser. no. 18/197195 and international patent application PCT/US23/22214 (approved for international filing).
- 5) Nanoparticle (NP)-enhanced Expression of Aquaporin-4 Channels and Water Transport in Human Astrocytes.** Rogers, K.E., Nag, O.K., Stewart, M.H., Oh, E., Delehanty, J.B. Navy Case # 211467 (approved by NRL Invention Evaluation Board for USPTO filing; provisional patent filed; nonprovisional application in preparation).
- 6) Hydrodynamic Focusing-Enabled Blood Vessel Fabrication for *in vitro* Modeling of the Blood Brain Barrier.** Divito, K., Luo, J., Rogers, K. E., Sundaram, S, Dahal, B., Hoek, M.V., Kehn-Hall, K., Delehanty, J., Adams, A.A. (2021). *Journal of Medical and Biological Engineering*, 41(4), 456-469
- 7) Recent Advances in the Use of Cadmium-free Quantum Dots for Bioimaging.** Rogers, K.E., Nag, O.K., Stewart, M.H., and Delehanty, J.B. (2021). *Material Matters*, 16.2.
- 8) Sensing Nitric Oxide in Cells: Historical Technologies and Future Outlook.** Almeida, B., Rogers, K. E., Nag, O. K., & Delehanty, J. B. (2021). *ACS sensors*, 6(5), 1695-1703.
- 9) Recent Progress in Bioconjugation Strategies for Liposome-Mediated Drug Delivery.** Almeida, B., Nag, O.K., Rogers, K. E. and Delehanty, J.B. (2020). *Molecules*, 25(23), p.5672.

Presentations

Department of Defense 6.1 Basic Research Conference.

Rogers, K. E., Oh, E., Nag, O.K., Delehanty, J. B. Improved Gold Nanoflower Mediated Depolarization of Cellular Membrane Potential. (2022)

Chemical and Biological Defense Science and Technology Conference.

Rogers K. E., Divito, K, Luo, J, et al. 3D Blood-Brain Barrier Tissue Engineering for Pathobiological Studies of Alpha-Viruses. (2017)

Photothermal-Enhanced Modulation of Cellular Membrane Potential Using Long-Wavelength-Activated Gold Nanoflowers



Author: Katherine E. Rogers, Okhil K. Nag, Kimihiro Susumu, et al

Publication: Bioconjugate Chemistry

Publisher: American Chemical Society

Date: Feb 1, 2023

Copyright © 2023, American Chemical Society

PERMISSION/LICENSE IS GRANTED FOR YOUR ORDER AT NO CHARGE

This type of permission/license, instead of the standard Terms and Conditions, is sent to you because no fee is being charged for your order. Please note the following:

- Permission is granted for your request in both print and electronic formats, and translations.
- If figures and/or tables were requested, they may be adapted or used in part.
- Please print this page for your records and send a copy of it to your publisher/graduate school.
- Appropriate credit for the requested material should be given as follows: "Reprinted (adapted) with permission from {COMPLETE REFERENCE CITATION}. Copyright {YEAR} American Chemical Society." Insert appropriate information in place of the capitalized words.
- One-time permission is granted only for the use specified in your RightsLink request. No additional uses are granted (such as derivative works or other editions). For any uses, please submit a new request.

If credit is given to another source for the material you requested from RightsLink, permission must be obtained from that source.

BACK

CLOSE WINDOW



Display of Potassium Channel-Blocking Tertiapin-Q Peptides on Gold Nanoparticles Enhances Depolarization of Cellular Membrane Potential

Author: James B. Delehanty, Jeffrey R. Deschamps, Eunkeu Oh, et al
 Publication: Particle & Particle Systems Characterization
 Publisher: John Wiley and Sons
 Date: Jan 28, 2019

© 2019 WILEY-VCH Verlag GmbH & Co. KGaA, Weinheim

Order Completed

Thank you for your order.
 This Agreement between Naval Research Laboratory -- Katherine Rogers ("You") and John Wiley and Sons ("John Wiley and Sons") consists of your license details and the terms and conditions provided by John Wiley and Sons and Copyright Clearance Center.

Your confirmation email will contain your order number for future reference.

| | | |
|-------------------------------------|---|-----------------------------------|
| License Number | 5560421270279 | Printable Details |
| License date | Jun 01, 2023 | |
| Licensed Content | | Order Details |
| Licensed Content Publisher | John Wiley and Sons | Type of use |
| Licensed Content Publication | Particle & Particle Systems Characterization | Dissertation/Thesis |
| Licensed Content Title | Display of Potassium Channel-Blocking Tertiapin-Q Peptides on Gold Nanoparticles Enhances Depolarization of Cellular Membrane Potential | Requestor type |
| Licensed Content Author | James B. Delehanty, Jeffrey R. Deschamps, Eunkeu Oh, et al | University/Academic |
| Licensed Content Date | Jan 28, 2019 | Format |
| Licensed Content Volume | 36 | Print and electronic |
| Licensed Content Issue | 3 | Portion |
| Licensed Content Pages | 6 | Figure/table |
| | | Number of figures/tables |
| | | 4 |
| | | Will you be translating? |
| | | No |

About Your Work

| | |
|-----------------------------------|--|
| Title | Implementation of Nanoparticles for Controlled Modulation of Cellular Behavior |
| Institution name | University of Maryland |
| Expected presentation date | Jul 2023 |

Additional Data

| | |
|-------------------------------|--------------------------------|
| Order reference number | 255 |
| Portions | Figure 1A, Figure 2A, Figure 4 |

Requestor Location

| | |
|---------------------------|--|
| Requestor Location | Naval Research Laboratory 12301 Featherwood Dr APT 22 Silver Spring, MD 20904 United States Attn: Naval Research Laboratory |
|---------------------------|--|

Tax Details

| | |
|-------------------------|-------------|
| Publisher Tax ID | EU826007151 |
|-------------------------|-------------|

Price

| | |
|--------------|----------|
| Total | 0.00 USD |
|--------------|----------|

Would you like to purchase the full text of this article? If so, please continue on to the content ordering system located here: [Purchase PDF](#)
 If you click on the buttons below or close this window, you will not be able to return to the content ordering system.

Total: 0.00 USD

[CLOSE WINDOW](#)

[ORDER MORE](#)

Hesperidin Loaded on Gold Nanoparticles as a Drug Delivery System for a Successful Biocompatible, Anti-Cancer, Anti-Inflammatory and Phagocytosis Inducer Model



Author: Ghassan M. Sulaiman et al
 Publication: Scientific Reports
 Publisher: Springer Nature
 Date: Jun 9, 2020
 Copyright © 2020, The Author(s)

Creative Commons

This is an open access article distributed under the terms of the Creative Commons CC BY license, which permits unrestricted use, distribution, and reproduction in any medium, provided the original work is properly cited.
 You are not required to obtain permission to reuse this article.
 To request permission for a type of use not listed, please contact Springer Nature

This is a License Agreement between Katherine Pendragon ("User") and Copyright Clearance Center, Inc. ("CCC") on behalf of the Rightsholder identified in the order details below. The license consists of the order details, the Marketplace Permissions General Terms and Conditions below, and any Rightsholder Terms and Conditions which are included below. All payments must be made in full to CCC in accordance with the Marketplace Permissions General Terms and Conditions below.

| | | | |
|------------------|-------------|-------------|------------------------------------|
| Order Date | 23-Jun-2023 | Type of Use | Republish in a thesis/dissertation |
| Order License ID | 1368560-1 | Publisher | Royal Society of Chemistry |
| ISSN | 2047-4849 | Portion | Chart/graph/table/figure |

LICENSED CONTENT

| | | | |
|-------------------|--|------------------|---|
| Publication Title | Biomaterials science | Publication Type | e-Journal |
| Article Title | Dual-functional gold nanoparticles with antimicrobial and proangiogenic activities improve the healing of multidrug-resistant bacteria-infected wounds in diabetic mice. | Start Page | 4482 |
| | | End Page | 4490 |
| | | Issue | 11 |
| Author/Editor | Royal Society of Chemistry (Great Britain), Kyoto Daigaku.Bushitsu-Saibo? To?go? Shisutemu Kyoten | Volume | 7 |
| | | URL | http://pubs.rsc.org/en/journals/journaliss... |
| Date | 01/01/2013 | | |
| Language | English | | |
| Country | United Kingdom of Great Britain and Northern Ireland | | |
| Rightsholder | Royal Society of Chemistry | | |

REQUEST DETAILS

| | | | |
|--|--------------------------|-----------------------------|----------------------------------|
| Portion Type | Chart/graph/table/figure | Distribution | Worldwide |
| Number of Charts / Graphs / Tables / Figures Requested | 4 | Translation | Original language of publication |
| Format (select all that apply) | Print, Electronic | Copies for the Disabled? | No |
| Who Will Republish the Content? | Academic institution | Minor Editing Privileges? | No |
| Duration of Use | Life of current edition | Incidental Promotional Use? | No |
| Lifetime Unit Quantity | Up to 499 | Currency | USD |
| Rights Requested | Main product | | |

NEW WORK DETAILS

| | | | |
|-----------------|--|----------------------------|--------------------------------------|
| Title | Implementation of Nanoparticles for the Controlled Modulation of Cellular Behavior | Institution Name | University of Maryland, College Park |
| Instructor Name | Katherine Pendragon | Expected Presentation Date | 2023-07-21 |

ADDITIONAL DETAILS

| | | | |
|------------------------|-----|---|---------------------|
| Order Reference Number | 999 | The Requesting Person/Organization to Appear on the License | Katherine Pendragon |
|------------------------|-----|---|---------------------|

REQUESTED CONTENT DETAILS

| | | | |
|---|---|--|--|
| Title, Description or Numeric Reference of the Portion(s) | Portions of Figures 1-4 | Title of the Article/Chapter the Portion Is From | Dual-functional gold nanoparticles with antimicrobial and proangiogenic activities improve the healing of multidrug-resistant bacteria-infected wounds in diabetic mice. |
| Editor of Portion(s) | Wei, Shih-Chun; Chang, Lung; Huang, Chih-Ching; Chang, Huan-Tsung | Author of Portion(s) | Wei, Shih-Chun; Chang, Lung; Huang, Chih-Ching; Chang, Huan-Tsung |
| Volume / Edition | 7 | Issue, if Republishing an Article From a Serial | 11 |
| Page or Page Range of Portion | 4482-4490 | Publication Date of Portion | 2019-11-01 |

Thermally Triggered in Situ Assembly of Gold Nanoparticles for Cancer Multimodal Imaging and Photothermal Therapy

Author: Mengmeng Sun, Dong Peng, Hanjun Hao, et al
 Publication: Applied Materials
 Publisher: American Chemical Society
 Date: Mar 1, 2017
 Copyright © 2017, American Chemical Society

PERMISSION/LICENSE IS GRANTED FOR YOUR ORDER AT NO CHARGE

This type of permission/license, instead of the standard Terms and Conditions, is sent to you because no fee is being charged for your order. Please note the following:

- Permission is granted for your request in both print and electronic formats, and translations.
- If figures and/or tables were requested, they may be adapted or used in part.
- Please print this page for your records and send a copy of it to your publisher/graduate school.
- Appropriate credit for the requested material should be given as follows: "Reprinted (adapted) with permission from (COMPLETE REFERENCE CITATION). Copyright (YEAR) American Chemical Society." Insert appropriate information in place of the capitalized words.
- One-time permission is granted only for the use specified in your RightsLink request. No additional uses are granted (such as derivative works or other editions). For any uses, please submit a new request.

If credit is given to another source for the material you requested from RightsLink, permission must be obtained from that source.

BACK

CLOSE WINDOW

Peptide-Conjugated Quantum Dots Activate Neuronal Receptors and Initiate Downstream Signaling of Neurite Growth



Author: Tania Q. Vu, Ravikanth Maddipati, Todd A. Blute, et al

Publication: Nano Letters

Publisher: American Chemical Society

Date: Apr 1, 2005

Copyright © 2005, American Chemical Society

PERMISSION/LICENSE IS GRANTED FOR YOUR ORDER AT NO CHARGE

This type of permission/license, instead of the standard Terms and Conditions, is sent to you because no fee is being charged for your order. Please note the following:

- Permission is granted for your request in both print and electronic formats, and translations.
- If figures and/or tables were requested, they may be adapted or used in part.
- Please print this page for your records and send a copy of it to your publisher/graduate school.
- Appropriate credit for the requested material should be given as follows: "Reprinted (adapted) with permission from {COMPLETE REFERENCE CITATION}. Copyright {YEAR} American Chemical Society." Insert appropriate information in place of the capitalized words.
- One-time permission is granted only for the use specified in your RightsLink request. No additional uses are granted (such as derivative works or other editions). For any uses, please submit a new request.

If credit is given to another source for the material you requested from RightsLink, permission must be obtained from that source.

[BACK](#)

[CLOSE WINDOW](#)

Intracellularly Actuated Quantum Dot–Peptide–Doxorubicin Nanobioconjugates for Controlled Drug Delivery via the Endocytic Pathway



Author: Ajneeta Sangtani, Eleonora Petryayeva, Miao Wu, et al

Publication: Bioconjugate Chemistry

Publisher: American Chemical Society

Date: Jan 1, 2018

Copyright © 2018, American Chemical Society

PERMISSION/LICENSE IS GRANTED FOR YOUR ORDER AT NO CHARGE

This type of permission/license, instead of the standard Terms and Conditions, is sent to you because no fee is being charged for your order. Please note the following:

- Permission is granted for your request in both print and electronic formats, and translations.
- If figures and/or tables were requested, they may be adapted or used in part.
- Please print this page for your records and send a copy of it to your publisher/graduate school.
- Appropriate credit for the requested material should be given as follows: "Reprinted (adapted) with permission from {COMPLETE REFERENCE CITATION}. Copyright {YEAR} American Chemical Society." Insert appropriate information in place of the capitalized words.
- One-time permission is granted only for the use specified in your RightsLink request. No additional uses are granted (such as derivative works or other editions). For any uses, please submit a new request.

If credit is given to another source for the material you requested from RightsLink, permission must be obtained from that source.

[BACK](#)

[CLOSE WINDOW](#)

ELSEVIER LICENSE
TERMS AND CONDITIONS

Jun 26, 2023

This Agreement between Naval Research Laboratory -- Katherine Pendragon ("You") and Elsevier ("Elsevier") consists of your license details and the terms and conditions provided by Elsevier and Copyright Clearance Center.

| | |
|------------------------------|--|
| License Number | 5576320675873 |
| License date | Jun 26, 2023 |
| Licensed Content Publisher | Elsevier |
| Licensed Content Publication | Plasmid |
| Licensed Content Title | The cell-penetrating YopM protein-functionalized quantum dot-plasmid DNA conjugate as a novel gene delivery vector |
| Licensed Content Author | Özge Uğurlu,Fırat Barış Barlas,Serap Evran,Suna Timur |
| Licensed Content Date | Jul 1, 2020 |
| Licensed Content Volume | 110 |
| Licensed Content Issue | n/a |
| Licensed Content Pages | 1 |
| Start Page | 102513 |
| End Page | 0 |
| Type of Use | reuse in a thesis/dissertation |
| Portion | figures/tables/illustrations |

Number of figures/tables/illustrations 2

| | |
|--|--|
| Format | both print and electronic |
| Are you the author of this Elsevier article? | No |
| Will you be translating? | No |
| Title | Implementation of Nanoparticles for Controlled Modulation of Cellular Behavior |
| Institution name | University of Maryland |
| Expected presentation date | Jul 2023 |
| Order reference number | 999 |
| Portions | Scheme 1 and Figure 5 |
| Requestor Location | Naval Research Laboratory 12301 Featherwood Dr APT 22 Silver Spring, MD 20904 United States Attn: Naval Research Laboratory |
| Publisher Tax ID | 98-0397604 |
| Total | 0.00 USD |
| Terms and Conditions | |

References

1. Papin, J. A., Hunter, T., Palsson, B. O., and Subramaniam, S. (2005). Reconstruction of cellular signalling networks and analysis of their properties. *Nature Reviews Molecular Cell Biology*, 6(2), 99-111.
2. Marks, F., Klingmüller, U. and Müller-Decker, K. (2008). *Cellular signal processing: an introduction to the molecular mechanisms of signal transduction*. Garland Science.
3. Berridge, M.J., Cobbold, P.H. and Cuthbertson, K.S.R. (1988). Spatial and temporal aspects of cell signalling. *Philosophical Transactions of the Royal Society of London. B, Biological Sciences*, 320(1199), 325-343.
4. Mann, S. (2008). Life as a nanoscale phenomenon. *Angewandte Chemie International Edition*, 47(29), 5306-5320.
5. Castiglioni, A. (2019). *A History of Medicine (Vol. 2)*. Routledge.
6. Kamboj, V.P. (2000). Herbal medicine. *Current Science*, 78(1), 35-39.
7. Shara, M. and Stohs, S.J. (2015). Efficacy and safety of white willow bark (*Salix alba*) extracts. *Phytotherapy Research*, 29(8), 1112-1116.
8. Jones, A.W. (2011). Early drug discovery and the rise of pharmaceutical chemistry. *Drug Testing and Analysis*, 3(6), 337-344.
9. Drews, J. (2000). Drug discovery: a historical perspective. *Science*, 287(5460), 1960-1964.
10. Liljefors, T., Krogsgaard-Larsen, P., and Madsen, U. (Eds.). (2002). *Textbook of Drug Design and Discovery*. CRC Press.
11. Bodelon, G., Costas, C., Perez-Juste, J., Pastoriza-Santos, I. and Liz-Marzan, L.M. (2017). Gold nanoparticles for regulation of cell function and behavior. *Nano Today*, 13, 40-60.
12. Hulla, J.E., Sahu, S.C. and Hayes, A.W. (2015). Nanotechnology: History and future. *Human and Experimental Toxicology*, 34(12), 1318-1321.
13. Krukemeyer, M. G., Krenn, V., Huebner, F., Wagner, W., and Resch, R. (2015). History and possible uses of nanomedicine based on nanoparticles and nanotechnological progress. *Journal of Nanomedicine and Nanotechnology*, 6(6), 336.
14. Ariën, A., and Stoffels, P. (2016). History: potential, challenges, and future development in nanopharmaceutical research and industry. *Pharmaceutical Nanotechnology: Innovation and Production*, 1, 3-12.
15. Halwani, A. A. (2022). Development of pharmaceutical nanomedicines: from the bench to the market. *Pharmaceutics*, 14(1), 106.

16. Astruc, D. (2015). Introduction to nanomedicine. *Molecules*, 21(1), 4.
17. Modena, M. M., Rühle, B., Burg, T. P., and Wuttke, S. (2019). Nanoparticle characterization: what to measure?. *Advanced Materials*, 31(32), 1901556.
18. Sangtani, A., Nag, O. K., Field, L. D., Breger, J. C., and Delehanty, J. B. (2017). Multifunctional nanoparticle composites: progress in the use of soft and hard nanoparticles for drug delivery and imaging. *Wiley Interdisciplinary Reviews: Nanomedicine and Nanobiotechnology*, 9(6), e1466.
19. Singh, R., and Lillard Jr, J. W. (2009). Nanoparticle-based targeted drug delivery. *Experimental and Molecular Pathology*, 86(3), 215-223.
20. Jin, S., and Ye, K. (2007). Nanoparticle-mediated drug delivery and gene therapy. *Biotechnology Progress*, 23(1), 32-41.
21. Zha, S., Wong, K. L., and All, A. H. (2022). Intranasal delivery of functionalized polymeric nanomaterials to the brain. *Advanced Healthcare Materials*, 11(11), 2102610.
22. Niu, L., Chu, L. Y., Burton, S. A., Hansen, K. J., and Panyam, J. (2019). Intradermal delivery of vaccine nanoparticles using hollow microneedle array generates enhanced and balanced immune response. *Journal of Controlled Release*, 294, 268-278.
23. Fam, S. Y., Chee, C. F., Yong, C. Y., Ho, K. L., Mariatulqabtiah, A. R., and Tan, W. S. (2020). Stealth coating of nanoparticles in drug-delivery systems. *Nanomaterials*, 10(4), 787.
24. Goddard, Z. R., Marín, M. J., Russell, D. A., and Searcey, M. (2020). Active targeting of gold nanoparticles as cancer therapeutics. *Chemical Society Reviews*, 49(23), 8774-8789.
25. Maruyama, K. (1998). PEG-liposome in DDS and clinical studies. *Nihon rinsho. Japanese Journal of Clinical Medicine*, 56(3), 632-637.
26. Moore, T.L., Rodriguez-Lorenzo, L., Hirsch, V., Balog, S., Urban, D., Jud, C., Rothen-Rutishauser, B., Lattuada, M. and Petri-Fink, A. (2015). Nanoparticle colloidal stability in cell culture media and impact on cellular interactions. *Chemical Society Reviews*, 44(17), 6287-6305.
27. D Friedman, A., E Claypool, S., and Liu, R. (2013). The smart targeting of nanoparticles. *Current Pharmaceutical Design*, 19(35), 6315-6329.
28. Teow, Y., and Valiyaveetil, S. (2010). Active targeting of cancer cells using folic acid-conjugated platinum nanoparticles. *Nanoscale*, 2(12), 2607-2613.
29. Mitchell, M. J., Billingsley, M. M., Haley, R. M., Wechsler, M. E., Peppas, N. A., and Langer, R. (2021). Engineering precision nanoparticles for drug delivery. *Nature Reviews Drug Discovery*, 20(2), 101-124.

30. Bose, R. J., Lee, S. H., and Park, H. (2016). Biofunctionalized nanoparticles: an emerging drug delivery platform for various disease treatments. *Drug Discovery today*, 21(8), 1303-1312.
31. Etheridge, M. L., Campbell, S. A., Erdman, A. G., Haynes, C. L., Wolf, S. M., and McCullough, J. (2013). The big picture on nanomedicine: the state of investigational and approved nanomedicine products. *Nanomedicine: Nanotechnology, Biology and Medicine*, 9(1), 1-14.
32. Wilson, B., and Geetha, K. M. (2022). Lipid nanoparticles in the development of mRNA vaccines for COVID-19. *Journal of Drug Delivery Science and Technology*, 74, 103553.
33. Liu, L., Wang, W., Ju, X. J., Xie, R., and Chu, L. Y. (2010). Smart thermo-triggered squirting capsules for nanoparticle delivery. *Soft Matter*, 6(16), 3759-3763.
34. Lombardo, D., Kiselev, M. A., Magazù, S., and Calandra, P. (2015). Amphiphiles self-assembly: basic concepts and future perspectives of supramolecular approaches. *Advances in Condensed Matter Physics*, 2015.
35. Lombardo, D., Calandra, P., Barreca, D., Magazù, S., and Kiselev, M. A. (2016). Soft interaction in liposome nanocarriers for therapeutic drug delivery. *Nanomaterials*, 6(7), 125.
36. Qiao, R., Yang, C., and Gao, M. (2009). Superparamagnetic iron oxide nanoparticles: from preparations to in vivo MRI applications. *Journal of Materials Chemistry*, 19(35), 6274-6293.
37. Zrazhevskiy, P., Sena, M., and Gao, X. (2010). Designing multifunctional quantum dots for bioimaging, detection, and drug delivery. *Chemical Society Reviews*, 39(11), 4326-4354.
38. Ghaderi, S., Ramesh, B., and Seifalian, A. M. (2011). Fluorescence nanoparticles “quantum dots” as drug delivery system and their toxicity: a review. *Journal of Drug Targeting*, 19(7), 475-486.
39. Volkov, Y. (2015). Quantum dots in nanomedicine: recent trends, advances and unresolved issues. *Biochemical and Biophysical Research Communications*, 468(3), 419-427.
40. Bajpai, S., Tiwary, S.K., Sonker, M., Joshi, A., Gupta, V., Kumar, Y., Shreyash, N. and Biswas, S. (2021). Recent advances in nanoparticle-based cancer treatment: a review. *ACS Applied Nano Materials*, 4(7), 6441-6470.
41. Khan, M. S., Vishakante, G. D., and Siddaramaiah, H. (2013). Gold nanoparticles: a paradigm shift in biomedical applications. *Advances in Colloid and Interface Science*, 199, 44-58.
42. Elahi, N., Kamali, M., and Baghersad, M. H. (2018). Recent biomedical applications of gold nanoparticles: A review. *Talanta*, 184, 537-556.

43. Zhao, P., Li, N., and Astruc, D. (2013). State of the art in gold nanoparticle synthesis. *Coordination Chemistry Reviews*, 257(3-4), 638-665.
44. Herizchi, R., Abbasi, E., Milani, M., and Akbarzadeh, A. (2016). Current methods for synthesis of gold nanoparticles. *Artificial cells, Nanomedicine, and Biotechnology*, 44(2), 596-602.
45. Dreaden, E. C., Alkilany, A. M., Huang, X., Murphy, C. J., and El-Sayed, M. A. (2012). The golden age: gold nanoparticles for biomedicine. *Chemical Society Reviews*, 41(7), 2740-2779.
46. Phiri, M. M., Mulder, D. W., and Vorster, B. C. (2019). Seedless gold nanostars with seed-like advantages for biosensing applications. *Royal Society Open Science*, 6(2), 181971.
47. Sangtani, A., Lee, K., Nag, O.K., Susumu, K., Weiblen, R.J., Kim, M., Vurgaftman, I., Liou, S.C., Delehanty, J.B. and Oh, E. (2022). Seedless Synthesis of Disulfide-Grafted Gold Nanoflowers with Size and Shape Control and Their Photothermally Mediated Cell Perforation. *Chemistry of Materials*, 35(1), 163-176.
48. Wang, S., Lu, W., Tovmachenko, O., Rai, U. S., Yu, H., and Ray, P. C. (2008). Challenge in understanding size and shape dependent toxicity of gold nanomaterials in human skin keratinocytes. *Chemical Physics Letters*, 463(1-3), 145-149.
49. Mahato, K., Nagpal, S., Shah, M.A., Srivastava, A., Maurya, P.K., Roy, S., Jaiswal, A., Singh, R. and Chandra, P. (2019). Gold nanoparticle surface engineering strategies and their applications in biomedicine and diagnostics. *3 Biotech*, 9, 1-19.
50. Huang, X., Jain, P. K., El-Sayed, I. H., and El-Sayed, M. A. (2008). Plasmonic photothermal therapy (PPTT) using gold nanoparticles. *Lasers in Medical Science*, 23, 217-228.
51. Ali, M. R., Wu, Y., and El-Sayed, M. A. (2019). Gold-nanoparticle-assisted plasmonic photothermal therapy advances toward clinical application. *The Journal of Physical Chemistry C*, 123(25), 15375-15393.
52. Pissuwan, D., Valenzuela, S. M., and Cortie, M. B. (2006). Therapeutic possibilities of plasmonically heated gold nanoparticles. *Trends in Biotechnology*, 24(2), 62-67.
53. Sun, M., Peng, D., Hao, H., Hu, J., Wang, D., Wang, K., Liu, J., Guo, X., Wei, Y. and Gao, W. (2017). Thermally triggered in situ assembly of gold nanoparticles for cancer multimodal imaging and photothermal therapy. *ACS Applied Materials and Interfaces*, 9(12), 10453-10460.
54. Muroski, M. E., Oh, E., Deschamps, J., and Delehanty, J. B. (2019). Display of Potassium Channel-Blocking Tertiapin-Q Peptides on Gold Nanoparticles Enhances Depolarization of Cellular Membrane Potential. *Particle and Particle Systems Characterization*, 36(3), 1800493.
55. Sulaiman, G. M., Waheeb, H. M., Jabir, M. S., Khazaal, S. H., Dewir, Y. H., and Naidoo, Y. (2020). Hesperidin loaded on gold nanoparticles as a drug delivery system for a successful

biocompatible, anti-cancer, anti-inflammatory and phagocytosis inducer model. *Scientific Reports*, 10(1), 9362.

56. Wei, S. C., Chang, L., Huang, C. C., and Chang, H. T. (2019). Dual-functional gold nanoparticles with antimicrobial and proangiogenic activities improve the healing of multidrug-resistant bacteria-infected wounds in diabetic mice. *Biomaterials Science*, 7(11), 4482-4490.

57. Muroski, M. E., Oh, E., Nag, O. K., Medintz, I. L., Efros, A. L., Huston, A., and Delehanty, J. B. (2020). Gold-nanoparticle-mediated depolarization of membrane potential is dependent on concentration and tethering distance from the plasma membrane. *Bioconjugate Chemistry*, 31(3), 567-576.

58. Sibuyi, N. R. S., Moabelo, K. L., Fadaka, A. O., Meyer, S., Onani, M. O., Madiehe, A. M., and Meyer, M. (2021). Multifunctional gold nanoparticles for improved diagnostic and therapeutic applications: a review. *Nanoscale Research Letters*, 16, 1-27.

59. Reshma, V. G., and Mohanan, P. V. (2019). Quantum dots: Applications and safety consequences. *Journal of Luminescence*, 205, 287-298.

60. Ahmed, S.A., Nayak, A.K., Ansari, M.T., Sherikar, A., Siddique, M.U.M., Alkahtani, S., Ali, S., Tabish, M., Khatoon, S., Darraj, A.Q. and Hasnain, M.S. (2023). Quantum Dots in Biomedical Applications: Recent Advancements and Future Prospects. In *Carbon Nanostructures in Biomedical Applications* (pp. 169-196). Cham: Springer International Publishing.

61. Oh, E., Liu, R., Nel, A., Gemill, K. B., Bilal, M., Cohen, Y., and Medintz, I. L. (2016). Meta-analysis of cellular toxicity for cadmium-containing quantum dots. *Nature Nanotechnology*, 11(5), 479-486.

62. Wagner, A. M., Knipe, J. M., Orive, G., and Peppas, N. A. (2019). Quantum dots in biomedical applications. *Acta Biomaterialia*, 94, 44-63.

63. García de Arquer, F. P., Talapin, D. V., Klimov, V. I., Arakawa, Y., Bayer, M., and Sargent, E. H. (2021). Semiconductor quantum dots: Technological progress and future challenges. *Science*, 373(6555), eaaz8541.

64. Abdellatif, A. A., Younis, M. A., Alsharidah, M., Al Rugaie, O., and Tawfeek, H. M. (2022). Biomedical applications of quantum dots: overview, challenges, and clinical potential. *International Journal of Nanomedicine*, 17 1951-1970.

65. Sangtani, A., Petryayeva, E., Susumu, K., Oh, E., Huston, A.L., Lasarte-Aragones, G., Medintz, I.L., Algar, W.R. and Delehanty, J.B. (2019). Nanoparticle–Peptide–Drug Bioconjugates for Unassisted Defeat of Multidrug Resistance in a Model Cancer Cell Line. *Bioconjugate Chemistry*, 30(3), 525-530.

66. Uğurlu, Ö., Barlas, F. B., Evran, S., and Timur, S. (2020). The cell-penetrating YopM protein-functionalized quantum dot-plasmid DNA conjugate as a novel gene delivery vector. *Plasmid*, *110*, 102513.
67. Vu, T. Q., Maddipati, R., Blute, T. A., Nehilla, B. J., Nusblat, L., and Desai, T. A. (2005). Peptide-conjugated quantum dots activate neuronal receptors and initiate downstream signaling of neurite growth. *Nano Letters*, *5*(4), 603-607.
68. Rogers, K. E., Nag, O. K., Susumu, K., Oh, E., and Delehanty, J. B. (2023). Photothermal-Enhanced Modulation of Cellular Membrane Potential Using Long-Wavelength-Activated Gold Nanoflowers. *Bioconjugate Chemistry*, *34*(2), 405-413.
69. McCormick, D. A. (2014). Membrane potential and action potential. In *From Molecules to Networks* (pp. 351-376). Academic Press.
70. Sundelacruz, S., Levin, M., and Kaplan, D. L. (2009). Role of membrane potential in the regulation of cell proliferation and differentiation. *Stem Cell Reviews and Reports*, *5*(3), 231-246.
71. Nag, O. K., Muroski, M. E., Hastman, D. A., Almeida, B., Medintz, I. L., Huston, A. L., and Delehanty, J. B. (2020). Nanoparticle-mediated visualization and control of cellular membrane potential: strategies, progress, and remaining issues. *ACS Nano*, *14*(3), 2659-2677.
72. Sakmann, B., and Neher, E. (1984). Patch clamp techniques for studying ionic channels in excitable membranes. *Annual Review of Physiology*, *46*(1), 455-472.
73. Rios, G., Lubenov, E. V., Chi, D., Roukes, M. L., and Siapas, A. G. (2016). Nanofabricated neural probes for dense 3-D recordings of brain activity. *Nano letters*, *16*(11), 6857-6862.
74. Foroozandeh, P., and Aziz, A. A. (2018). Insight into cellular uptake and intracellular trafficking of nanoparticles. *Nanoscale Research Letters*, *13*(1), 1-12.
75. Chang, C. C., Chen, C. P., Wu, T. H., Yang, C. H., Lin, C. W., and Chen, C. Y. (2019). Gold nanoparticle-based colorimetric strategies for chemical and biological sensing applications. *Nanomaterials*, *9*(6), 861.
76. Xiong, R., Raemdonck, K., Peynshaert, K., Lentacker, I., De Cock, I., Demeester, J., De Smedt, S.C., Skirtach, A.G., and Braeckmans, K. (2014). Comparison of gold nanoparticle mediated photoporation: vapor nanobubbles outperform direct heating for delivering macromolecules in live cells. *ACS Nano*, *8*(6), 6288-6296.
77. Carvalho-de-Souza, J.L., Nag, O.K., Oh, E., Huston, A.L., Vurgaftman, I., Pepperberg, D.R., Bezanilla, F. and Delehanty, J.B. (2018). Cholesterol functionalization of gold nanoparticles enhances photoactivation of neural activity. *ACS Chemical Neuroscience*, *10*(3), 1478-1487.
78. Oh, E., Susumu, K., Goswami, R., and Mattoussi, H. (2010). One-phase synthesis of water-soluble gold nanoparticles with control over size and surface functionalities. *Langmuir*, *26*(10), 7604-7613.

79. McIsaac, R.S., Engqvist, M.K., Wannier, T., Rosenthal, A.Z., Herwig, L., Flytzanis, N.C., Imasheva, E.S., Lanyi, J.K., Balashov, S.P., Gradinaru, V. and Arnold, F.H. (2014). Directed evolution of a far-red fluorescent rhodopsin. *Proceedings of the National Academy of Sciences*, *111*(36), 13034-13039.
80. Hochbaum, D.R., Zhao, Y., Farhi, S.L., Klapoetke, N., Werley, C.A., Kapoor, V., Zou, P., Kralj, J.M., Maclaurin, D., Smedemark-Margulies, N. and Saulnier, J.L. (2014). All-optical electrophysiology in mammalian neurons using engineered microbial rhodopsins. *Nature Methods*, *11*(8), 825-833.
81. Smith, A. M., Mancini, M. C., and Nie, S. (2009). Second window for in vivo imaging. *Nature Nanotechnology*, *4*(11), 710-711.
82. de Puig, H., Tam, J. O., Yen, C. W., Gehrke, L., and Hamad-Schifferli, K. (2015). Extinction coefficient of gold nanostars. *The Journal of Physical Chemistry C*, *119*(30), 17408-17415.
83. Oh, E., Susumu, K., Jain, V., Kim, M., and Huston, A. (2012). One-pot aqueous phase growth of biocompatible 15–130 nm gold nanoparticles stabilized with bidentate PEG. *Journal of Colloid and Interface Science*, *376*(1), 107-111.
84. Loew, L. M. (1993). Confocal microscopy of potentiometric fluorescent dyes. *Methods in Cell Biology*, *38*, 195-209.
85. Tree-Udom, T., Seemork, J., Shigyong, K., Hamada, T., Sangphech, N., Palaga, T., Insin, N., Pan-In, P., and Wanichwecharungruang, S. (2015). Shape effect on particle-lipid bilayer membrane association, cellular uptake, and cytotoxicity. *ACS Applied Materials and Interfaces*, *7*(43), 23993-24000.
86. Choo, P., Liu, T., and Odom, T. W. (2021). Nanoparticle shape determines dynamics of targeting nanoconstructs on cell membranes. *Journal of the American Chemical Society*, *143*(12), 4550-4555.
87. Nethi, S. K., Mukherjee, S., Veeriah, V., Barui, A. K., Chatterjee, S., and Patra, C. R. (2014). Bioconjugated gold nanoparticles accelerate the growth of new blood vessels through redox signaling. *Chemical Communications*, *50*(92), 14367-14370.
88. Conde, J., Ambrosone, A., Sanz, V., Hernandez, Y., Marchesano, V., Tian, F., Child, H., Berry, C.C., Ibarra, M.R., Baptista, P.V. and Tortiglione, C. (2012). Design of multifunctional gold nanoparticles for in vitro and in vivo gene silencing. *ACS Nano*, *6*(9), 8316-8324.
89. Daraee, H., Eatemadi, A., Abbasi, E., Fekri Aval, S., Kouhi, M., and Akbarzadeh, A. (2016). Application of gold nanoparticles in biomedical and drug delivery. *Artificial cells, Nanomedicine, and Biotechnology*, *44*(1), 410-422.

90. Kim, D., Jeong, Y. Y., and Jon, S. (2010). A drug-loaded aptamer– gold nanoparticle bioconjugate for combined CT imaging and therapy of prostate cancer. *ACS Nano*, 4(7), 3689-3696.
91. Han, H. S., and Choi, K. Y. (2021). Advances in nanomaterial-mediated photothermal cancer therapies: toward clinical applications. *Biomedicines*, 9(3), 305.
92. Andrásfalvy, B.K., Galiñanes, G.L., Huber, D., Barbic, M., Macklin, J.J., Susumu, K., Delehanty, J.B., Huston, A.L., Makara, J.K. and Medintz, I.L. (2014). Quantum dot–based multiphoton fluorescent pipettes for targeted neuronal electrophysiology. *Nature methods*, 11(12), 1237-1241.
93. Chen, G., Cao, Y., Tang, Y., Yang, X., Liu, Y., Huang, D., Zhang, Y., Li, C. and Wang, Q. (2020). Advanced Near-Infrared Light for Monitoring and Modulating the Spatiotemporal Dynamics of Cell Functions in Living Systems. *Advanced Science*, 7(8), 1903783.
94. Paviolo, C. and Stoddart, P.R. (2017). Gold nanoparticles for modulating neuronal behavior. *Nanomaterials*, 7(4), 92.
95. Link, S., Burda, C., Nikoobakht, B. and El-Sayed, M.A. (2000). Laser-induced shape changes of colloidal gold nanorods using femtosecond and nanosecond laser pulses. *The Journal of Physical Chemistry B*, 104(26), 6152-6163.
96. Jia, Y.P., Ma, B.Y., Wei, X.W. and Qian, Z.Y. (2017). The in vitro and in vivo toxicity of gold nanoparticles. *Chinese Chemical Letters*, 28(4), 691-702.
97. Eom, K., Kim, J., Choi, J.M., Kang, T., Chang, J.W., Byun, K.M., Jun, S.B. and Kim, S.J. (2014). Enhanced infrared neural stimulation using localized surface plasmon resonance of gold nanorods. *Small*, 10(19), 3853-3857.
98. Monzel, C., Vicario, C., Piehler, J., Coppey, M., and Dahan, M. (2017). Magnetic control of cellular processes using biofunctional nanoparticles. *Chemical Science*, 8(11), 7330-7338.
99. Lee, D., and Hong, J. H. (2020). Nanoparticle-mediated therapeutic application for modulation of lysosomal ion channels and functions. *Pharmaceutics*, 12(3), 217.
100. Maysinger, D., Ji, J., Hutter, E., and Cooper, E. (2015). Nanoparticle-based and bioengineered probes and sensors to detect physiological and pathological biomarkers in neural cells. *Frontiers in Neuroscience*, 9, 480.
101. Hou, X., Zaks, T., Langer, R., and Dong, Y. (2021). Lipid nanoparticles for mRNA delivery. *Nature Reviews Materials*, 6(12), 1078-1094.
102. Guevara, M. L., Persano, F., and Persano, S. (2020). Advances in lipid nanoparticles for mRNA-based cancer immunotherapy. *Frontiers in Chemistry*, 8, 589959.

103. Yamamoto, S., Iwamaru, Y., Shimizu, Y., Ueda, Y., Sato, M., Yamaguchi, K., and Nakanishi, J. (2019). Epidermal growth factor-nanoparticle conjugates change the activity from anti-apoptotic to pro-apoptotic at membrane rafts. *Acta Biomaterialia*, 88, 383-391.
104. Iliff, J.J., Wang, M., Liao, Y., Plogg, B.A., Peng, W., Gundersen, G.A., Benveniste, H., Vates, G.E., Deane, R., Goldman, S.A. and Nagelhus, E.A. (2012). A paravascular pathway facilitates CSF flow through the brain parenchyma and the clearance of interstitial solutes, including amyloid β . *Science Translational Medicine*, 4(147), 147ra111-147ra111.
105. Lv, T., Zhao, B., Hu, Q., and Zhang, X. (2021). The glymphatic system: a novel therapeutic target for stroke treatment. *Frontiers in Aging Neuroscience*, 13, 689098.
106. Jessen, N. A., Munk, A. S. F., Lundgaard, I., and Nedergaard, M. (2015). The glymphatic system: a beginner's guide. *Neurochemical research*, 40, 2583-2599.
107. Fultz, N. E., Bonmassar, G., Setsompop, K., Stickgold, R. A., Rosen, B. R., Polimeni, J. R., and Lewis, L. D. (2019). Coupled electrophysiological, hemodynamic, and cerebrospinal fluid oscillations in human sleep. *Science*, 366(6465), 628-631.
108. Levendowski, D.J., Gamaldo, C., St Louis, E.K., Ferini-Strambi, L., Hamilton, J.M., Salat, D., Westbrook, P.R. and Berka, C. (2019). Head position during sleep: potential implications for patients with neurodegenerative disease. *Journal of Alzheimer's Disease*, 67(2), 631-638.
109. Brissaud, O., Villega, F., Pieter Konsman, J., Sanchez, S., Raffard, G., Franconi, J.M., Chateil, J.F. and Bouzier-Sore, A.K. (2010). Short-term effect of erythropoietin on brain lesions and aquaporin-4 expression in a hypoxic-ischemic neonatal rat model assessed by magnetic resonance diffusion weighted imaging and immunohistochemistry. *Pediatric Research*, 68(2),123-127.
110. Rizwan Siddiqui, M., Attar, F., Mohanty, V., Kim, K. S., Shekhar Mayanil, C., and Tomita, T. (2018). Erythropoietin-mediated activation of aquaporin-4 channel for the treatment of experimental hydrocephalus. *Child's Nervous System*, 34, 2195-2202.
111. Livnah, O., Stura, E. A., Middleton, S. A., Johnson, D. L., Jolliffe, L. K., and Wilson, I. A. (1999). Crystallographic evidence for preformed dimers of erythropoietin receptor before ligand activation. *Science*, 283(5404), 987-990.
112. Watowich, S. S., Hilton, D. J., and Lodish, H. F. (1994). Activation and inhibition of erythropoietin receptor function: role of receptor dimerization. *Molecular and Cellular Biology*. 14(6), 3535-3549.
113. McGraw, K. L., Fuhler, G. M., Johnson, J. O., Clark, J. A., Caceres, G. C., Sokol, L., and List, A. F. (2012). Erythropoietin receptor signaling is membrane raft dependent. *PloS One*, 7(4), e34477.

114. Bradburne, C.E., Delehanty, J.B., Boeneman Gemmill, K., Mei, B.C., Mattoussi, H., Susumu, K., Blanco-Canosa, J.B., Dawson, P.E. and Medintz, I.L. (2013). Cytotoxicity of quantum dots used for in vitro cellular labeling: role of QD surface ligand, delivery modality, cell type, and direct comparison to organic fluorophores. *Bioconjugate Chemistry*, 24(9), 1570-1583.
115. Susumu, K., Oh, E., Delehanty, J.B., Blanco-Canosa, J.B., Johnson, B.J., Jain, V., Hervey IV, W.J., Algar, W.R., Boeneman, K., Dawson, P.E. and Medintz, I.L. (2011). Multifunctional compact zwitterionic ligands for preparing robust biocompatible semiconductor quantum dots and gold nanoparticles. *Journal of the American Chemical Society*, 133(24), 9480-9496.
116. Field, L. D., Walper, S. A., Susumu, K., Lasarte-Aragones, G., Oh, E., Medintz, I. L., and Delehanty, J. B. (2018). A quantum dot-protein bioconjugate that provides for extracellular control of intracellular drug release. *Bioconjugate Chemistry*, 29(7), 2455-2467.
117. Delehanty, J. B., Medintz, I. L., Pons, T., Brunel, F. M., Dawson, P. E., and Mattoussi, H. (2006). Self-assembled quantum dot-peptide bioconjugates for selective intracellular delivery. *Bioconjugate Chemistry*, 17(4), 920-927.
118. Nag, O. K., Jeong, J. E., Le, V. S., Oh, E., Woo, H. Y., and Delehanty, J. B. (2020). Anionic Conjugated Polyelectrolytes for FRET-based Imaging of Cellular Membrane Potential. *Photochemistry and Photobiology*, 96(4), 834-844.
119. Nag, O.K., Stewart, M.H., Deschamps, J.R., Susumu, K., Oh, E., Tsytsarev, V., Tang, Q., Efros, A.L., Vaxenburg, R., Black, B.J. and Chen, Y. (2017). Quantum dot-peptide-fullerene bioconjugates for visualization of in vitro and in vivo cellular membrane potential. *ACS Nano*, 11(6), 5598-5613.
120. Delehanty, J.B., Bradburne, C.E., Susumu, K., Boeneman, K., Mei, B.C., Farrell, D., Blanco-Canosa, J.B., Dawson, P.E., Mattoussi, H. and Medintz, I.L. (2011). Spatiotemporal multicolor labeling of individual cells using peptide-functionalized quantum dots and mixed delivery techniques. *Journal of the American Chemical Society*, 133(27), 10482-10489.
121. Hibi, M., and Hirano, T. (1998). Signal Transduction Through Cytokine Receptors. *International Reviews of Immunology*, 17(1-4), 75-102.
122. Jasieniak, J., Smith, L., Van Embden, J., Mulvaney, P., and Califano, M. (2009). Re-examination of the size-dependent absorption properties of CdSe quantum dots. *The Journal of Physical Chemistry C*, 113(45), 19468-19474.
123. Chen, D., Zhao, F., Qi, H., Rutherford, M., and Peng, X. (2010). Bright and stable purple/blue emitting CdS/ZnS core/shell nanocrystals grown by thermal cycling using a single-source precursor. *Chemistry of Materials*, 22(4), 1437-1444.

124. Kitchen, P., Salman, M. M., Abir-Awan, M., Al-Jubair, T., Törnroth-Horsefield, S., Conner, A. C., and Bill, R. M. (2020). Calcein fluorescence quenching to measure plasma membrane water flux in live mammalian cells. *STAR protocols*, 1(3), 100157.
125. Algar, W. R., Prasuhn, D. E., Stewart, M. H., Jennings, T. L., Blanco-Canosa, J. B., Dawson, P. E., and Medintz, I. L. (2011). The controlled display of biomolecules on nanoparticles: a challenge suited to bioorthogonal chemistry. *Bioconjugate Chemistry*, 22(5), 825-858.
126. Delehanty, J.B., Bradburne, C.E., Boeneman, K., Susumu, K., Farrell, D., Mei, B.C., Blanco-Canosa, J.B., Dawson, G., Dawson, P.E., Mattoussi, H. and Medintz, I.L. (2010). Delivering quantum dot-peptide bioconjugates to the cellular cytosol: escaping from the endolysosomal system. *Integrative Biology*, 2(5-6), 265-277.
127. Prasuhn, D.E., Deschamps, J.R., Susumu, K., Stewart, M.H., Boeneman, K., Blanco-Canosa, J.B., Dawson, P.E. and Medintz, I.L. (2010). Polyvalent display and packing of peptides and proteins on semiconductor quantum dots: predicted versus experimental results. *Small*, 6(4), 555-564.
128. Hoshyar, N., Gray, S., Han, H., and Bao, G. (2016). The effect of nanoparticle size on in vivo pharmacokinetics and cellular interaction. *Nanomedicine*, 11(6), 673-692.
129. Sulahian, R., Cleaver, O., and Huang, L. J. S. (2009). Ligand-induced EpoR internalization is mediated by JAK2 and p85 and is impaired by mutations responsible for primary familial and congenital polycythemia. *Blood, The Journal of the American Society of Hematology*, 113(21), 5287-5297.
130. Al-Sarraf, H., Malatiali, S., Al-Awadi, M., and Redzic, Z. (2018). Effects of erythropoietin on astrocytes and brain endothelial cells in primary culture during anoxia depend on simultaneous signaling by other cytokines and on duration of anoxia. *Neurochemistry International*, 113, 34-45.
131. Liu, J., Narasimhan, P., Song, Y. S., Nishi, T., Yu, F., Lee, Y. S., and Chan, P. H. (2006). Epo protects SOD2-deficient mouse astrocytes from damage by oxidative stress. *Glia*, 53(4), 360-365.
132. Wang, C., Xu, Y., Huang, Y., and Huang, Y. (2017). Effects of erythropoietin and methylprednisolone on AQP4 expression in astrocytes. *Molecular Medicine Reports*, 16(5), 5924-5930.
133. Tenchov, R., Bird, R., Curtze, A. E., and Zhou, Q. (2021). Lipid nanoparticles— from liposomes to mRNA vaccine delivery, a landscape of research diversity and advancement. *ACS Nano*, 15(11), 16982-17015.
134. Gregoriadis, G. (2021). Liposomes and mRNA: Two technologies together create a COVID-19 vaccine. *Medicine in Drug Discovery*, 12, 100104.

135. Zhang, W., Jiang, Y., He, Y., Boucetta, H., Wu, J., Chen, Z., and He, W. (2022). Lipid carriers for mRNA delivery. *Acta Pharmaceutica Sinica B*.
136. Ma, X., Xiong, Y., and Lee, L. T. O. (2018). Application of nanoparticles for targeting G protein-coupled receptors. *International Journal of Molecular Sciences*, 19(7), 2006.
137. Yamamoto, S., Iwamaru, Y., Shimizu, Y., Ueda, Y., Sato, M., Yamaguchi, K., and Nakanishi, J. (2019). Epidermal growth factor-nanoparticle conjugates change the activity from anti-apoptotic to pro-apoptotic at membrane rafts. *Acta Biomaterialia*, 88, 383-391.
138. Zhang, S., Ouyang, T., and Reinhard, B. M. (2022). Multivalent Ligand-Nanoparticle Conjugates Amplify Reactive Oxygen Species Second Messenger Generation and Enhance Epidermal Growth Factor Receptor Phosphorylation. *Bioconjugate Chemistry*, 33(9), 1716-1728.
139. Elsabahy, M., Nazarali, A., and Foldvari, M. (2011). Non-viral nucleic acid delivery: key challenges and future directions. *Current Drug Delivery*, 8(3), 235-244.
140. Akhtar, S., and Benter, I. (2007). Toxicogenomics of non-viral drug delivery systems for RNAi: potential impact on siRNA-mediated gene silencing activity and specificity. *Advanced Drug Delivery Reviews*, 59(2-3), 164-182.
141. Wilbie, D., Walther, J., and Mastrobattista, E. (2019). Delivery aspects of CRISPR/Cas for in vivo genome editing. *Accounts of Chemical Research*, 52(6), 1555-1564.
142. Gkazi, S. A. (2019). Quantifying CRISPR off-target effects. *Emerging Topics in Life Sciences*, 3(3), 327-334.
143. Yang, M., and Brackenbury, W. J. (2013). Membrane potential and cancer progression. *Frontiers in Physiology*, 4, 185.
144. Yang, M., and Brackenbury, W. J. (2022). Harnessing the membrane potential to combat cancer progression. *Bioelectricity*, 4(2), 75-80.
145. Yu, H. (2022). Depolarization or hyperpolarization: Emerging role of altered bioelectricity in breast cancer metastasis. *EBioMedicine*, 76, 103853.
146. Staley, K. (2015). Molecular mechanisms of epilepsy. *Nature Neuroscience*, 18(3), 367-372.
147. Muroski, M. E., Nag, O., Oh, E., Huston, A. L., and Delehanty, J. B. (2019). Controlled membrane depolarization through photothermal effects of tethered gold nanoparticles. In *Colloidal Nanoparticles for Biomedical Applications XIV* 10892, 70-75. SPIE BiOS.

148. Sabourian, P., Yazdani, G., Ashraf, S. S., Frounchi, M., Mashayekhan, S., Kiani, S., and Kakkar, A. (2020). Effect of physico-chemical properties of nanoparticles on their intracellular uptake. *International Journal of Molecular Sciences*, 21(21), 8019.
149. Seegar, T. C., Eller, B., Tzvetkova-Robev, D., Kolev, M. V., Henderson, S. C., Nikolov, D. B., and Barton, W. A. (2010). Tie1-Tie2 interactions mediate functional differences between angiopoietin ligands. *Molecular Cell*, 37(5), 643-655.
150. Ma, Y., Pandzic, E., Nicovich, P. R., Yamamoto, Y., Kwiatek, J., Pagon, S. V., Benda, A., Rossy, J., and Gaus, K. (2017). An intermolecular FRET sensor detects the dynamics of T cell receptor clustering. *Nature communications*, 8(1), 15100.
151. Periasamy, A., Wallrabe, H., Chen, Y., and Barroso, M. (2008). Quantitation of protein-protein interactions: confocal FRET microscopy. *Methods in cell biology*, 89, 569-598.